Nondestructive Measurement and Quantitative Evaluation of Wall Thinning in a Long-distance Metal Pipe Using Microwaves

LIU Linsheng

Nagoya University

February, 2012

Nondestructive Measurement and Quantitative Evaluation of Wall Thinning in a Long-distance Metal Pipe Using Microwaves

(マイクロ波による長い金属配管内減肉の非破壊検査及び定量評価に関する研究)

PhD Dissertation

By

LIU Linsheng

Submitted to
Department of Mechanical Science and Engineering,
Graduate School of Engineering, Nagoya University, Japan

名古屋大学・工学研究科・機械理工学専攻
(材料強度・評価学研究グループ)

In partial fulfillment of the requirements for the degree of

Doctor of Engineering

NAGOYA UNIVERSITY

February, 2012

Abstract

Metal pipes are used widely in industry. During recent twenty years, accidents caused by pipe wall thinning (PWT) have been reported frequently all over the world. PWT is one of the most serious defects in the pipes used in industry. Efficiently detecting and quantitatively evaluating the PWT locations and degrees (lengths and depths) in these pipes, especially for long-distance pipes, are mandatory for effective maintenance and lifetime prediction of the pipelines in order to avoid severe economical and social damages.

This research aims to find an efficient, nondestructive and quantitative way of detecting the locations and degrees of PWT in a long-distance metal pipe. Since a conductive pipe (such as a metal pipe) can be taken as a circular waveguide of microwaves, microwave signals can propagate a long distance with low attenuation in the pipe. Meanwhile, a wavelength, group velocity, and wave impedance change will occur at the PWT section.

When building up a resonance structure concerning the wavelength changes at the PWT section in the pipe under test (PUT), frequency domain measurement (FDM) of microwave signals is adopted to evaluate the PWT degrees (depths). When considering the time of flight (TOF) of microwave signals propagating in the PUT and that reflected from the PWT section, time domain measurement (TDM) of signals is adopted to evaluate the PWT locations and lengths (a length is obtained from the difference of the evaluated locations of the start and end points of a PWT section).

To carry out the FDM and TDM, a microwave vector network analyzer (VNA) was employed and a pair of coaxial-line sensors was designed to generate microwave signals propagating in the pipe. The two coaxial-line sensors were utilized separately with the VNA working at S12 or S11 mode. A VNA can realize the FDM of microwave signals directly, and the TDM results are obtained from inverse fast Fourier transform (IFFT) of

FDM results. To approach a long-distance pipe with PWT defects, pipe specimens and PWT joints are used to combine many sets of PUTs with lengths longer than 2 m.

The evaluation of PWT depths is realized by firstly designing a two-port coaxial-line sensor and working the VNA at S12 (or S21) mode while building up a resonance condition in the PUT, and then tactfully solving the resonance equations. By comparing the evaluated PWT depths obtained using this method with the nominal PWT depths in the pipes, the maximum error of evaluation is found to be less than 0.05 mm, which is less than 0.294% of the inner diameter of the pipe. It indicates that a high precision evaluation method to evaluate the PWT depth in a long-distance pipe is established.

The evaluation of PWT locations is realized by designing a single port coaxial-line sensor and working the VNA at S11 mode while measuring microwaves signals propagating and reflecting in the PUT. By analyzing time domain response of signals and extracting the TOF corresponding to the PWT location, PWT locations are quantitatively evaluated after the group velocity of the signals in the pipe was calibrated. The arithmetical mean error of the evaluation for PWT locations is less than 1.7 mm, i.e. less than 0.068% of the length of the corresponding pipe. It indicates that an efficient and precise method to quantitatively evaluate PWT locations in a long-distance pipe has been established.

In addition, through optimizing the sweeping frequency range, an improved TDM method for PWT location evaluation with space resolution no longer than the value of the pipe's inner diameter has been realized.

Keywords:

Microwave, Nondestructive testing (NDT), Pipe wall thinning (PWT), Vector network analyzer (VNA), Frequency domain measurement (FDM), Inverse fast Fourier transform (IFFT), Time domain measurement (FDM), Time of flight (TOF), Pipe under test (PUT)

List of Symbols

f : working frequency of the microwave

$\omega = 2\pi f$: angular frequency

f_c : cutoff frequency of the waveguide

λ : wavelength of the plane waves propagating in the material/medium

λ_c : cutoff wavelength of the waveguide

$\mu = \mu_r \mu_0$: permeability of the medium, where μ_r is the relative permeability

μ_0 : permeability of free space with value of $\mu_0 = 4\pi \times 10^{-7}$ H/m

$\varepsilon = \varepsilon_r \varepsilon_0$: permittivity of the medium, where $\varepsilon_r = \varepsilon_r' - \mathrm{j}\varepsilon_r''$ is the relative permittivity

ε_0 : permittivity of free space with value of $\varepsilon_0 = 8.854 \times 10^{-12}$ F/m

$k = \omega\sqrt{\mu\varepsilon} = 2\pi / \lambda$: wavenumber of the material filling the waveguide/transmission line

k_c : cutoff wavenumber of the waveguide

$\gamma = \alpha + \mathrm{j}\beta$: complex propagation constant, where α is the attenuation constant

$\beta = \sqrt{k^2 - k_c^2}$: propagation constant

$\eta = \sqrt{\mu / \varepsilon}$: impedance of the medium

$\eta_0 = \sqrt{\mu_0 / \varepsilon_0}$: impedance of free space with value of $\eta_0 = 376.7\ \Omega$

$v = 1/\sqrt{\mu\varepsilon}$: velocity of plane wave in the material filling the waveguide/transmission line

$c = 1/\sqrt{\mu_0\varepsilon_0}$: velocity of light in free space with value of $c = 2.998 \times 10^8$ m/s

$v_g \le v$: group velocity in the waveguide or transmission line

$v_p = \omega / \beta = v^2 / v_g \ge v$: phase velocity in the waveguide or transmission line

σ : conductivity of the material

Z : wave impedance of the waveguide or transmission line

p_{nm} : mth zeros of the first kind of Bessel functions $J_n(x)=0$

p'_{nm} : mth extrema of the first kind of Bessel functions $J'_n(x)=0$

Contents

Contents

Chapter 1. General Introduction

1.1. Introduction

1.1.1. Research Background

After the end of World War II, metal pipes started to be widely used in industry, such as oil and gas transportation, chemical industry and various kinds of power plants. During the recent twenty years, pipe explosion accidents caused by pipe wall thinning (PWT) have been reported frequently all over the world after most of these pipes had been in service for more than twenty years.

Among these accidents, there are two typical ones took place at nuclear power plants. One is the feedwater pipe steam explosion in the Unit 2 pressurized water reactor (PWR) of Surry Nuclear Power Plant in US in 1986, during which 4 workers were killed and other 4 ones were scalded (this was the worst accident in terms of human cost of any in the US commercial nuclear industry) [1]. The other is the hot water and steam leaking from a broken pipe (caused by flow accelerated corrosion and/or cavitation-erosion) of No. 3 PWR at the Mihama Nuclear Power Plant in Japan in 2004, during which 4 workers were killed and 7 other ones were injured (the accident had been called Japan's worst nuclear power accident before the crisis at Fukushima I Nuclear Power Plant of 2011, which is a boiling water reactor (BWR)) [2]. These accidents seriously damaged public confidence in nuclear safety and the world's nuclear measures.

The schematic diagram of the piping system and power transfer in a nuclear BWR is shown in Fig. 1.1, and that in a nuclear PWR is shown in Fig. 1.2. It can be found that there are long distance metal pipes (generally carbon steel pipes) connected with the

reactor for both the BWR and PWR power plants.

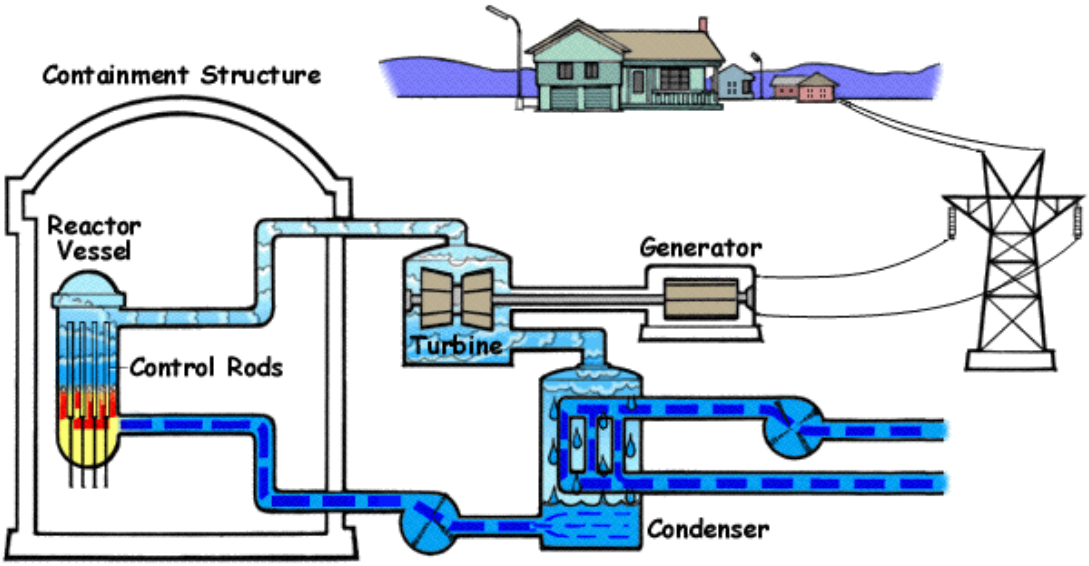

Fig. 1.1. Schematic diagram of piping system and power transfer in a BWR [3].

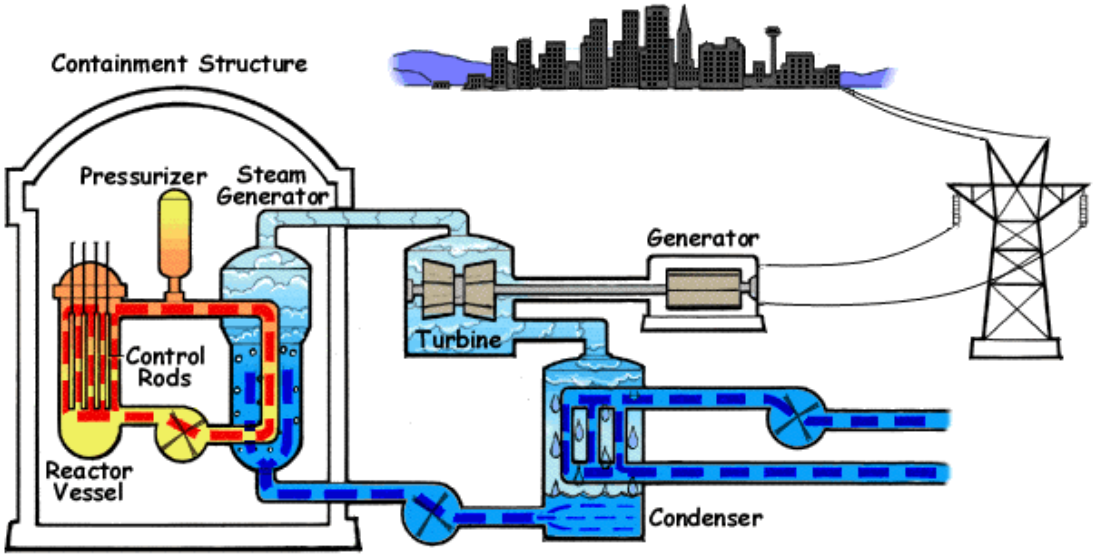

Fig. 1.2. Schematic diagram of power transfer in a PWR, where primary coolant is in orange and the secondary coolant (steam and later feedwater) is in blue [4].

In addition, the July 18, 2007 New York City steam pipe explosion (caused by the failure of a Consolidated Edison 24-inch underground steam pipe installed in 1924 near Grand Central Terminal) sent a geyser of hot steam up from beneath a busy intersection, with a 40-story-high shower of mud and flying debris raining down on the crowded streets of Midtown Manhattan in New York City, New York, United States. The escaping steam shook nearby office buildings, causing many occupants to immediately evacuate. A 51-year-old New Jersey woman (worked a block from the site) died of a heart attack suffered while fleeing the disaster area. 45 people were injured (two injured critically) [5].

In nowadays, nuclear power plants generate 1/3 of energy for the countrywide energy consumption in Japan. From the viewpoint of both environment and energy supply, the nuclear power plants are not only necessary but also very important. Other countries such as the Unite States, Russia, China, and India also are confronted with the similar conditions. As mentioned above, wall thinning is one of the most serious defects in industrial pipes, and, as a result, it is one of the prime criminals for these accidents. However, during the service of a pipe, the corrosion and/or erosion in the inner wall of the pipe are inevitable for pipes under any kind of usage and condition although the erosion speeds differ. The PWT condition is especially serious for the ageing piping system that served for over tens of years, in which the pipe wall of the PWT section is not thick enough to safely hold the inner pressure of the water or steam that flows through along the pipe. The PWT defects that putting the piping systems into the boundary over-pressurized condition become the direct villain of the piece of potential accidents.

In addition, the aforementioned accidents that took place at nuclear power plants not only killed human beings and brought tragedy to the society but also seriously damaged public confidence in nuclear safety. The reason of the accidents is due to the inevitable

ageing and PWT of the pipes, however, there is no standard measure and also theoretically impossible to establish a uniform scientific criterion to predict confirmedly where PWT defects will happen and when (through how many years and days) the wall thinning will be serious enough (at the boundary over-pressurized condition) and should be replaced immediately. Moreover, PWT is generally not well-proportioned for all parts of a pipe, but instead the local wall thinning defect in the pipe is the most general condition. As a result, it will be generally a big extravagant waste of time, manpower, and money to periodically replace all of the pipes in a piping system. Therefore it is quite important and emergent to find out a stable and scientific method to remotely detect and precisely evaluate the PWT locations and degrees accurately and efficiently.

Moreover, with the development of the oil and gas industry in China and some other countries, the piping systems for transportation also develop very fast. As a result, the safety of operation for such transportation piping systems gets more and more attention. For an example, the piping systems for this purpose are more than 3×10^6 km at present in China, and are continually developed by 1,000 to 2,000 km per year. However, most of the present underground piping systems have already been in service for more than 20 years, and the leakage accidents caused by PWT happened frequently in recent years [6,7]. In the United States, the annual cost associated with corrosion damage of structural components is greater than the combined annual cost of natural disasters, including hurricanes, storms, floods, fires and earthquakes [8]. Similar findings have been made by studies conducted in the United Kingdom, Germany, and Japan. According to the U.S. Department of Transportation Office of Pipeline Safety, internal corrosion caused approximately 15% of all reportable incidents affecting gas transmission pipelines over the past several years, leading to an average cost of $3 million annually in property

damage, as well as several fatalities [8]. The need to manage and mitigate corrosion damage has rapidly increased as materials are placed in more extreme environments and pushed beyond their original design life. Therefore, how often to inspect the in-service piping systems and how to find out PWT problems and repair them efficiently have also become an important problem to reduce the cost and price of oil and gas. Considering all of the mentioned problems and the potential hazards caused by PWT, timely remote detection and accurate evaluation of PWT conditions in the long distance pipes have become quite important and emergent.

This research aims to find an efficient, nondestructive and quantitative way of detecting the locations and degrees of PWT in a long-distance metal pipe, which can ensure that the workers work under a safe condition and help the urban and rural residences live in a safe and harmonious environment where they don't need to worry about the breaking out of pipe or steam explosion disasters.

1.1.2. Two Important Aspects of PWT Problems

To solve the aforementioned PWT problems, a stable, credible, and nondestructive method for effective maintenance and accurate lifetime prediction of a long-distance pipe are most needed. The effective maintenance means that the inspector can detect the PWT locations, i.e. where the PWT happens, effectively during the inspection, which makes it possible to repair or replace the PWT parts timely if necessary; while the accurate and trustful lifetime prediction means that the inspector can accurately evaluate the PWT degrees, i.e., PWT lengths and depths, of a PWT defect, which makes it possible to predict whether or not the PWT part can still be in service safely and when it will be out of use and should be replaced. In other words, the two most important aspects of a PWT problem are the PWT locations (for effective and efficient maintenance) and degrees

(for accurate and credible lifetime prediction).

The schematic diagram for a pipe having different PWT locations and degrees is shown in Fig. 1.3. In this figure, l_0 is the total length of the pipe that having a wall thickness of t, l_{11} is the start point of the first PWT defect that having PWT length of l_{21} and PWT depth of t_1, and $(l_{11}+l_{21}+l_{12})$ is the start point of the second PWT defect that having PWT length of l_{22} and PWT depth of t_2.

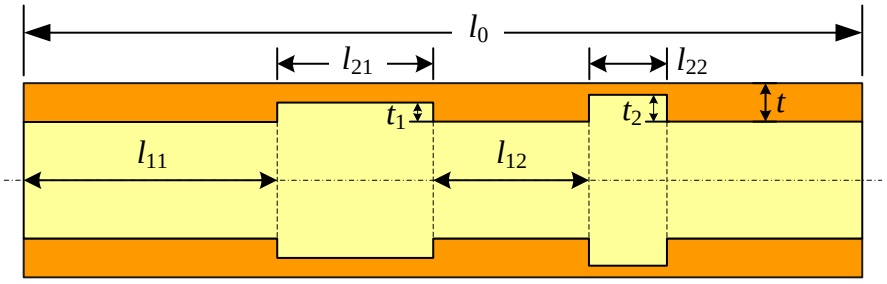

Fig. 1.3. Schematic diagram of a pipe having two PWT locations and degrees.

As a result, efficient detection and high-precision evaluation of the PWT locations and degrees in a pipe are the two most important works for solving the PWT problems, especially for a long-distance pipe. They are mandatory for effective maintenance and accurate and credible lifetime prediction of the pipelines so as to avoid severe potential economical and social damages.

For the first aspect, i.e. PWT locations, there are three kinds of typical potential PWT locations. The first one is the place behind an orifice inserted in the pipe, where water or other liquid flows through. This is because a strong bifurcation of the liquid that flowing in the pipe will generally take place behind the orifice and it will generate serious wall thinning on the inner side of the pipe. The second one is the place behind an elbow of the piping system. This is because the liquid that flowing through along the pipe will generally wash out much more of the inner wall than other places of the pipe. The third

kind of typical potential PWT locates around a welding part of the inner wall of a pipe. This is also because the liquid that flowing through along the pipe will generally wash out more of the inner wall than the other comparatively smooth parts of a pipe. However, it should be noted out that wall thinning of other places inside the pipe are also possible, and the start of PWT inside the ordinary pipe wall can be caused by lots of complicated reasons. Moreover, after a small PWT occurs at some part of a pipe, this part will become more easily to be eroded than the other parts inside the pipe. As a result, a throughout inspection should be carried out along the full pipe to confirm all the PWT locations where a PWT happens. This is general a boring and time and manpower costing process before the establishment of our method, especially for a long-distance buried pipe.

As mentioned above, the PWT degree means the length and depth of a PWT defect. It can be seen clearly from the schematic diagram shown in Fig. 1.3 where two different PWT defects having both different PWT lengths and depths.

It can be summarized as that the two most important aspects of a PWT problem needed for detection and evaluation are the PWT locations and degrees. This dissertation will focus on nondestructive and high-efficiency detection and high-precision evaluation of them in a long-distance pipe so as to solve the PWT problems comprehensively.

1.1.3. Review of NDT Methods and Applications

Definition of Nondestructive Testing (NDT)

Nondestructive (or written as *Non-destructive*) testing and evaluation (NDT&E) is the science and practice of evaluating various properties of a material without compromising its utility and usefulness [9]. Those material properties might be physical, chemical, mechanical, or geometrical. The interrogating signal must be suitable for use in a laboratory or test situation and be able to interact with the material under test. The existing standard

techniques for NDT&E methods may not always be capable of inspecting the new composites that are replacing metals in some applications. Microwave and millimeter wave NDT&E techniques are recognized as tools that render a more comprehensive picture of an inspection problem. Electromagnetic signals at microwave and millimeter wave frequencies are well suited for inspecting dielectric materials and composite structures in many critical applications [10].

NDT has also been defined (by Canadian Institute for NDE [11]) as to examine structures, materials or components without damaging or destroying the object being tested and provide a means to ensure product reliability and quality. There is an assortment of NDT techniques used throughout a broad cross-section of industries. The five most widely used techniques being radiography, ultrasonics, eddy current, liquid penetrant, and magnetic particle. Moreover, NDT is used in all sectors of industry including aerospace, nuclear, automotive, oil and petro-chemical, welding and steel production [11].

In addition, NDT is defined by the American Society for Nondestructive Testing as comprising those test methods used to examine an object, material or system without impairing its future usefulness, and it is generally applied to nonmedical investigations of material integrity [12]. Ultrasonic, X-rays and endoscopes are used for both medical testing and industrial testing. In the 1940s, many members of the American Society for Nondestructive Testing (then the Society for Industrial Radiography) were medical X-ray professionals. Medical NDT, however, has come to be treated by a body of learning so separate from industrial NDT that today most physicians never use the word nondestructive [12]. NDT is used to investigate the material integrity of the test object. A number of other technologies such as radio astronomy, voltage and amperage measurement and rheometry (flow measurement) are nondestructive but are not used to evaluate material properties

specifically. NDT is concerned in a practical way with the performance of the test piece such as how long may the piece be used and when does it need to be checked again. Radar and sonar are classified as NDT when used to inspect dams, for instance, but not when they are used to chart a river bottom.

Discontinuity Detection

NDT is not confined to crack detection. Other discontinuities include porosity, wall thinning from corrosion and many sorts of disbonds [12]. Nondestructive material characterization is a growing field concerned with material properties including material identification and microstructural characteristics (such as resin curing, case hardening and stress) that have a direct influence on the service life of the test object. NDT has also been defined by listing or classifying the various methods. This approach is practical in that it typically highlights methods in use by industry.

Purposes of NDT

Since the 1920s, NDT has developed from a laboratory curiosity to an indispensable tool of production [12]. No longer is visual examination the principal means of determining quality. NDTs in great variety are in worldwide use to detect variations in structure, minute changes in surface finish, the presence of cracks or other physical discontinuities, to measure the thickness of materials and coatings and to determine other characteristics of industrial products [12]. The categories of NDT methods are shown in TABLE 1.1.

Modern NDTs are used by manufacturers (1) to ensure product integrity and reliability; (2) to avoid failures, prevent accidents and save human life; (3) to make a profit for users; (4) to ensure customer satisfaction and maintain the manufacturer’s reputation; (5) to aid in better product design; (6) to control manufacturing processes; (7) to lower manufacturing costs; (8) to maintain uniform quality level; and (9) to ensure operational readiness [12].

TABLE 1.1. Nondestructive testing (NDT) method categories [12].

Basic Categories	**Objectives**
Mechanical and optical	color, cracks, dimensions, film thickness, gaging, reflectivity, strain distribution and magnitude, surface finish, surface flaws, through cracks
Penetrating radiation	cracks, density and chemistry variations, elemental distribution, foreign objects, inclusions, microporosity, misalignment, missing parts, segregation, service degradation, shrinkage, thickness, voids
Electromagnetic and electronic	alloy content, anisotropy, cavities, cold work, local strain, hardness, composition, contamination, corrosion, cracks, crack depth, crystal structure, electrical and thermal conductivities, flakes, heat treatment, hot tears, inclusions, ion concentrations, laps, lattice strain, layer thickness, moisture content, polarization, seams, segregation, shrinkage, state of cure, tensile strength, thickness, disbonds
Sonic and ultrasonic	crack initiation and propagation, cracks, voids, damping factor, degree of cure, degree of impregnation, degree of sintering, delaminations, density, dimensions, elastic moduli, grain size, inclusions, mechanical degradation, misalignment, porosity, radiation degradation, structure of composites, surface stress, tensile, shear and compressive strength, disbonds, wear
Thermal and infrared	bonding, composition, emissivity, heat contours, plating thickness, porosity, reflectivity, stress, thermal conductivity, thickness, voids
Chemical and analytical	alloy identification, composition, cracks, elemental analysis and distribution, grain size, inclusions, macrostructure, porosity, segregation, surface anomalies
Auxiliary Categories	**Objectives**
Image generation	dimensional variations, dynamic performance, anomaly characterization and definition, anomaly distribution, anomaly propagation, magnetic field configurations
Signal image analysis	data selection, processing and display, anomaly mapping, correlation and identification, image enhancement, separation of multiple variables

Each method can be completely characterized in terms of five principal factors [12]: (1) energy source or medium used to probe the test objects such as X-rays, ultrasonic waves or thermal radiation; (2) nature of the signals, image or signature resulting from interaction with the test objects such as attenuation of X-rays or reflection of ultrasound; (3) means of detecting/sensing resulting signals such as photo emulsion, piezoelectric crystal or inductance coil; (4) method of indicating/recording signals such as meter deflection, oscilloscope trace or radiograph; and (5) basis for interpreting the results such as direct/indirect indication, qualitative/quantitative, and pertinent dependencies.

The objective of each test method is to provide information about the following material parameters [12]: (1) discontinuities such as cracks, voids, inclusions, PWT, and delaminations; (2) structure or malstructure including crystalline structure, grain size, segregation, and misalignment; (3) dimensions and metrology such as thickness, diameter, gap size, discontinuity size); (4) physical and mechanical properties such as reflectivity, conductivity, elastic modulus, and sonic velocity; (5) composition and chemical analysis such as alloy identification, impurities, and elemental distributions; (6) stress and dynamic responses such as residual stress, crack growth, wear, and vibration; (7) signature analysis such as image content, frequency spectrum, and field configuration.

1.1.4. Related NDT Methods for PWT Testing

As mentioned above, PWT is one of the most serious ones among the defects in the metal pipes used in industry [13,14]. Efficiently detecting and quantitatively evaluating the PWT locations and degrees (lengths and depths) in these pipes, especially for long-distance pipes, are mandatory for effective maintenance and lifetime prediction of the pipelines in order to avoid severe economical and social damages. An efficient, accurate, credible, and nondestructive method is urgently needed for solving the PWT problem.

During recent years, many NDT techniques, such as x-ray [15], electrical potential drop [16], ultrasonic [17,18], magnetic flux leakage [19], eddy current testing [20] and so on, have been used for the measurement of PWT. However, except for the hollow cylindrical guided wave (HCGW) of ultrasonic method [18], all of them can only inspect a pipe locally. Even though HCGW can propagate a long distance along an isolated pipe, the ultrasonic energy will attenuate much faster when there are many girth welds on the surface of the pipe [21]. Besides, all of the aforementioned methods are difficult to measure pipes buried under ground, in walls of some structures, or under other buried conditions. This is the main shortage for the HCGW method, because the ultrasonic energy will attenuate much faster in the pipe surrounded by different kinds of media such as earth, concrete, etc. [22]. In reality, all those methods generally take lots of time and labor to inspect a long-distance pipe, and most of them can only measure the PWT degrees locally, i.e., they can only solve part of the first aspect of the PWT problem.

1.1.5. Microwave NDT of PWT

Application of Microwave NDT

The term *microwaves* refers to alternating current signals with frequencies between 0.3 and 300 GHz, with a corresponding electrical wavelength between $\lambda = c / f = 1$ m and 1 mm, respectively [23]. Signals with wavelengths on the order of millimeters are also called *millimeter waves*. Fig. 1.4 shows a diagram of the electromagnetic spectrum that showing various properties across the range of frequencies and wavelengths, and Fig. 1.5 shows the location of the microwave frequency band in the electromagnetic spectrum [24]. The electromagnetic spectrum is the range of all possible frequencies of electromagnetic radiation. The *electromagnetic spectrum* of an object is the characteristic distribution of electromagnetic radiation emitted or absorbed by that particular object [24].

Because of the high frequencies (and short wavelengths), standard circuit theory (SCT) generally cannot be used to directly to solve microwave network problems [23]. In a sense, SCT is an approximations or special use of the broader theory of electromagnetics as described by Maxwell's equations. Therefore, in microwave engineering, Maxwell's equations and their solutions are used in the nature of these equations that mathematical complexity arises, since the equations involve vector differential or integral operations on vector field quantities and these fields are functions of spatial coordinates. A field theory solution generally provides a complete description of the electromagnetic filed at every point in space, which is usually much more information than we really need for most practical purposes. The high frequencies and short wavelengths of microwave energy provide unique opportunities of the application of microwave systems although they make for difficulties in analysis and design of microwave components and systems.

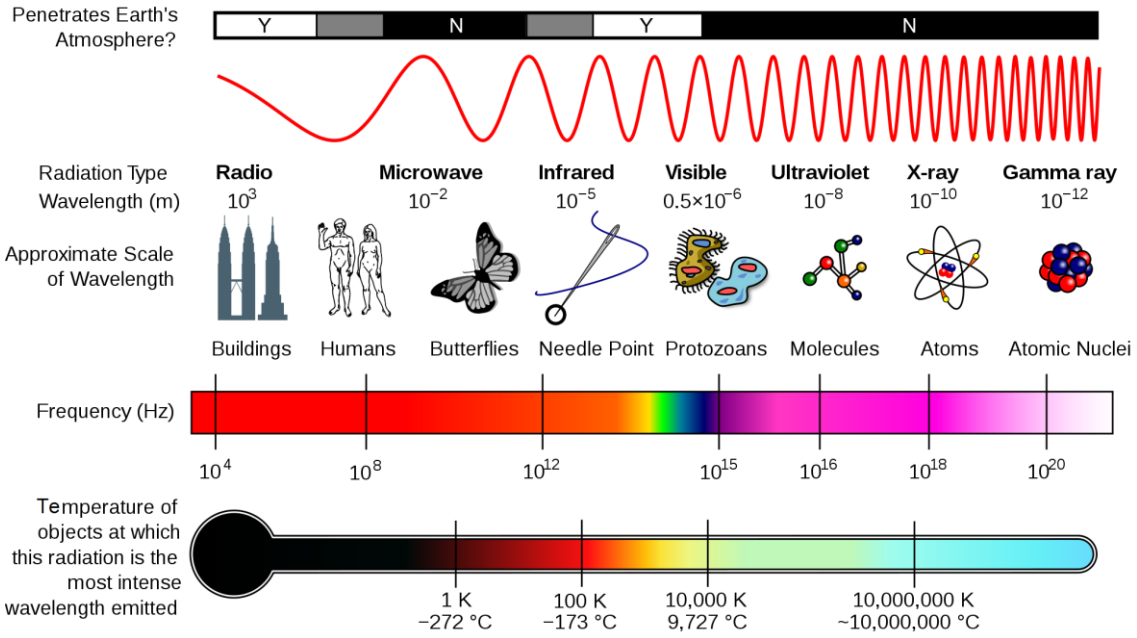

Fig. 1.4. A diagram of the electromagnetic spectrum, showing various properties across the range of frequencies and wavelengths [24].

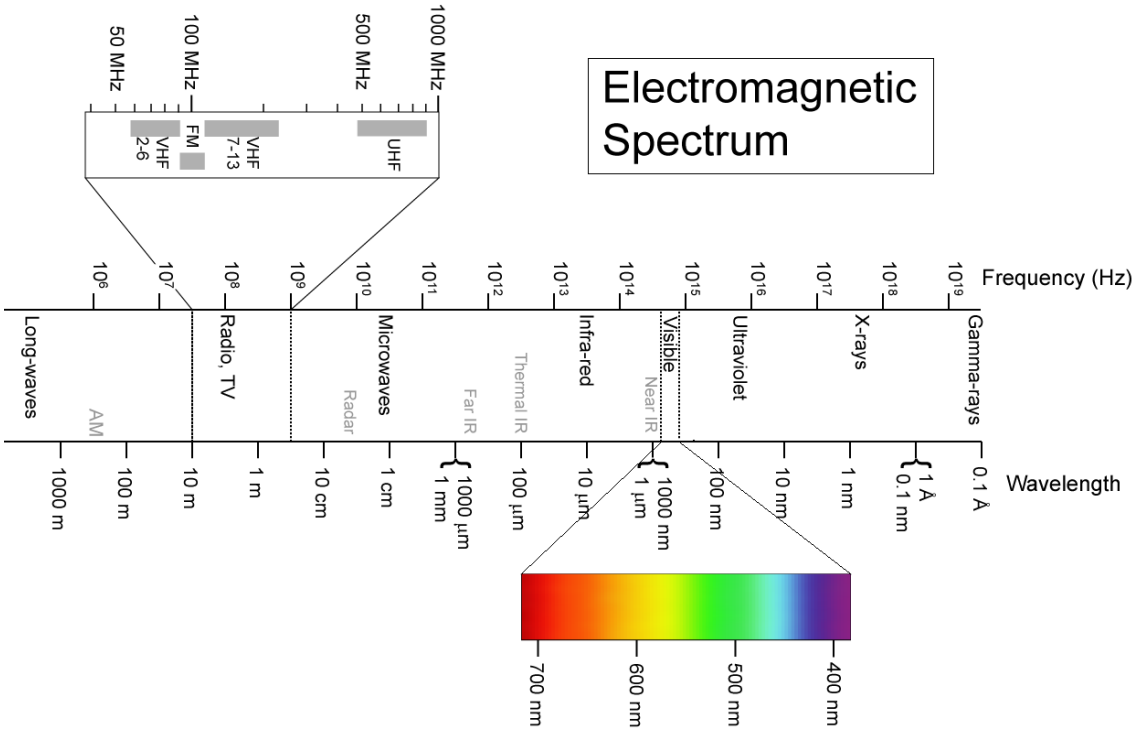

Fig. 1.5. Location of microwave frequency band in the electromagnetic spectrum [24].

Testing with microwaves is dominated by the basic properties of microwaves. Since their penetration in good conducting materials is minimal, they are mainly used to test non-conducting materials. This includes dielectric and lossy dielectric materials. Testing and measurements on conducting materials are limited to dimensional testing such as thickness gauging and surface measurements such as testing for surface breaking flaws [25]. Microwave nondestructive techniques have a long history dating from the early 1950s, with a strong flurry of activities in the 1960s and 1990s. However, these techniques still are not widely known in the nondestructive testing (NDT) community and often are referred to as *emerging techniques* or *others* [10,26,27]. It is only during the last two or three years that some NDT conferences have allocated a whole session or two solely to the topic of microwave NDT. For those involved in the research and development of microwave NDT techniques who have long appreciated the advantages of such techniques, this

increased visibility is a welcome and encouraging change.

Microwave NDT has many advantageous features [28,29], such as coherence properties (magnitude & phase), large available bandwidth, life-cycle inspection possibilities, on-line and real-time inspection, operation in industrial environments, little to no need for operator expertise, relatively inexpensive, applications to where other NDT techniques have limited applicability. Moreover, the measurement systems are possible to be non-contact, one-sided, mono-static, compact and small, low power, in-field and operator friendly, adaptable to existing scanning platforms, robust and repeatable [28]. The Zoughi laboratory (amntl) does the basic R&D and applied research in the field of microwave NDT&E, covering frequency range of 1 GHz – 150 GHz. Examples of their recent investigations and developments are [28]: (1) detection and sizing of small changes (in the few micrometer range) in dielectric sheet materials, such as polymers, coatings, ceramics and thermal barrier coatings; (2) porosity estimation in composites and ceramics such as thermal barrier coatings and composite skin subjected to loading (i.e., aircraft radome skin); (3) detection and estimation of void and delamination within sandwich composites such as aircraft radomes, thermal insulation materials such as spray on foam insulation (SOFI) and acreage heat tiles; (4) detection of internal flaws, defects and moisture permeation in thick composites including honeycomb structures used in aircraft radomes and SOFI; (5) fatigue crack detection and sizing on metal surfaces, using three distinct approaches; (6) detection of surface anomalies in metals (i.e., rolled); (7) cure state monitoring of various chemically produced materials (i.e., resin binder, rubber, etc.); (8) detection and evaluation of corrosion (including corrosion precursor pitting) under paint and composite laminates; (9) cure-state monitoring in resins, rubber products and cement-based materials (i.e., cement paste, mortar and concrete); (10) determination of water-to-cement ratio

(w/c) in fresh cement paste, mortar and concrete; (11) determination of water-to-cement ratio (w/c) in hardened (cured) cement paste, mortar and concrete; (12) determination of sand-to-cement ratio (s/c) in mortar; (13) determination of coarse aggregate-to-cement ratio (ca/c) in concrete; (14) evaluation of aggregate segregation in concrete; (15) detection of grout-filled cells in masonry blocks; (16) evaluation of concrete compressive strength; (17) evaluation of porosity in mortar; (18) detection and evaluation of chloride added to the mixing water of cement-based materials; (19) detection of cyclical chloride ingress in mortar; (20) detection and sizing of delamination between FRP composites and cement-based materials such as CFRP-strengthened bridge concrete bridge members; (21) development of hybrid measurement technique using embedded modulated scattering PIN diode-loaded dipole antenna for material characterization and microwave imaging; (22) near-field high-resolution imaging; (23) development of synthetic aperture-focused (SAF) and holographical or 3-D imaging of interior of composites and objects; (24) development of rapid imaging systems using coherent transceivers and rotary scanning platforms; (25) development of real-time, portable, battery-operated and high-resolution imaging techniques/systems using modulated scatterer technique (MST); (26) development of frequency-modulated continuous-wave (FM-CW) radar for short-range applications such as detection and evaluation of flaws in composite structures (e.g., walls); (27) development of robust microwave and millimeter wave testing and imaging systems for specific applications; (28) microwave and millimeter wave noninvasive diagnosis of human skin, and (29) new application being discovered continuously.

Moreover, Y. Ju, *et al* in 1999 derived a new method of microwave NDT that using a developed open-ended coaxial-line sensor to increase the spatial resolution and inspect the delamination in IC packages [30]. During their research, an open-ended coaxial line

sensor (with inner and outer conductors in smaller dimension than the wavelength) was used to incident and receive signals that interacting with the tested objects, and the magnitude of the reflection coefficient (proportional to the total reflection from different interfaces) was measured as a characteristic signal to distinguish the delamination. Thereafter, improved research of Ju research group developed a new microwave imaging technique to detect the delamination in IC packages [31-34], in which the image was created by measuring the phase of the effective reflection coefficient at the aperture of the coaxial line sensor. These improved studies developed a method for further increase the spatial resolution of microwave imaging and better evaluation of the shape and size of the delamination. The resolution affected by the dimensions of the sensor, the frequency of operation, and the standoff distance was investigated in their research. The experimental results indicate that microwave imaging is a promising technique for integrity assessment of IC packages [31].

In addition, Y. Ju *et al* in 2002 developed a significant NDT method for quantitative measurement of electrical conductivity of semiconductor (Si) wafers in a contactless fashion using reflection of microwaves using curve fitting [35], during which a focusing sensor was developed to focus a 110 GHz millimeter wave beam on the surface of a Si wafer. Thereafter, an improved theory of carrying out the contactless measurement of electrical conductivity independent of wafer thickness was developed in 2005 [36]. Further research of L. Liu and Y. Ju in 2010 improved the measurement and evaluation method utilized to evaluate the electrical conductivity of doped GaAs wafers by using two analytical and explicit expressions that having only two undetermined coefficients (instead of the previous curve fitting method that needing at least three specimens whose conductivities are known for calibration [35,36]), which was derived based on the

characteristics of the microwave detector and the fact that the microwave measurement is independent of the thickness of the wafer [37].

In the year 2005, Y. Ju *et al* demonstrated a microwave NDT method to evaluate the shape and size of a small 3D crack [38]. By considering the interference phenomenon occurring in the case of 3D cracks, a parameter reflecting microwave interference effect, which was a function of the position of the sensor in the direction of the crack length, was introduced into the usual dual frequency evaluation-equation. From the modified dual frequency equation, a new component named interference waveform was obtained based on the amplitude of reflection coefficient measured at two different frequencies. On the other hand, a corresponding interference waveform based on the interference model, which can be calculated from the assumed shape and size of a 3D crack, was also introduced. By comparing these two interference waveforms, the evaluation of the shape and size of the 3D crack were carried out.

It should be noted out that a significant microwave AFM system has been developed by Y. Ju research group from the year 2007 [39], and this AFM measurement system is a combination of the principles of scanning probe microscope and microwave-measurement technique and recent improvement makes it be capable of investigating surface topography and electrical property of conductive and dielectric materials simultaneously on a nanometer scale [40-41].

Microwave NDT Utilized for Solving PWT Problems

Since microwave can propagate a long distance with quite little attenuation in a low-loss dielectric medium such as air, gas, and gasoline, it can be used to overcome shortcomings of the aforementioned methods. To microwave NDT, a metal pipe under test (PUT) can be promisingly taken as a circular waveguide, and all the energy of microwave signals

is confined inside the pipe [23,42-44]. Therefore the propagation and attenuation of microwave in the pipe are independent of the surrounding conditions of the pipe [43,44]. Some studies had been done by utilizing time of flight (TOF) of microwave signals to detect locations of deep inner cracks that having depth no less than 2 mm inside a metal pipe [45,46], however, the evaluation of PWT, i.e. a shallow defect with small changes of the inner diameter of a pipe, is still not carried out. Moreover, there is no literature before our research reporting the inspection of metal pipes using microwaves at the open-end condition, which is the most common case in the practice [43,44]. In addition, the microwave NDT of PWT depth, which is generally more important than its location for predicting the life time of the pipe, is a brand new method for remote detection and precise evaluation. This thesis reports and demonstrates our comprehensive research on the evaluation method of microwave NDT&E for both PWT degrees and locations measured under open-end conditions.

The schematic diagram of circular waveguide theory for microwave NDT of PWT is shown in Fig. 1.6, where the "Microwave Instrument" means the microwave VNA, and "T" and "R" mean the transmitting and receiving ports of the instrument, respectively. d_0 is the distance between T&R ports and $d_0 = 0$ is measurement under S11 mode.

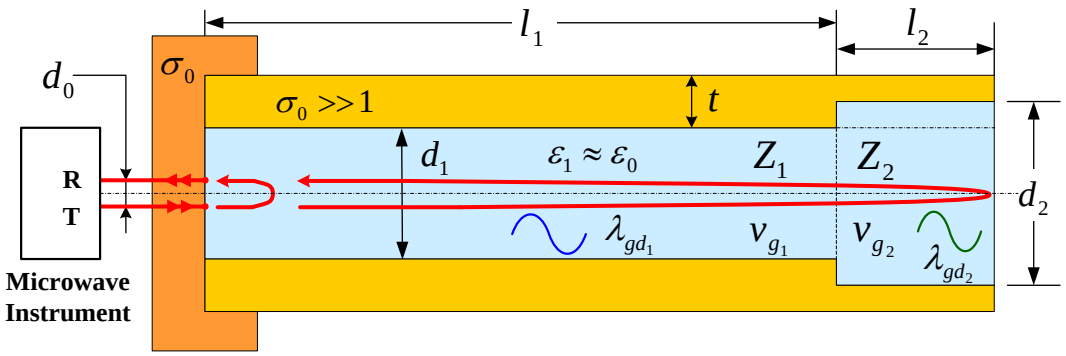

Fig. 1.6. Theoretical schematic diagram for microwave NDT of PWT.

In Fig. 1.6, σ_0 is the conductivity of the wall of the metal pipe that having a value of $\sigma_0 >> 1$; l_1 and l_2 are lengths of pipe at the defect-free part that having a inner diameter of d_1 and at the PWT part that having a inner diameter of d_2, respectively. t is the wall thickness of the defect-free part of the pipe. Since air is the inner medium inside the pipe, the permittivity ε_1 approximately equals to ε_0, which is the permittivity of free space. λ_{gd_1}, Z_1, and v_{g_1} are the wavelength, wave impedance, and group velocity in the defect-free part of the pipe, and they are all functions of the inner diameter of the pipe. As shown in Fig. 1.6, PWT causes increase in the inner diameter, as a result, the wavelength, wave impedance, and group velocity in the PWT part change to λ_{gd_2}, Z_2, and v_{g_2}. The detailed relations are shown as follows [23],

$$\lambda_{gd} = 2\pi/\beta = 2\pi/\sqrt{k^2 - k_c^2} = 1\Big/\sqrt{\mu\varepsilon f^2 - [\chi_{nm}/(\pi d)]^2} \tag{1.1}$$

$$Z_{\mathrm{TE}} = \eta k/\beta = \eta/\sqrt{1-(k_c/k)^2} \quad \text{and} \quad Z_{\mathrm{TM}} = \eta\beta/k = \eta\cdot\sqrt{1-(k_c/k)^2} \tag{1.2}$$

$$v_g = v^2(\beta/\omega) = v\cdot\sqrt{1-(k_c/k)^2} = v\cdot\sqrt{1-(f_c/f)^2} \tag{1.3}$$

where μ and ε are the permeability and permittivity of the medium inside the pipe, and f is the working frequency of microwaves. In addition, $\chi_{nm} = p_{nm}$, which is the *m*th zeros of the first kind of Bessel functions $J_n(x)$=0, for microwaves of TM_{nm} modes, or $\chi_{nm} = p'_{nm}$, which is the *m*th extrema of the first Bessel functions $J'_n(x)$=0, for TE_{nm} modes. $\eta = \sqrt{\mu/\varepsilon}$ is the wave impedance for the plane wave, $v = 1/\sqrt{\mu\varepsilon}$ is the velocity of plane wave, and $k = \omega\sqrt{\mu\varepsilon} = 2\pi/\lambda$ is the wavenumber of the material filling the waveguide. $\beta = \sqrt{k^2 - k_c^2}$ is the propagation constant, $k_c = 2\chi_{nm}/d$ is the cutoff wavenumber, and $f_c = k_c/(2\pi\sqrt{\mu\varepsilon}) = v\chi_{nm}/(\pi d)$ is the cutoff frequency. As the medium inside the pipe is air, these parameters are approximately $\mu = \mu_0$, $\varepsilon = \varepsilon_0$, $\eta = \eta_0$, $k = 2\pi f/c$, and $f_c = c\chi_{nm}/(\pi d)$, which are parameters of free space.

It can be found from Eqs. (1.1) to (1.3) that, for a given working frequency, the

wavelength and Z_{TE} will decrease, and the group velocity and Z_{TM} will increase when the inner diameter of the pipe increases due to a PWT.

It is theoretically possible to establish a group of resonance equations from which λ_{gd_2} can be solved, and then d_2 that having information of PWT depth can be obtained from Eq. (1.1) and expressed in Eq. (1.4), and, as a result, the PWT depth D_{PWT} that equals to $(d_2 - d_1)/2$ is quantitatively evaluated.

$$d_2 = \chi_{nm} \Big/ \left[\pi \sqrt{\mu\varepsilon f^2 - \left(1/\lambda_{gd_2}\right)^2} \right] \tag{1.4}$$

This will be demonstrated, analyzed and discussed in detail in the following Chapter 3 of this thesis.

In addition, as a PWT defect causes a wave impedance change in the circular waveguide, a reflection of the microwaves will happen at the interface of start and end points of the PWT section. The schematic diagrams are shown in Fig. 1.7.

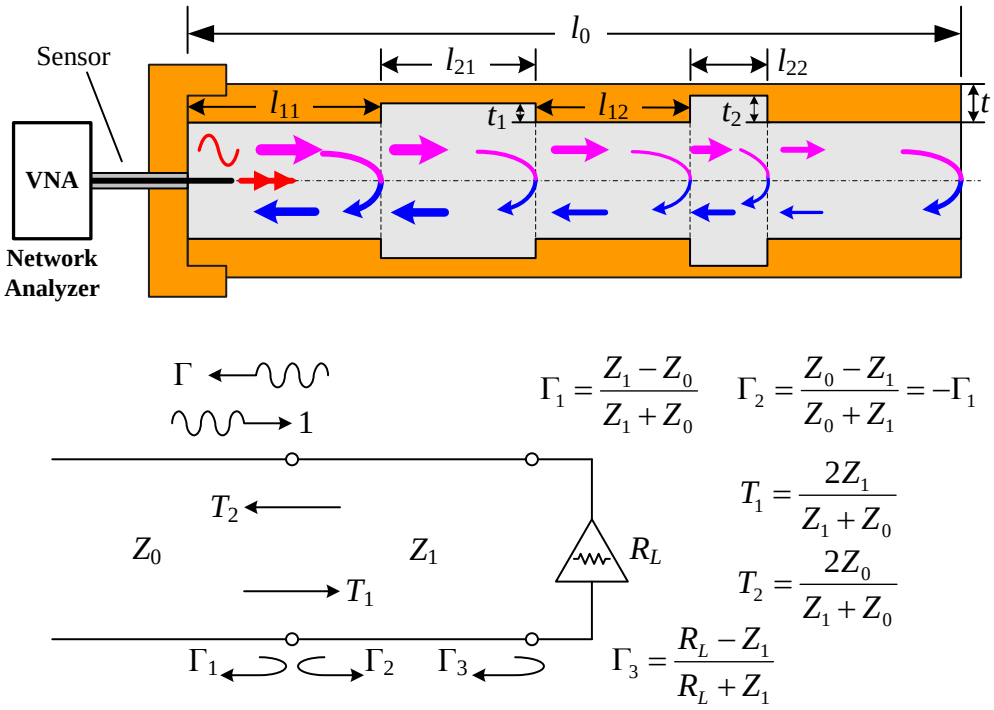

Fig. 1.7. Reflection and transmission at the junctions of discontinuities in a waveguide.

In Fig. 1.7, the parameters shown in the upper figure have the same meaning as shown in Fig. 1.3. Z_0 and Z_1 are the different wave impedances in the transmission line, and R_L is the terminated load resistance. Γ_1, Γ_2 and Γ_3 are partial reflection coefficients, and Γ is the overall reflection coefficient. T_1 and T_2 are partial transmission coefficients.

Fortunately, the time domain measurement (TDM) results of a VNA that are obtained from the inverse Fourier transform of the frequency domain measurement (FDM) results can be utilized as an effective tool for locating fault, identifying impedance variations in connectors, etc. It is also described in the application note of Agilent Technology [47] that fault location is a powerful example of the bandpass mode of a VNA. In the TDM, not only are the large connector responses obvious, but also any discontinuities due to the bends or mismatches within the cable, transmission line, or waveguide are seen as discrete inductive or capacitive impedance discontinuities. Any positive or negative reflection that deviates from the characteristic impedance is clearly apparent. The locations and magnitudes of these discontinuities are easily determined. To show this usage clear, a significant schematic diagram that shows the TDM responses in comparison with the FDM responses is shown in Fig. 1.8. It can be found that the discontinuities are clearly observed in the TDM responses that shown in Fig. 1.8(b).

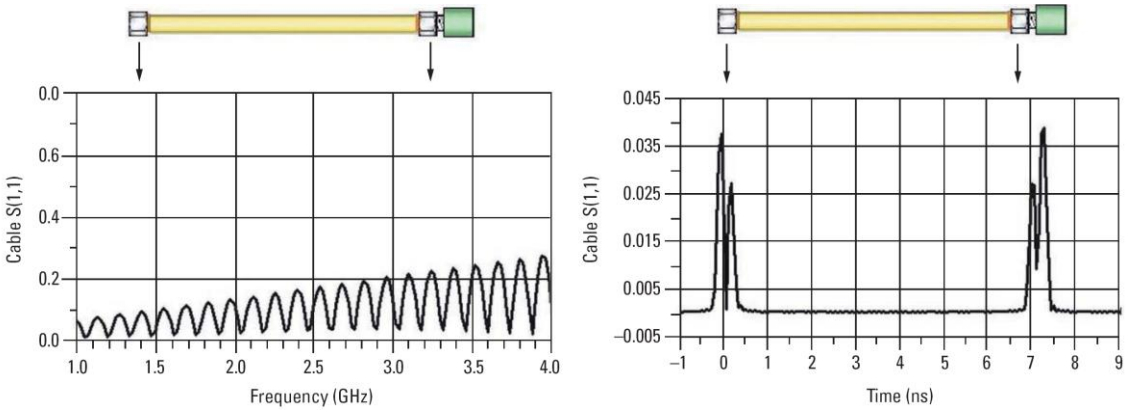

(a) FDM responses (b) TDM responses

Fig. 1.8. Schematic diagram of reflection responses shown in (a) FDM and (b) TDM [47].

In this research, the TDM results are utilized to evaluate the PWT locations, and the detailed methods are shown in the following Chapter 4 of the thesis.

At the end of this part, it should be noted that two different kinds of coaxial-line sensors are designed in this research. One is composed of two coaxial-line cables at the same side working separately as T (transmitting) and R (receiving) ports when the VNA working at S12 (or S21) mode, and the other is composed of a single coaxial-line cable working as both the T and R ports when the VNA working at S11 mode. The detailed structures of the two sensors are shown in Figs. 1.9(a) and 1.9(b), respectively.

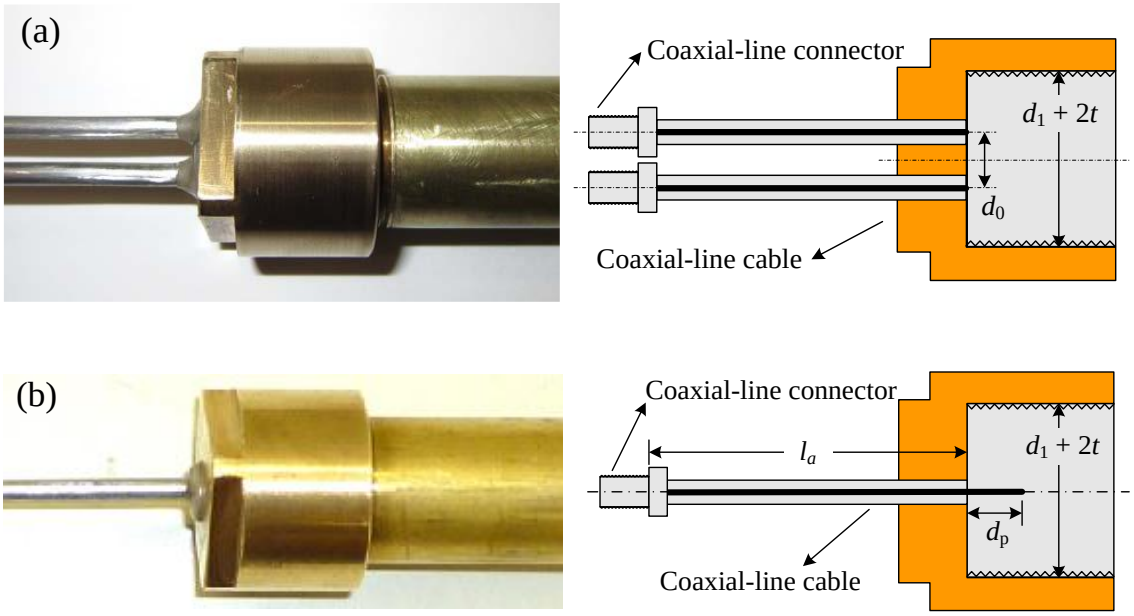

Fig. 1.9. The two kinds of self-designed coaxial-line sensors used in this research.

1.2. Objectives of this Research

As it is mentioned above, the two most important aspects of a PWT problem are the PWT locations (for effective and efficient maintenance) and degrees (for accurate and credible lifetime prediction). The research demonstrated in this thesis reports the

efficient, effective and quantitative microwave NDT&E method for remote testing of both the PWT degrees and PWT locations in a long-distance metal pipe measured under open-end condition.

Since a conductive pipe (such as a metal pipe) can be taken as a circular waveguide of microwaves, microwave signals can propagate a long distance with low attenuation in the pipe. Meanwhile, a wavelength, group velocity, and wave impedance change will occur at the PWT section.

Because the degree of PWT is generally more important than its location for predicting the life time of the pipe, the research firstly aims to solve the problem through remote NDT and quantitative evaluation of the PWT depth utilizing the FDM results recorded of the microwave VNA. Moreover, as the PWT locations are also very important for effective and efficient maintenance of the pipeline systems, the research also developed a remote NDT&E method for PWT locations utilizing the TDM results that obtained from IFFT of the FDM results. Finally, since the PWT lengths are also an important character for PWT defects, the research further developed a high-resolution TDM method that can not only be used for NDT of the PWT locations but also of the PWT lengths (no less than the inner diameter of the PUT) through optimizing the working frequency range of microwaves.

1.2.1. Frequency Domain Measurement (FDM) for PWT Depth Evaluation

The PWT depth in a metal pipe was firstly detected utilizing the resonance phenomenon of microwave at a short-end condition with high microwave frequencies (microwaves working at high order modes), and the possibility to quantitatively evaluate the PWT using microwaves was proved by comparing the experimental and theoretical analysis results [42].

In this study, we focus on establishing a more systematic nondestructive evaluation method using microwaves to inspect a pipe in a large scale at an open-end condition and to measure the PWT remotely with using the dominant mode frequencies [43]. After confirming the working mode of microwaves for certain frequencies, the wavelength of microwave in a waveguide is a function of the frequency and the inner diameter of the pipe [23]. By tracing the route of microwave propagating in the pipe, the resonance condition of the microwaves propagating in the pipe is established, and then, by solving the resonance equations, the wavelength of microwave at the PWT part and then the inner diameter of the PWT part including the direct information of the PWT depth can be quantitatively evaluated, from which the PWT depths are quantitatively evaluated.

1.2.2. Time Domain Measurement (TDM) for PWT Location Evaluation

After having established the FDM method for remote NDT&E of PWT depths [43], we further demonstrates the PWT location evaluation method in open-end pipes utilizing time domain measurement (TDM) results of microwave signals.

Because a PWT defect in the pipe acts as discontinuity of the wave impedance of the waveguide and causes reflection peaks at both the start and the end of the PWT section in time domain signals, the TDM of microwave signals is adopted in this research and the time of flight (TOF) extracted from the TDM results of the microwave signals is utilized to detect the locations of PWT defects in a metal pipe [44].

In this research, we design a rotationally symmetric coaxial line sensor, and utilized the TOF of microwaves to detect the location of PWT defect. The sensor is designed based on the studies of Gimenno and Guglielmi [48], Piotrowski [49], and Adous *et al* [50], which have shown that when a coaxial line is connected directly to a circular waveguide under the rotational symmetry condition, only TM_{0m} modes are excited in the circular

waveguide.

It should be noted that the research in this part mainly aims to establish an efficient and stable method to determine the PWT location in a long-distance pipe regardless of the start point and end point of a PWT defect since lengths of PWT defects are normally no longer than the inner diameter of the pipe. After the location is determined, more detailed information such as the start and end points, as well as the shape of a PWT defect can be evaluated by a further development of the proposed method or by other local detection methods with further advance in accuracy.

1.2.3. Improved TDM for Evaluation of PWT Locations and Lengths

In our previous studies [43], the PWT degrees of a 2 m long pipe were remotely examined and quantitatively evaluated with a high precision using microwave signals at frequency domain. Meanwhile, TDM results of microwave signals, which is derived from inverse fast Fourier Transform (IFFT) of the frequency domain signals has been used as an effectively tool to detect fault locations in a metal pipe in our previous studies [44]. However, our previous study mainly aimed to establish an efficient and stable method to determine the PWT location in a long-distance pipe regardless of the start and end points of a PWT defect. Thus, only the dominant TM_{01} mode was generated in the pipe by a self-designed rotationally symmetric coaxial-line sensor to act as the working mode. It is found that the response resolution for the time of flight (TOF) of the TM_{01} mode signals at time domain was not high enough and the reflection signals from the start and end points of the PWT section were overlapped and difficult to separate [44]. In this part, we aim to improve the response resolution of the time domain signals, i.e. the ability to resolve two closely-spaced responses, or a measure of how close two responses can be to each other and still be distinguished from each other [47], by optimizing the sweeping

frequency range, and thereby find out a method to detect the PWT locations with higher resolution, which can successfully evaluate the start and end points of a PWT defect with length no less than the inner diameter of the pipe. Moreover, a reference pipe under the open condition is utilized to calibrating the group velocity at the optimum frequency range in this work to make the calibration easier to carry out than the previous TDM method that calibrated at the short circuit condition [44,51].

It should be noted that the response resolution of PWT length testing and evaluation depends upon the microwave mode, the frequency range and the relative propagation velocity of the signal path.

1.3. Organization of the Chapters

This dissertation aims to solve the two most important problems, i.e., the PWT locations (for effective and efficient maintenance) and degrees (for accurate and credible lifetime prediction), of a PWT defect in a long distance metal pipe. It reports the microwave NDT&E method for remote, efficient, effective, and quantitative testing and evaluation of both the PWT degrees and PWT locations in a long-distance metal pipe measured under the open-end condition.

Chapter 1 is a general introduction of the background of this research, such as the accidents caused by PWT problems, the two most important aspects of the problem, the related methods derived for solving this problem and their shortcomings, advantages of microwave NDT methods, and method of microwave NDT utilized for solving PWT problems. The signification of this research is presented step by step.

Chapter 2 introduces the microwave theory for solving the PWT problem. As we solve the PWT problem by firstly taking the PUT as a circular waveguide and designing

two kinds of different coaxial-line sensors to generate microwave signals into the PUT, and secondly utilizing mode analysis and transmission line theory in modeling and equation solving, basic microwave theories of transmission line, circular waveguide, and coaxial line are introduced and discussed in this chapter.

Chapter 3 focuses on establishing a NDT&E method using microwaves working at the dominant mode frequencies to inspect a pipe in a large scale at the open-end condition and to measure the PWT depths remotely. By designing a T&R coaxial-line sensor to generate and receive microwaves into and from the PUT, and tracing the microwaves propagating in the pipe, the resonance condition of the microwaves propagating in the pipe is established, and then, by solving the resonance equations, the wavelength of microwave at the PWT part and then the inner diameter of the PWT part including the direct information of the PWT depth are quantitatively evaluated.

Chapter 4 represents a rotationally symmetric coaxial-line sensor designed by ourselves and the PWT location evaluation method in open-end pipes utilizing time domain measurement (TDM) results of microwave signals. Because a PWT defect in the pipe acts as discontinuity of the wave impedance of the waveguide and causes reflection peaks at both the start and end points of the PWT section in TDM results, the TDM of microwave signals is adopted in this research and the time of flight (TOF) extracted from the TDM results of the microwave signals is utilized to detect the locations of PWT defects in a metal pipe.

Chapter 5 shows an improved TDM method for high-resolution evaluation of the PWT locations and lengths. Because the response resolution, i.e. the ability to resolve two closely-spaced responses or a measure of how close two responses can be to each other and still be distinguished from each other, for the TOF of the TM_{01} mode signals

in the TDM method shown in the previous chapter is not high enough and the reflection signals from the start and end points of the PWT section are overlapped and difficult to separate, in this chapter, we improve the response resolution of the TDM results by optimizing the sweeping frequency range and thereby find out a method to detect the PWT locations with higher resolution, which can successfully evaluate the start and end points of a PWT defect with length no less than the inner diameter of the pipe.

Chapter 6 is the conclusion and prospect of the microwave NDT&E methods derived and shown in detail in this dissertation.

References

[1] See: http://en.wikipedia.org/wiki/Surry_Nuclear_Power_Plant

[2] See: http://en.wikipedia.org/wiki/Mihama_Nuclear_Power_Plant

[3] See: http://www.nrc.gov/reading-rm/basic-ref/students/animated-bwr.html (United States Nuclear Regulatory Commission)

[4] See: http://en.wikipedia.org/wiki/Pressurized_water_reactor

[5] See: http://en.wikipedia.org/wiki/2007_New_York_City_steam_explosion

[6] H. He, L. Li, and X. Jiang, J. Xi'an Petrol. Ins., **16**, 43 (in Chinese), (2001).

[7] Y. Shi, J. Liu, and W. Wang, Industri. Saf. Environ. Prot., **32**, 46 (in Chinese), (2006).

[8] B. H. Thacker, G. M. Light, J. F. Dante, E. Trillo, F. Song, C. F. Popelar, K. E. Coulter, and R. A. Page, Pipeline Gas. J., **237**(3), (2010).

[9] P. J. Shull, Nondestructive Evaluation: Theory, Techniques, and Applications, New York: Marcel Dekker, (2002).

[10] R. Zoughi, Microwave Non-Destructive Testing and Evaluation (Principles) (Non-Destructive Evaluation Series **4**), The Netherlands: Kluwer Academic Publishers, (2000).

[11] Canadian Institute for NDE (See: http://www.cinde.ca)

[12] American Society for Nondestructive Testing (See: http://www.asnt.org)

[13] R. B. Dooley and V. K. Chexal, Int. J. Pres. Ves. Pip., **77**, 85 (2000).

[14] A. Vageswar, K. Balasubramaniam, C. V. Krishnamurthy, T. Jayakumar, and B. Raj, NDT & E Int., **42**, 275 (2009).

[15] G. Kajiwara, J. Test. Eval., **33**, 295 (2005).

[16] T. Shimakawa, H. Takahashi, H. Doi, K. Watashi, and Y. Asada, Nuclear Eng. Des., **139**, 283 (1993).

[17] K. R. Leonard and M. K. Hinders, Ultrasonics, **43**, 574 (2005).

[18] H. Nishino, M. Takemoto, and N. Chubachi, Appl. Phys. Lett., **85**, 1077 (2004).

[19] J. Ding, Y. Kang, and X. Wu, NDT & E Int., **39**, 53 (2006).

[20] J. B. Nestleroth and R. J. Davis, NDT & E Int., **40**, 77 (2007).

[21] Y. Li, L. Sun, Z. Song, and Y. Zhang, Ultrasonics, **44**(S1), e1111 (2006).

[22] C. Aristégui, M. J. S. Lowe, and P. Cawley, Ultrasonics, **39**, 367 (2001).

[23] D. M. Pozar, Microwave Engineering (2nd Ed), New York: John Wiley & Sons, (1998).

[24] See: http://en.wikipedia.org/wiki/Electromagnetic_spectrum

[25] N. Ida, Microwave NDT, The Netherlands: Kluwer Academic Publishers, (2000).

[26] R. Zoughi, Int. Adv. Nondestr. Test., **15**, 255 (1990).

[27] R. Zoughi, Res. Nondestr. Eval. **7**, 71 (1995).

[28] Appl. Microw. Nondestr. Test. Lab. (amntl), Elect. Comp. Eng. Dept. at Missouri S&T, Microwave and Millimeter Wave NDT & E Tutorial (http://amntl.mst.edu/).

[29] S. Kharkovsky and R. Zoughi, IEEE Instru. Meas. Mag., **10**, 26 (2007).

[30] Y. Ju, M. Saka, and H. Abe, NDT & E Int., **32**, 259 (1999).

[31] Y. Ju, M. Saka, and H. Abe, NDT & E Int., **34**, 49 (2001).

[32] Y. Ju, M. Saka, and H. Abe, NDT & E Int., **34**, 213 (2001).

[33] Y. Ju, M. Saka, and H. Abe, IEEE T. Instrum. Meas., **50**, 1019 (2001).

[34] Y. Ju, M. Saka, and H. Abe, J. Electron. Packaging, **123**, 42 (2001).

[35] Y. Ju, K. Inoue, M. Saka, and H. Abe, Appl. Phys. Lett., **81**, 3585 (2002).

[36] Y. Ju, Y. Hirosawa, H. Soyama, and M. Saka, Appl. Phys. Lett., **87**, 162102 (2005).

[37] L. Liu and Y. Ju, Rev. Sci. Instrum., **81**, 124701 (2010).

[38] Y. Ju, M. Saka, and Y. Uchimura, NDT & E Int., **38**, 726 (2005).

[39] Y. Ju, T. Kobayashi, and H. Soyama, Microsyst. Technol., **14**, 1021 (2007).

[40] A. Fujimoto, L. Zhang, A. Hosoi, and Y. Ju, Microsyst. Technol., **17**, 715 (2010).

[41] L. Zhang, Y. Ju, A. Hosoi, and A. Fujimoto, Rev. Sci. Instrum., **81**, 123708 (2010).

[42] Y. Ju, L. Liu, and M. Ishikawa, Mater. Sci. Forum, **614**, 111 (2009).

[43] L. Liu and Y. Ju, NDT & E Int., **44**, 106 (2011).

[44] L. Liu, Y. Ju, M. Chen, and D. Fang, Mater. Trans., **52**, 2091 (2011).

[45] K. Abbasi, S. Ito, and H. Hashizume, Int. J. Appl. Electromagn. Mech., **28**, 429 (2008).

[46] K. Abbasi, N. H. Motlagh, M. R. Neamatollahi, and H. Hashizume, Int. J. Pres. Ves. Pip., **86**, 764 (2009).

[47] Agilent Technologies, Time Domain Analysis Using Network Analyzer. Application Note 1287-12, March 2007.

[48] B. Gimeno and M. Guglielmi, Int. J. Microw. Millimet. Wave Comput. Aided Eng., **7**, 180 (1997).

[49] J. K. Piotrowski, Proc. 13 Int. Conf. Microw. Radar Wireless. Commun. 2000 (MIKON-2000), **1**, 333 (2000).

[50] M. Adous, P. Queffelec, and L. Laguerre, Meas. Sci. Tech., **17**, 2241 (2006).

[51] L. Liu, Y. Ju, and M. Chen, Optimizing the frequency range of microwaves for high-resolution evaluation of wall thinning locations in a long-distance metal pipe, *to be submitted*.

Chapter 2. Theory for Microwave NDT of Pipe Wall Thinning (PWT)

During solving the pipe wall thinning (PWT) problem, because a metal pipe under test (PUT) can be taken as a circular waveguide, transmission line theory and mode analysis of microwaves inside a circular waveguide are utilized for analyzing and solving the PWT problem in our research. In addition, as the microwave signals for analysis are obtained by generating microwave signals from a microwave VNA to the PUT utilizing two different coaxial-line sensors designed by ourselves separately for the FDM and TDM applications, basic theories of transmission line, circular waveguide, and coaxial line are introduced and discussed in this chapter.

2.1. Transmission Lines and Waveguides

Firstly, we will study the general properties of transmission line, circular waveguide and coaxial line. In many ways transmission line theory bridges the gap between field analysis and basic circuit theory and is of significant importance in microwave network analysis [1]. The key difference between circuit theory and transmission line theory is the electrical size. Circuit analysis assumes that the physical dimensions of a network are much smaller than the electrical wavelength, while transmission lines may be a considerable fraction of a wavelength, or many wavelengths, in size. Thus a transmission line is a distributed parameter network, where voltages and currents can vary in magnitude and phase over its length.

2.1.1. The Lumped-element Circuit Model for a Transmission Line

The schematic diagrams of a transmission line having a short piece of line of length Δz and its equivalent lamped-element circuit are shown together in Fig. 2.1. Where R, L, G, and C are per unit length quantities of series resistance, series inductance, shunt conductance, and shunt capacitance, respectively. L represents the total self-inductance of the two conductors; C is due to the close proximity of the two conductors; R represents the resistance due to the finite conductivity of the conductors, and G is due to dielectric loss in the material between the conductors [1]. Therefore, R and G represent loss. A finite length of transmission line can be viewed as a cascade of sections of the form of Fig. 2.1(b), where $\omega = 2\pi f$ is the angular frequency.

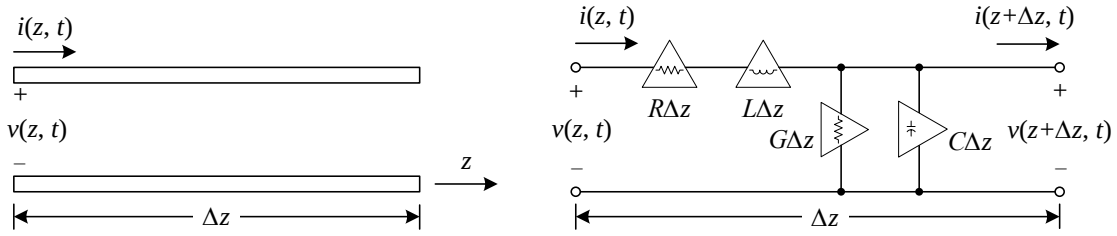

Fig. 2.1. Voltage and current definitions and equivalent circuit for an incremental length of transmission line: (a) Voltage and current definitions; (b) Lumped-element equivalent circuit [1].

For the sinusoidal steady-state condition, the propagation equations of the transmission line can be simplified to [1]

$$\mathrm{d}V(z)/\mathrm{d}z = -(R + \mathrm{j}\omega L)I(z) \tag{2.1a}$$

$$\mathrm{d}I(z)/\mathrm{d}z = -(G + \mathrm{j}\omega C)V(z) \tag{2.1b}$$

The two equations of Eq. (2.1) can be solved simultaneously to give wave equations

for $V(z)$ and $I(z)$:

$$\mathrm{d}^2V(z)/\mathrm{d}z^2 - \gamma^2 V(z) = 0 \tag{2.2a}$$

$$\mathrm{d}^2I(z)/\mathrm{d}z^2 - \gamma^2 I(z) = 0 \tag{2.2b}$$

where γ is the complex propagation constant, which is a function of frequency and can be expressed as

$$\gamma = \alpha + \mathrm{j}\beta = \sqrt{(R + \mathrm{j}\omega L)(G + \mathrm{j}\omega C)} \tag{2.3}$$

The characteristic impedance, Z_0, can be defined as [1]

$$Z_0 = (R + \mathrm{j}\omega L)/\gamma = \sqrt{(R + \mathrm{j}\omega L)/(G + \mathrm{j}\omega C)} \tag{2.4}$$

The wavelength on the line is $\lambda = 2\pi/\beta$, and the phase velocity and group velocity are $v_p = \omega/\beta = \lambda f$ and $v_g = c^2/v_p = (\lambda_0/\lambda)c$, respectively. Where c is the velocity of light in free space, and λ_0 is the wavelength of microwave in free space working at frequency f. As β is generally smaller than k_0, which is the wavenumber in free space, $\lambda > \lambda_0$ is the general case, and as a result, the relationship among these velocities is generally $v_p > c > v_g$.

It should be noted that a transmission line is characterized by a propagation constant and a characteristic impedance; if the line is lossy, attenuation is also of interest. These quantities will be derived by a field theory analysis for the various lines and waveguides.

Different types of wave propagation and modes can exist on transmission lines and waveguides. Transmission lines may support transverse electromagnetic (TEM) waves, characterized by the lack of longitudinal field components. TEM waves have a uniquely defined voltage, current, and characteristic impedance. Waveguides, often consisting of a single conductor, support transverse electric (TE) and/or transverse magnetic (TM) waves, characterized by the presence of longitudinal magnetic or electric, respectively,

field components. It should be noted that a unique definition of characteristic impedance is not possible for TE and TM waves, although definitions can be chosen so that the characteristic impedance concept can be used for waveguides with meaningful results [1].

The geometry of a coaxial line is shown in Fig. 2.2. R_s is the surface resistivity of both the inner and outer conductors, and the material filling the space between the conductors to have a complex permittivity $\varepsilon = \varepsilon' - \mathrm{j}\varepsilon''$ and a permeability $\mu = \mu_0 \mu_r$. The equivalent circuit transmission line parameters are obtained to be [1]

$$L = (\mu / 2\pi)\ln(b/a) \quad \text{H/m}, \quad C = 2\pi\varepsilon' / \ln(b/a) \quad \text{F/m}, \tag{2.5a}$$

$$R = (R_s / 2\pi)(1/a + 1/b) \quad \Omega\text{/m}, \quad G = 2\pi\omega\varepsilon'' / \ln(b/a) \quad \text{S/m}. \tag{2.5b}$$

where R_s is the surface resistance of the conductor.

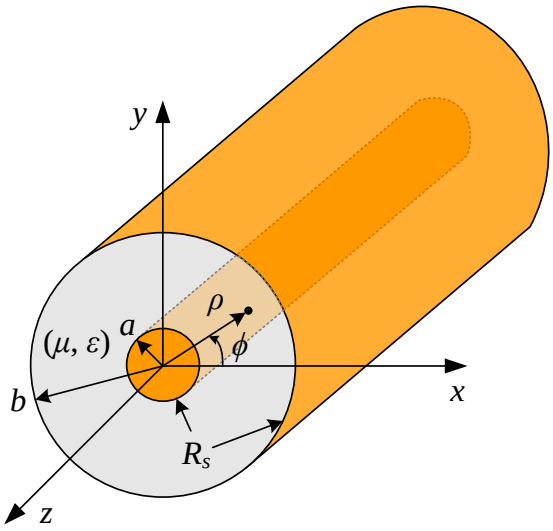

Fig. 2.2. Schematic geometry of a coaxial line.

The propagation constant is $\gamma^2 = -\omega^2 \mu\varepsilon$, which, for lossless media, reduces to [1]

$$\beta = \omega\sqrt{\mu\varepsilon} = \omega\sqrt{LC} \tag{2.6}$$

This is a general result for TEM transmission lines.

The wave impedance is obtained to be

$$Z_\omega = E_\rho / H_\phi = \omega\mu / \beta = \sqrt{\mu / \varepsilon} = \eta \tag{2.7}$$

It is seen to be identical to the intrinsic impedance of the medium, η, and again is a general result for TEM transmission lines.

The characteristic impedance of the coaxial line is defined as

$$Z_0 = V_0 / I_0 = E_\rho \ln(b/a)/(2\pi H_\phi) = \eta \ln(b/a)/(2\pi) = \sqrt{\mu / \varepsilon} \ln(b/a)/(2\pi) \tag{2.8}$$

It is found that the characteristic impedance is geometry dependent and will be different for other transmission line configurations.

Finally, the power flow (in the z direction) on the coaxial line can be computed from the Poynting vector as $P = V_0 I_0^* / 2$. It is clear agreement with circuit theory [1]. This shows that the flow of power in a transmission line takes place entirely via the E and M fields between the two conductors; power is not transmitted through the conductors themselves. For the case of finite conductivity, power may enter the conductors, but this power is then lost as heat and is not delivered to the load.

2.1.2. Lossy Transmission Lines

In practice, all transmission lines have loss due to finite conductivity and/or lossy dielectric, but these losses are usually small. In many practical problems, loss may be neglected, but at times the effect of loss may be of interest, such as when dealing with the attenuation of a transmission line, or the quality factor, *Q*, of a resonant cavity, etc.

When the loss is small, some approximations can be made to simplify the expressions for the general transmission line parameters of $\gamma = \alpha + \mathrm{j}\beta$ and Z_0. For the low-loss line, it can be assumed that $R << \omega L$ and $G << \omega C$ in Eq. (2.3), which means that both the conductor loss and dielectric loss are small. Then $RG << \omega^2 LC$, and Eq. (2.3)

can reduce to

$$\gamma = \mathrm{j}\omega\sqrt{LC}\sqrt{1-\mathrm{j}[R/(\omega L)+G/(\omega C)]} \tag{2.9}$$

Using the first two terms of the Taylor series expansion for $\sqrt{1+x} \approx 1+x/2+\ldots$, the complex propagation constant shown in Eq. (2.9) can be obtained as

$$\gamma \approx \mathrm{j}\{1-\mathrm{j}[R/(\omega L)+G/(\omega C)]/2\}\omega\sqrt{LC} \tag{2.10}$$

So that

$$\alpha \approx (R\sqrt{C/L}+G\sqrt{L/C})/2 = (R/Z_0+GZ_0)/2, \text{ and } \beta \approx \omega\sqrt{LC} \tag{2.11}$$

where $Z_0 = \sqrt{L/C}$ is the characteristic impedance of the lossless transmission line. It should be noted that the propagation constant β is the same as the lossless case. Using the same order of approximation, the characteristic impedance Z_0 expressed in Eq. (2.4) can be approximated as a real quantity:

$$Z_0 = \sqrt{(R+\mathrm{j}\omega L)/(G+\mathrm{j}\omega C)} \approx \sqrt{L/C} \tag{2.12}$$

Equations (2.11) and (2.11) are known as the high-frequency, low-loss approximations for transmission lines, and are important because they show that the propagation constant and characteristic impedance for a low-loss line can be closely approximated by considering the line as lossless.

2.1.3. Attenuation Constant of the Coaxial Line

The transmission line parameters shown in Eq. (2.5) of the coaxial line were derived for a general case (both lossy and lossless cases are included). Assuming the loss is small, the attenuation constant can be calculated from Eqs. (2.11) and (2.5) as follows,

$$\alpha \approx (R\sqrt{C/L}+G\sqrt{L/C})/2 = \{R_s(1/a+1/b)/[\eta\ln(b/a)]+\omega\varepsilon''\eta\}/2 \tag{2.13}$$

where $\eta = \sqrt{\mu/\varepsilon'}$ is the intrinsic impedance of the dielectric material filling the coaxial

line, and $R_s = \mathrm{Re}(\eta) = \mathrm{Re}[(1+\mathrm{j})/(\sigma\delta_s)] = 1/(\sigma\delta_s) = \sqrt{\omega\mu/(2\sigma)}$ is the surface resistance of the conductor. In addition, $\beta = \omega\sqrt{LC} = \omega\sqrt{\mu\varepsilon'}$, and $Z_0 = \sqrt{L/C} = [\eta/(2\pi)]\ln(b/a)$.

2.1.3.1. Perturbation Method for Calculating Attenuation

It should be noted that the above method for the calculation of attenuation requires that the line parameters L, C, R, and G be known. For a more general condition, the perturbation method can be used instead as a standard technique for calculating the attenuation constant of a low-loss line. The method avoids the use of these transmission line parameters, and instead uses the fields of the lossless line, with the assumption that the fields of the lossy line are not greatly different from the fields of the lossless line.

The power flow along a lossy transmission line, in the absence of reflections, can be expressed as [1]

$$P(z) = P_0 \exp(-2\alpha z) \tag{2.14}$$

where P_0 is the power at the $z = 0$ plane, and α is the attenuation constant to be determined. Now define the power loss per unit length along the line as

$$P_l = -\partial P/\partial z = 2\alpha P_0 \exp(-2\alpha z) = 2\alpha P(z) \tag{2.15}$$

where the negative sign on the derivative was chosen so that P_l would be a positive quantity. From this, the attenuation constant can be determined as

$$\alpha = P_l(z)/[2P(z)] = P_l(z=0)/(2P_0) \tag{2.16}$$

Eq. (2.16) shows that α can be determined from P_0, the power on the line, and P_l, the power loss per unit length of line. It is important to realize that P_l can be computed from the fields of the lossless line, and can account for both conductor loss P_c shown in Eq. (2.17) and dielectric loss P_d shown in Eq. (2.18).

$$P_c = (R_s/2)\int_S |\bar{J}_s|^2 \,\mathrm{ds} = (R_s/2)\int_S |\bar{H}_t|^2 \,\mathrm{ds} \tag{2.17}$$

$$P_d = (\sigma/2)\int_V |\bar{E}|^2 \, \mathrm{d}v + (\omega/2)\int_V (\varepsilon'' |\bar{E}|^2 + \mu'' |\bar{H}|^2)\mathrm{d}v \tag{2.18}$$

where $\bar{J}_s$ is the surface current, and $\bar{H}_t$ is the tangential magnetic field. The surface current $\bar{J}_s$ can be found from $\bar{J}_s = \hat{n} \times \bar{H}$ as if the metal were a perfect conductor.

2.1.3.2. Wheeler Incremental Inductance Rule

Another useful technique for the practical evaluation of attenuation due to conductor loss for TEM or quasi-TEM lines is the Wheeler incremental inductance rule [2]. This method is based on the similarity of the equations for the inductance per unit length and resistance per unit length of a transmission line. In other words, the conductor loss of a line is due to current flow inside the conductor which is related to the tangential magnetic field at the surface of the conductor, and thus to the inductance of the line.

The attenuation due to conductor loss can be evaluated as [1]

$$\alpha_c = P_l/(2P_0) = \omega \Delta L/(2Z_0) \tag{2.19}$$

where $P_0 = |I|^2 Z_0/2$ is the total power flow down the line, and Z_0 is the characteristic impedance of the line. ΔL is evaluated as the change in inductance when all conductor walls are receded by an amount $\delta_s/2$.

Since $Z_0 = \sqrt{L/C} = L/\sqrt{LC} = Lv_p$, Eq. (2.19) can be written in terms of the change in characteristic impedance as

$$\alpha_c = \beta \Delta Z_0/(2Z_0) \tag{2.20}$$

where ΔZ_0 is the change in characteristic impedance when all conductor walls are receded by an amount of $\delta_s/2$. Yet another form of the incremental inductance rule can be obtained by using the first two terms of a Taylor series expansion for Z_0. Thus,

$$Z_0(\delta_s/2) \approx Z_0 + (\delta_s/2)(\mathrm{d}Z_0/\mathrm{d}l) \tag{2.21}$$

so that

$$\Delta Z_0 = Z_0(\delta_s/2) - Z_0 = (\delta_s/2)(\mathrm{d}Z_0/\mathrm{d}l) \tag{2.22}$$

where $Z_0(\delta_s/2)$ refers to the characteristic impedance of the line when the walls are receded by $\delta_s/2$, and l refers to a distance into the conductors. Then Eq. (2.20) can be written as

$$\alpha_c = [\beta\delta_s/(4Z_0)](\mathrm{d}Z_0/\mathrm{d}l) = [R_s/(2\eta Z_0)](\mathrm{d}Z_0/\mathrm{d}l) \tag{2.23}$$

This equation is one of the most practical forms of the incremental inductance rule, because the characteristic impedance is known for a wide variety of transmission lines.

2.1.3.3. Attenuation Constant of a Coaxial Line

The perturbation method is utilized to find the attenuation constant of a coaxial line having a lossy dielectric and lossy conductors.

The fields of the lossless coaxial line, for $a < \rho < b$ shown in Fig. 2.2, are [1]

$$\overline{E} = \frac{V_0\hat{\rho}\exp(-\mathrm{j}\beta z)}{\rho\ln(b/a)}, \text{ and } \overline{H} = \frac{V_0\hat{\phi}\exp(-\mathrm{j}\beta z)}{2\pi\rho Z_0}, \tag{2.24}$$

where $Z_0 = [\eta/(2\pi)]\ln(b/a)$ is the characteristic impedance of the coaxial line and V_0 is the voltage across the line at $z = 0$. The power flowing on the lossless line, P_0, is

$$P_0 = (1/2)\,\mathrm{Re}\int_S \overline{E}\times\overline{H}^*\cdot\mathrm{d}\overline{s} = [|V_0|^2/(2Z_0)]\int_{\rho=a}^{b}\int_{\phi=0}^{2\pi}\frac{\rho\mathrm{d}\rho\mathrm{d}\phi}{2\pi\rho^2\ln(b/a)} = |V_0|^2/(2Z_0) \tag{2.25}$$

The P_l shown in Eq. (2.15) comes from conductor loss, P_c, and dielectric loss, P_d, which can be calculated from Eqs. (2.17) and (2.18), respectively, as

$$P_c = (R_s/2)\int_{z=0}^{1}\left[\int_{\phi=0}^{2\pi}|H_\phi(\rho=a)|^2\,a\mathrm{d}\phi + \int_{\phi=0}^{2\pi}|H_\phi(\rho=b)|^2\,b\mathrm{d}\phi\right]\mathrm{d}z = \frac{R_s|V_0|^2(1/a+1/b)}{4\pi Z_0^2}$$

$$P_d = (\omega\varepsilon''/2)\int_V|\overline{E}|^2\,\mathrm{d}v = (\omega\varepsilon''/2)\int_{\rho=a}^{b}\int_{\phi=0}^{2\pi}\int_{z=0}^{1}|E_\rho|^2\,\rho\mathrm{d}\rho\mathrm{d}\phi\mathrm{d}z = \pi\omega\varepsilon''|V_0|^2/\ln(b/a) \tag{2.26}$$

Finally, the attenuation constant can be obtained from Eq. (2.16) as

$$\alpha = (P_c + P_d)/(2P_0) = R_s(1/a + 1/b)/[2\eta \ln(b/a)] + \omega\varepsilon''\eta/2 \quad (2.27)$$

The following part will calculate the attenuation constant due to conductor loss of a coaxial line using the incremental inductance rule.

As the characteristic impedance of a coaxial line is $Z_0 = \eta \ln(b/a)/(2\pi)$, the attenuation due to conductor loss expressed in Eq. (2.23) is [1]

$$\alpha_c = [R_s/(2\eta Z_0)](\mathrm{d}Z_0/\mathrm{d}l) = [R_s/(4\pi Z_0)](1/b + 1/a) \quad (2.28)$$

It agrees with the result shown in Eq . (2.27). However, it should be noted out that the measured attenuation constants for practical lines are usually higher regardless of how attenuation is calculated [1]. The main reason for this discrepancy is the fact that realistic transmission lines have metallic surfaces that are somewhat rough, which increases the loss, while these theoretical calculations assume perfectly smooth conductors. A quasi- empirical formula that can be used to correct for surface roughness for any transmission line is [3]

$$\alpha_c' = \alpha_c\{1 + (2/\pi)\tan^{-1}[1.4(\Delta/\delta_s)^2]\} \quad (2.29)$$

where α_c is the attenuation due to perfectly smooth conductors, α_c' is the attenuation corrected for surface roughness, Δ is the rms surface roughness, and δ_s is the skin depth of the conductors.

2.1.3.4. Attenuation Due to Dielectric Loss

As mentioned above, attenuation in a transmission line or waveguide can be caused by either dielectric loss or conductor loss. If α_d is the attenuation constant due to dielectric loss, and α_c is the one due to conductor loss, then the total one is $\alpha = \alpha_d + \alpha_c$.

Attenuation caused by conductor loss can be calculated using the perturbation method shown above, and this loss depends on the field distribution in the guide and so must be

evaluated separately for each type of transmission line or waveguide. However, if the line or guide is completely filled with a homogeneous dielectric, the attenuation due to lossy dielectric can be calculated from the propagation constant, and this result will apply to any guide or line with a homogeneous dielectric filling.

Therefore, using the complex dielectric constant allows the complex propagation constant to be written as [1]

$$\gamma = \alpha_d + \mathrm{j}\beta = \sqrt{k_c^2 - \omega^2 \mu_0 \varepsilon_0 \varepsilon_r (1 - \mathrm{j}\tan\delta)} \tag{2.30}$$

where $\sqrt{k_c^2 - \omega^2 \mu_0 \varepsilon_0 \varepsilon_r} = \sqrt{k_c^2 - k^2} = \mathrm{j}\beta$, and $k^2 = \omega^2 \mu_0 \varepsilon_0 \varepsilon_r$ is the (real) wavenumber in the absence of loss.

In practice, most dielectric materials have a very small loss, i.e. $\tan\delta << 1$, so this expression can be simplified by using the first two terms of the Taylor expansion as [1]

$$\gamma = \sqrt{k_c^2 - k^2 + \mathrm{j}k^2 \tan\delta} \approx \sqrt{k_c^2 - k^2} + \mathrm{j}k^2 \tan\delta / (2\sqrt{k_c^2 - k^2}) = k^2 \tan\delta / (2\beta) + \mathrm{j}\beta \tag{2.31}$$

Eq. (2.31) shows that when the loss is small, the phase constant, β, is unchanged, while the attenuation constant due to dielectric loss is given by

$$\alpha_d = k^2 \tan\delta / (2\beta) \quad \text{(for TE or TM waves)} \tag{2.32}$$

It should be noted that this equation can also be used for TEM lines, where $k_c = 0$ and $\beta = k$.

2.2. Circular Waveguide

A hollow metal tube of circular cross section also supports TE and TM waveguide modes. Fig. 2.3 shows the cross-section geometry of such a circular waveguide of inner radius a. It is appropriate to employ cylindrical coordinates, and the components of the

transverse fields can be derived from the longitudinal components as

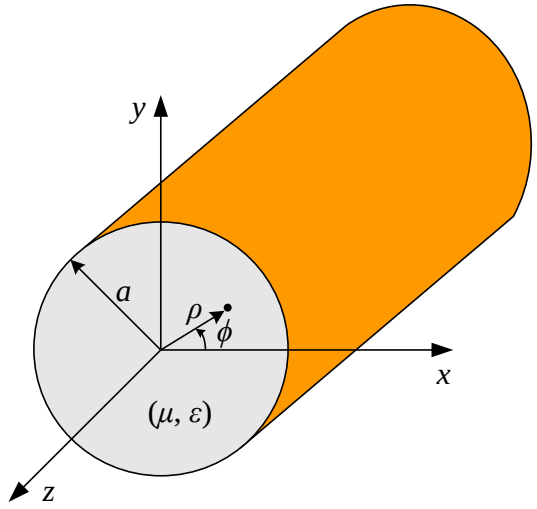

$$E_\rho = \frac{-\mathrm{j}}{k_c^2}\left(\beta\frac{\partial E_z}{\partial\rho} + \frac{\omega\mu}{\rho}\frac{\partial H_z}{\partial\phi}\right) \quad (2.33a)$$

$$E_\phi = \frac{-\mathrm{j}}{k_c^2}\left(\frac{\beta}{\rho}\frac{\partial E_z}{\partial\phi} - \omega\mu\frac{\partial H_z}{\partial\rho}\right) \quad (2.33b)$$

$$H_\rho = \frac{\mathrm{j}}{k_c^2}\left(\frac{\omega\varepsilon}{\rho}\frac{\partial E_z}{\partial\phi} - \beta\frac{\partial H_z}{\partial\rho}\right) \quad (2.33c)$$

$$E_\phi = \frac{-\mathrm{j}}{k_c^2}\left(\omega\varepsilon\frac{\partial E_z}{\partial\rho} + \frac{\beta}{\rho}\frac{\partial H_z}{\partial\phi}\right) \quad (2.33d)$$

Fig. 2.3. Geometry of a circular waveguide.

where $k_c^2 = k^2 - \beta^2$, and $e^{-\mathrm{j}\beta z}$ propagation has been assumed. For $e^{+\mathrm{j}\beta z}$ propagation, replace β with $-\beta$ in all expressions.

2.2.1. TE Modes

For TE modes, $E_z = 0$, and H_z is a solution to the wave equation,

$$\nabla^2 H_z + k^2 H_z = 0 \quad (2.34)$$

If $H_z(\rho,\phi,z) = h_z(\rho,\phi)e^{-\mathrm{j}\beta z}$, Eq. (2.34) can be expressed in cylindrical coordinates as

$$\left(\frac{\partial^2}{\partial\rho^2} + \frac{1}{\rho}\frac{\partial}{\partial\rho} + \frac{1}{\rho^2}\frac{\partial^2}{\partial\phi^2} + k_c^2\right)h_z(\rho,\phi) = 0 \quad (2.35)$$

Again, a solution can be derived using the method of separation of variables. Thus,

$$h_z(\rho,\phi) = R(\rho)\Phi(\phi) \quad (2.36)$$

and when substituting it into Eq. (2.35), the following equation is obtained

$$\frac{\rho^2}{R}\frac{\partial^2 R}{\partial\rho^2} + \frac{\rho}{R}\frac{\partial R}{\partial\rho} + k_c^2\rho^2 = \frac{-1}{\Phi}\frac{\partial^2\Phi}{\partial\phi^2} \quad (2.37)$$

The left side of this equation depends on ρ (not ϕ), while the right side depends only on ϕ. Thus, each side must be equal to a constant, which we will call k_ϕ^2. Then,

$$\partial^2\Phi/\partial\phi^2 + k_\phi^2\Phi = 0 \tag{2.38}$$

and

$$\rho^2(\partial^2 R/\partial\rho^2) + \rho(\partial R/\partial\rho) + \left(\rho^2 k_c^2 - k_\phi^2\right)R = 0 \tag{2.39}$$

The general solution to Eq. (2.38) is

$$\Phi(\phi) = A\sin k_\phi\phi + B\cos k_\phi\phi \tag{2.40}$$

Since the solution to h_z must be periodic in ϕ, i.e. $h_z(\rho,\phi) = h_z(\rho,\phi \pm 2m\pi)$, k_ϕ must be an integer, *n*. Thus, Eq. (2.40) becomes

$$\Phi(\phi) = A\sin n\phi + B\cos n\phi \tag{2.41}$$

while Eq. (2.39) becomes

$$\rho^2\frac{\partial^2 R}{\partial\rho^2} + \rho\frac{\partial R}{\partial\rho} + \left(\rho^2 k_c^2 - n^2\right)R = 0 \tag{2.42}$$

which is Bessel's differential equation. The solution is

$$R(\rho) = CJ_n(k_c\rho) + DY_n(k_c\rho) \tag{2.43}$$

where $J_n(x)$ and $Y_n(x)$ are the Bessel functions of first and second kinds, respectively. Since $Y_n(k_c\rho)$ becomes infinite at $\rho = 0$, this term is physically unacceptable for the circular waveguide problem, so that $D = 0$. The solution for can then be written as

$$h_z(\rho,\phi) = (A\sin n\phi + B\cos n\phi)J_n(k_c\rho) \tag{2.44}$$

where the constant *C* of Eq. (2.43) has been absorbed into the constants *A* and *B* of Eq. (2.44). We must still determine the cutoff wavenumber k_c, which we can do by enforcing the boundary condition that $E_{\tan} = 0$ on the waveguide wall. Since $E_z = 0$, we must

have that

$$E_\phi(\rho,\phi)=0,\ \text{at}\ \ \rho=a \tag{2.45}$$

From Eq. (2.33b), we find E_ϕ from H_z as

$$E_\phi(\rho,\phi,z)=(\mathrm{j}\omega\mu/k_c)(A\sin n\phi+B\cos n\phi)J_n'(k_c\rho)\exp(-\mathrm{j}\beta z) \tag{2.46}$$

where the notation $J_n'(k_c\rho)$ refers to the derivative of Bessel function J_n with respect to its argument. For E_ϕ to vanish at the conductor surface $\rho=a$, we must have

$$J_n'(k_c a)=0 \tag{2.47}$$

If the roots of $J_n'(x)$ are defined as p_{nm}', so that $J_n'(p_{nm}')=0$, where p_{nm}' is the *m*th root of J_n', then k_c must have the value

$$k_{c_{nm}}=p_{nm}'/a \tag{2.48}$$

Values of p_{nm}' are given in mathematical tables, and the first few values are listed in TABLE 2.1.

TABLE 2.1. Values of p_{nm}' for TE modes of a circular waveguide

n	p_{n1}'	p_{n2}'	p_{n3}'	p_{n4}'	p_{n5}'	p_{n6}'	p_{n7}'	p_{n8}'	p_{n9}'
0	3.8317	7.0156	10.1735	13.3237	16.4706	19.6159	22.7601	25.9037	29.0468
1	1.8412	5.3314	8.5363	11.7060	14.8636	18.0155	21.1644	24.3113	27.4571
2	3.0542	6.7061	9.9695	13.1704	16.3475	19.5129	22.6716	25.8260	28.9777
3	4.2012	8.0152	11.3459	14.5858	17.7887	20.9725	24.1449	27.3101	30.4703
4	5.3176	9.2824	12.6819	15.9641	19.1960	22.4010	25.5898	28.7678	31.9385
5	6.4156	10.5199	13.9872	17.3128	20.5755	23.8036	27.0103	30.2028	33.3854
6	7.5013	11.7349	15.2682	18.6374	21.9317	25.1839	28.4098	31.6179	34.8134
7	8.5778	12.9324	16.5294	19.9419	23.2681	26.5450	29.7907	33.0152	36.2244
8	9.6474	14.1155	17.7740	21.2291	24.5872	27.8893	31.1553	34.3966	37.6201
9	10.7114	15.2867	19.0046	22.5014	25.8913	29.2186	32.5052	35.7638	39.0019

The TE_{nm} modes are thus defined by the cutoff wavenumber, $k_{c_{nm}}=p_{nm}'/a$, where

n refers to the number of circumferential variations, ϕ, and m refers to the number of radial variations, ρ. The propagation constant of the TE_{nm} mode is

$$\beta_{nm} = \sqrt{k^2 - k_c^2} = \sqrt{k^2 - (p'_{nm}/a)^2} \tag{2.49}$$

with a cutoff frequency of

$$f_{c_{nm}} = k_{c_{nm}}/(2\pi\sqrt{\mu\varepsilon}) = p'_{nm}/(\pi d\sqrt{\mu\varepsilon}) \tag{2.50}$$

where $d = 2a$ is the inner diameter of the circular waveguide.

The first TE mode to propagate is the mode with the smallest value of p'_{nm}, which from TABLE 2.1 is seen to be the TE_{11} mode. This mode is then the dominant mode, and the one most frequently used. As $m \geq 1$, there is no TE_{10} mode, but there is a TE_{01} mode.

The wave impedance can be obtained as

$$Z_{\mathrm{TE}} = E_\rho / H_\phi = -E_\phi / H_\rho = \eta k / \beta \tag{2.51}$$

It is noted that the above solutions have two remaining arbitrary amplitude constants, A and B. These constants control the amplitude of the $\sin(n\phi)$ and $\cos(n\phi)$ terms, which are independent. That is, because of the azimuthal symmetry of the circular waveguide, both of them are valid solutions, and can be present in a specific problem to any degree. The actual amplitudes of these terms will be dependent on the excitation of the waveguide. From a different viewpoint, the coordinate system can be rotated about the *z*-axis to obtain an h_z with either $A = 0$ or $B = 0$.

Now consider the dominant TE_{11} mode with an excitation such that $B = 0$. The power flow down the waveguide can be computed as [1]

$$P_0 = \pi\omega\mu\,|A|^2\,\mathrm{Re}(\beta)(p'^2_{11} - 1)J_1^2(k_c a)/(4k_c^4) \tag{2.52}$$

which is seen to be nonzero only when β is real, corresponding to a propagating mode.

Attenuation due to dielectric loss is given by Eq. (2.32). The attenuation due to a

lossy waveguide conductor can be obtained by computing the power loss per unit length of guide,

$$\begin{aligned} P_l &= (R_s/2)\int_{\phi=0}^{2\pi} |\bar{J}_s|^2 \, a\mathrm{d}\phi = (R_s/2)\int_{\phi=0}^{2\pi} (|H_\phi|^2 + |H_z|^2) a\mathrm{d}\phi \\ &= (\pi |A|^2 \, R_s a/2)[1+\beta^2/(k_c^4 a^2)]J_1^2(k_c a) \end{aligned} \tag{2.53}$$

The attenuation constant per unit length is then

$$\alpha_c = P_l/(2P_0) = R_s(k_c^4 a^2 + \beta^2)/[\eta k \beta a(p_{11}'^2 - 1)] = [R_s/(\eta k \beta a)][k_c^2 + k^2/(p_{11}'^2 - 1)] \tag{2.54}$$

2.2.2. TM Modes

For the TM modes of the circular waveguide, we must solve for E_z from the wave equation in cylindrical coordinates,

$$\left(\frac{\partial^2}{\partial\rho^2} + \frac{1}{\rho}\frac{\partial}{\partial\rho} + \frac{1}{\rho^2}\frac{\partial^2}{\partial\phi^2} + k_c^2\right) e_z(\rho,\phi) = 0 \tag{2.55}$$

where $E_z(\rho,\phi,z) = h_z(\rho,\phi)e^{-\mathrm{j}\beta z}$, and $k_c^2 = k^2 - \beta^2$. Using the same method as solving Eq. (2.35), the general solutions can be obtained as,

$$e_z(\rho,\phi) = (A\sin n\phi + B\cos n\phi)J_n(k_c\rho) \tag{2.56}$$

The difference from the TE solution is that the boundary condition becomes,

$$E_z(\rho,\phi) = 0, \text{ at } \rho = a \tag{2.57}$$

Thus, we must have

$$J_n(k_c a) = 0 \tag{2.58}$$

or

$$k_c = p_{nm}/a \tag{2.59}$$

where p_{nm} is the *m*th root of $J_n(x)$, i.e. $J_n(p_{nm}) = 0$. Values of p_{nm} are given in mathematical tables, and the first few values are listed in TABLE 2.2.

TABLE 2.2. Values of p_{nm} for TM modes of a circular waveguide

n	p_{n1}	p_{n2}	p_{n3}	p_{n4}	p_{n5}	p_{n6}	p_{n7}	p_{n8}	p_{n9}
0	2.4048	5.5201	8.6537	11.7915	14.9309	18.0711	21.2116	24.3525	27.4935
1	3.8317	7.0156	10.1735	13.3237	16.4706	19.6159	22.7601	25.9037	29.0468
2	5.1356	8.4172	11.6198	14.7960	17.9598	21.1170	24.2701	27.4206	30.5692
3	6.3802	9.7610	13.0152	16.2235	19.4094	22.5827	25.7482	28.9084	32.0649
4	7.5883	11.0647	14.3725	17.6160	20.8269	24.0190	27.1991	30.3710	33.5371
5	8.7715	12.3386	15.7002	18.9801	22.2178	25.4303	28.6266	31.8117	34.9888
6	9.9361	13.5893	17.0038	20.3208	23.5861	26.8202	30.0337	33.2330	36.4220
7	11.0864	14.8213	18.2876	21.6415	24.9349	28.1912	31.4228	34.6371	37.8387
8	12.2251	16.0378	19.5545	22.9452	26.2668	29.5457	32.7958	36.0256	39.2404
9	13.3543	17.2412	20.8070	24.2339	27.5837	30.8854	34.1544	37.4001	40.6286

The first TM mode to propagate is the TM_{01} mode with $p_{01} = 2.4048$, which is the dominant TM modes. Meanwhile, since $p_{01} = 2.4048$ is greater than $p'_{11} = 1.8412$ of the lowest order TE_{11} mode, the TE_{11} mode is the dominant mode of the circular waveguide.

The wave impedance can be obtained as [1]

$$Z_{\mathrm{TM}} = E_\rho / H_\phi = -E_\phi / H_\rho = \eta\beta / k \tag{2.60}$$

The propagation constant of the TM_{nm} mode is

$$\beta_{nm} = \sqrt{k^2 - k_c^2} = \sqrt{k^2 - (p_{nm}/a)^2} \tag{2.61}$$

with a cutoff frequency of

$$f_{c_{nm}} = k_{c_{nm}} / (2\pi\sqrt{\mu\varepsilon}) = p_{nm} / (\pi d\sqrt{\mu\varepsilon}) \tag{2.62}$$

where $d = 2a$ is the inner diameter of the circular waveguide.

In addition, field lines for some of the lowest order TE and TM modes are shown in Fig. 2.4.

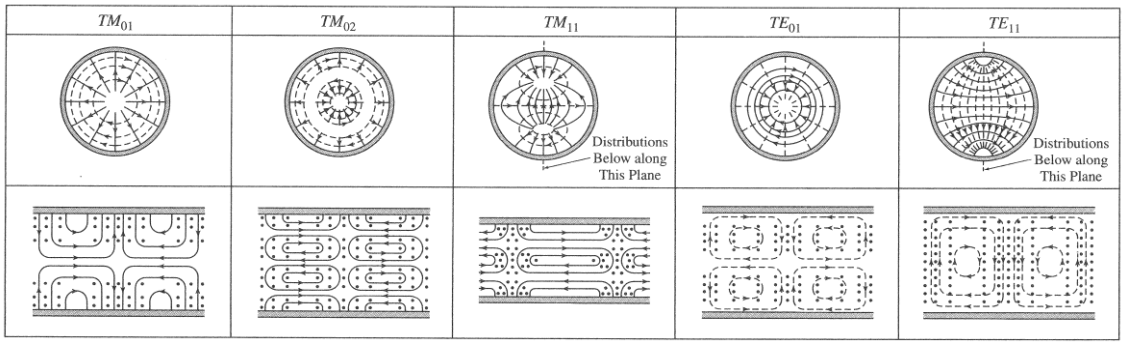

Fig. 2.4. Field lines for some of the lower order modes of a circular waveguide [1].

2.2.3. Wavelength and Velocity

2.2.3.1. Wavelength in the Circular Waveguide

The wavelengths for both TE and TM modes have the same form.

The cutoff wavelengths for both TE and TM modes are expressed as [1],

$$\lambda_c = 2\pi / k_c \tag{2.63}$$

and the wavelengths in the waveguide for TE and TM modes are [1]

$$\lambda_g = 2\pi / \beta \tag{2.64}$$

Because $\beta = \sqrt{k^2 - k_c^2} < k$, it can be found that $\lambda_g > 2\pi / k = \lambda$ for both TE and TM modes, where $\lambda = 2\pi / k$ is the wavelength of plane waves propagating in the medium or material filling the waveguide.

2.2.3.2. Phase Velocity and Group Velocity

The phase velocities for both TE and TM modes also have the same form.

The phase velocities for both TE and TM modes are expressed as [1],

$$v_p = \omega / \beta \tag{2.65}$$

Because $\beta < k$, it can be found that $v_p > \omega/k = \lambda f = v$ for both TE and TM modes, where $v = \lambda f$ is the velocity of plane waves propagating in the medium/material filling the waveguide. In addition, the group velocities for both TE and TM modes are

$$v_g = v^2 / v_p = (\beta / k)v \tag{2.66}$$

It is found from Eqs. (2.65) and (2.66) that the relations between these three velocities are $v_g < v < v_p$.

2.3. Summary

In this chapter, basic theory for transmission lines and circular waveguides is presented in detail. Moreover, general method for evaluating attenuation constants in coaxial line and waveguides is also introduced.

Because a metal pipe can be taken as a circular waveguide, the full-wave analysis of circular waveguide is demonstrated in detail in this part. In addition, not only the field analysis of TE and TM modes, but also the wavelengths and velocities of the circular waveguide are introduced.

All of the contents of this chapter are prepared for a thorough full-wave analysis and insight understanding of the significant work presented in later chapters.

References

[1] D. M. Pozar, Microwave Engineering (2nd Ed), New York: John Wiley & Sons, (1998).

[2] H. A. Wheeler, Proc. IRE, **28**, 412 (1942).

[3] T. C. Edwards, Foundations for Microstrip Circuit Design, New York: John Wiley & Sons, (1987).

Chapter 3. Frequency Domain Measurement (FDM) for PWT Depth Evaluation

Abstract

We report an efficient microwave nondestructive testing and evaluation (NDT&E) method to measure the pipe wall thinning (PWT) depths of PWT defects remotely in a long-distance metal pipe. A microwave vector network analyzer (VNA) and a self-designed transmitting and receiving (T&R) coaxial-line sensor were employed to work at S12 mode in the experiment to generate microwave signals propagating in the pipe where the frequency was swept from 14.00 to 14.20 GHz. A brass pipe with inner diameter of 17.03 mm, 1.0 mm wall thickness, 2.0 m length, and connected respectively with 6 joints having the length of 17.0 mm and PWT depths from 0 to 60% of wall thickness was measured. By taking the pipe as a circular waveguide of microwave, after building up a resonance condition and then solving the resonance equations, the evaluation of PWT was realized. By comparing the evaluated results obtained using our suggested method with the nominal inner diameters of the joints, the maximum evaluation error is found to be less than 0.05 mm, which is less than 0.294% of the inner diameter of the pipe, which indicates that a high precision evaluation method is established.

Keywords:

Microwave, pipe wall thinning (PWT), metal pipe, nondestructive testing and evaluation (NDT&E), resonance frequency

3.1. Introduction

Metal pipes are used widely in industry, such as oil and gas transportation, chemical industry and various kinds of power plants. Since the decade before last, accidents caused by pipe wall-thinning (PWT) have been reported frequently all over the world. PWT is one of the most serious defects in pipes used in industry [1,2]. Efficiently detecting and quantitatively evaluating the PWT depths in the pipes is a very important issue for predicting the lifetime of pipes and avoiding severe accidents economically.

Recently, many NDT techniques, such as x-ray [3], electrical potential drop [4], ultrasonic [5,6], magnetic flux leakage [7], eddy current testing [8] and so on, have been used for the measurement of PWT. However, except for the hollow cylindrical guided wave (HCGW) of ultrasonic method [6], all of them can only inspect a pipe locally. Even though HCGW can propagate a long distance along an isolated pipe, the ultrasonic energy will attenuate much faster when there are many girth welds on the surface of the pipe [9]. Besides, all of the aforementioned methods are difficult to measure pipes buried under ground, in walls of some structures, or under other buried conditions. This is the main shortage for the HCGW method, because the ultrasonic energy will attenuate much faster in the pipe surrounded by different kinds of media such as earth, concrete, or water [10]. As a result, all the existing methods generally take lots of time and labor to inspect a large scale pipe under many practical conditions.

Microwave can be used to overcome the shortcomings of the mentioned methods above, because it can propagate a very long distance with quite little attenuation in the medium of air, petroleum, gasoline, or any other low-loss dielectric materials. In microwave inspection, a metal pipe under test can be taken as a circular waveguide [11],

and all the energy of the propagating microwave is confined inside the pipe so that the propagation and attenuation of microwave in the pipe are independent of the pipe's surrounding conditions. The time of flight (TOF) of microwave has been used to detect the locations of cracks in the pipe [12,13], however, the degree of PWT is generally more important than its location for predicting the life time of the pipe. In our previous work [11], the PWT depth in a metal pipe was firstly detected utilizing the resonance phenomenon of microwave at a short-end condition with high microwave frequencies, and the possibility to quantitatively evaluate the PWT using microwaves was proved by comparing the experimental and theoretical analysis results. In this study, we focus on establishing a systematic nondestructive evaluation method using microwaves to inspect a pipe in a large scale at an open-end condition and to measure the PWT remotely with the dominant mode frequencies. After confirming the working mode of microwave for certain frequencies, the wavelength of microwave in a waveguide is a function of the frequency and the inner diameter of the pipe [14]. As a result, after determining the wavelength of microwave at the PWT part, the inner diameter including the direct information of the PWT depth can be evaluated. By tracing the route of microwave propagating in the pipe, the resonance condition of microwaves propagating in the pipe is established, and then by solving the resonance equations, the PWT depths are quantitatively evaluated.

3.2. Experimental Approach

The experimental instrument is composed of a microwave vector network analyzer (VNA) and a self-designed transmitting and receiving (T&R) coaxial-line sensor. The

microwave VNA is utilized to work at S12 mode to measure the resonance conditions in the pipe. The photograph of the instrument is shown in Fig. 3.1, and the schematic diagram of the measured pipe is shown in Fig. 3.2. The pipe specimens consist of a brass pipe with inner diameter of $d_1 = 17.03$ mm, wall thickness of $t = 1.0$ mm and length of $l_1 = 2.0$ m, and six joints with a length of $l_2 = 17.0$ mm and inner diameters of d_2. These six joints with different inner diameters which are numbered as No. 1 to No. 6 successively act as different PWT conditions. The nominal values of the inner diameters of the joints are shown in TABLE 3.1. In the case of No. 1 joint, its PWT value is zero, i.e., the inner diameter of which is the same as that of the pipe, $d_2 = d_1$. The schematic diagram of the PWT joint connecting with the pipe is shown in Fig. 3.2.

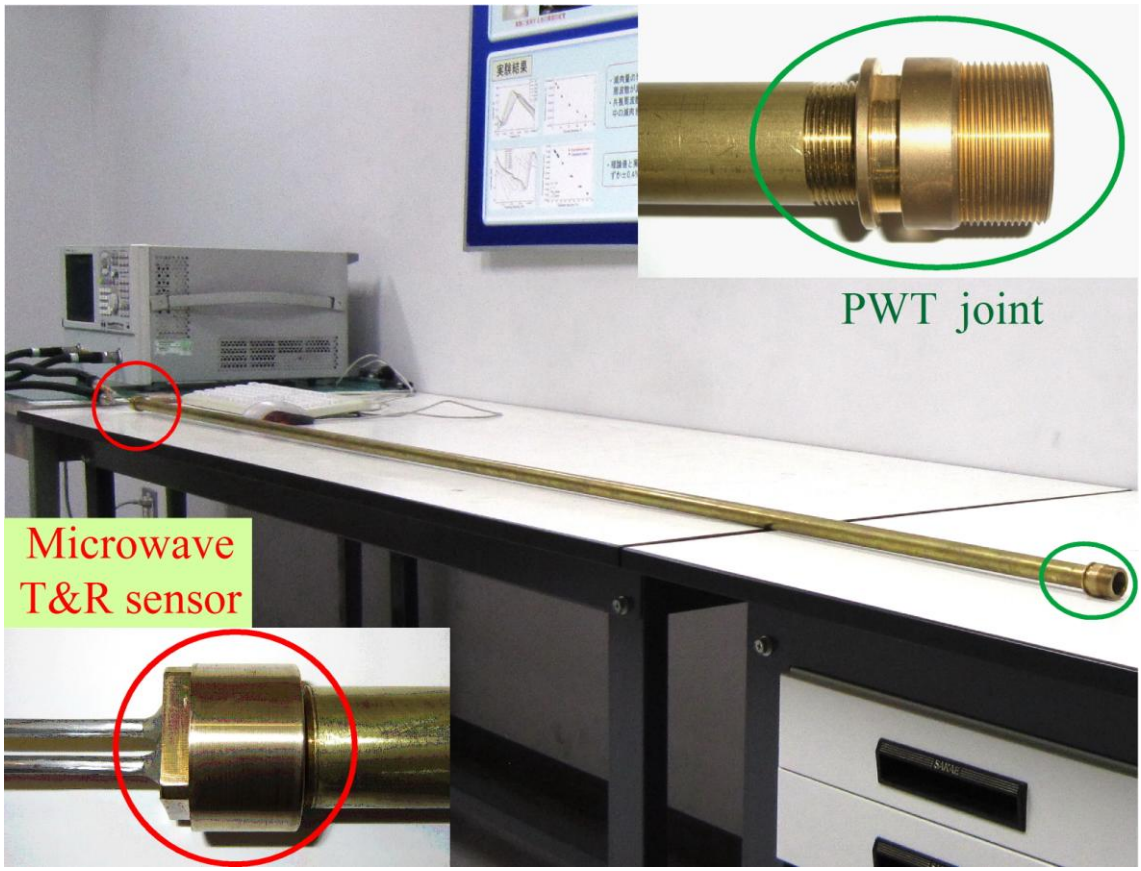

Fig. 3.1. Overall photograph of the experimental instrument.

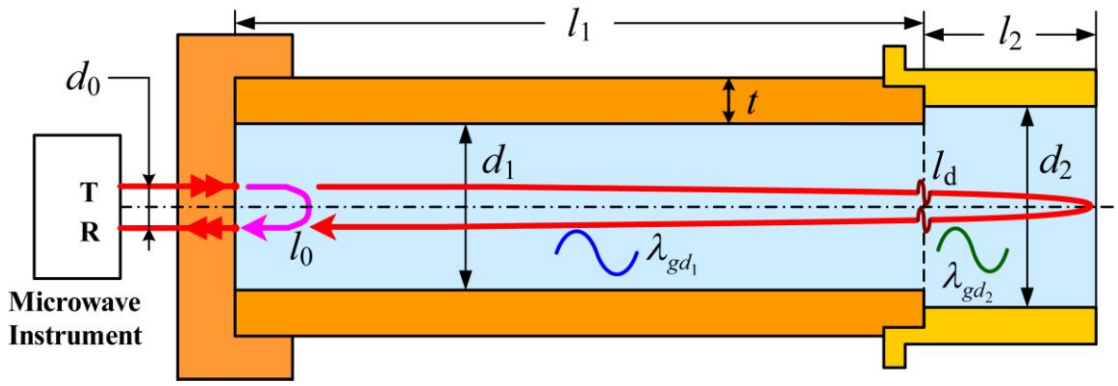

Fig. 3.2. Schematic diagram of interference mechanism in a pipe that having a PWT defect.

The "Microwave Instrument" in Fig. 3.2 refers to the microwave VNA, and the T and R represent transmitting and receiving port of the sensor, respectively. Symbol d_0 is the distance between the two ports; l_0 is the length of path along which microwaves propagate directly to the receiving port; d_1 is the inner diameter of pipe without PWT and having the length l_1; d_2 is the inner diameter of the PWT joint with a constant PWT value and having the length l_2; t is the wall thickness of the pipe. Symbols λ_{gd_1} and λ_{gd_2} are the wavelengths of the microwaves propagating in the pipe at the areas without and with PWT respectively, and l_d is an introduced fictitious length corresponding to the phase shift occurred due to the discontinuity at the abrupt wall-thinning interface.

TABLE 3.1. Detailed geometric parameters of the joints.

Joint's no.	1	2	3	4	5	6
Diameter, d_2 (mm)	17.03	17.10	17.20	17.40	17.80	18.20
PWT degree, %t	0	3.5 %t	8.5 %t	18.5 %t	38.5 %t	58.5 %t

Frequency domain measurement is employed in the proposed method. During the experiment, the microwaves generated by the microwave VNA were coupled into the pipe through the transmitting port of the T&R coaxial-line sensor. The experiments were carried out on the pipe connecting respectively with each of the PWT joints shown in TABLE 3.1. The interference results of the microwaves reflected from the terminal of the PWT joint (after propagating along the pipe) and those going directly to the receiving port (without propagating along the pipe) were detected by the receiving port of the sensor. When sweeping the frequency within a proper range, the corresponding amplitudes containing information of the resonance frequencies were measured and recorded. The resonance frequencies were used as the input parameters of the theoretical analysis to evaluate the PWT degrees quantitatively.

3.3. Theoretical Analysis

3.3.1. Resonance Condition and Resonance Equations

To evaluate the PWT quantitatively using microwave, the crucial hint for analysis is the resonance condition at the receiving port. The resonance condition is built up by the microwave signals reflected from the terminal of the pipe and those going directly to the receiving port along a route with length $l_0 = F(\lambda_{gd_1})d_0$. $F(\lambda_{gd_1})$ is a dimensionless function of the wavelength in the pipe without PWT with values larger than 1. The expression of l_0 is based on the fact that the larger d_0 corresponds to the larger l_0 while $d_0 \to 0$ corresponds to $l_0 \to 0$. In addition, the terminal condition in the measurement is not under the ideal open circuit condition which introduces a fictitious length at the end of the pipe. For conciseness, the influence at the terminal is counted in

the length l_0 and expresses the combined l_0 approximately as $l_0 = G(\lambda_{gd_1})$.

When taking $l_{Total} = l_1 + l_2$ and expressing the propagation route in terms of wavelengths, the equation for the difference of the distance that microwaves propagate along the two routes can be written as follows,

$$2l_{Total} - l_0(f_q) + 2l_d(f_q) = (m+x)\cdot\lambda_{gd_1}(f_q) + (n+y)\cdot\lambda_{gd_2}(f_q) \tag{3.1}$$

where $m, n \in N$ and $0 \le x, y < 1$.

N is the set of natural number. f_q is the qth resonance frequency of the pipe connected with a PWT joint. The term $(m+x)\lambda_{gd_1}$ refers to the difference of distance between the two different routes in the pipe at the part without PWT, in which the integer m is the number of full wavelength, and the proper fraction x means the fraction of a full wavelength. Similarly, $(n+y)\lambda_{gd_2}$ refers to length of the roundabout trip along which microwave propagates in the joint with PWT, in which n and y have the similar meanings as m and x.

Considering the differences of distance that microwaves propagating in the pipe at the parts without and with PWT, respectively, Eq. (3.1) can be written in the separated form as

$$\begin{cases} 2l_1 - l_0(f_q) = (m+x)\cdot\lambda_{gd_1}(f_q) \\ 2l_2 + 2l_d(f_q) = (n+y)\cdot\lambda_{gd_2}(f_q) \end{cases} \tag{3.2}$$

It is known that when the microwave propagates a full wavelength, its phase will change 2π. The phase change in Eq. (3.2) can be expressed as

$$\begin{cases} (m+x)\lambda_{gd_1}/\theta_1 = \lambda_{gd_1}/(2\pi) \\ (n+y)\lambda_{gd_2}/\theta_2 = \lambda_{gd_2}/(2\pi) \end{cases} \tag{3.3}$$

therefore,

$$\begin{cases} \theta_1 = 2\pi(m+x) \\ \theta_2 = 2\pi(n+y) \end{cases} \tag{3.4}$$

θ_1 and θ_2 refer to the phase changes in the roundabout trips along the pipe at the parts without and with PWT, respectively.

Therefore, the whole difference of phase change for microwave propagating along the two routes expressed in Eq. (3.1) can be expressed as

$$\theta = \theta_1 + \theta_2 = 2\pi(m+x+n+y) \tag{3.5}$$

The resonance happens when the difference of phase change equals to integer times of 2π. Therefore, the resonance condition can be derived

$$q = (m+n+x+y) \in N \tag{3.6}$$

Taking the integral values of m and n into account, Eq. (3.6) can be written in a simpler form as

$$x + y = 1 \tag{3.7}$$

Eqs. (3.6) and (3.7) show that the resonance condition is formed only when the difference of the distance that microwave propagates along the two routes in the pipe is integer times (q times) of wavelength, i.e., the two routes of microwave signals can form the resonance only when they having the phase difference of $2\pi q$.

For microwaves propagating along the two routes in the pipe connected with the joint without PWT, l_d in Eq. (3.1) equals to zero. The equation describing the difference of distance can then be written as follows,

$$2l_{Total} - l_0(f_q') = q \cdot \lambda_{gd_1}(f_q') \tag{3.8}$$

where f_q' is the resonance frequency of the pipe connected with the joint without PWT,

and q is the same as that of the pipe connected with a PWT joint.

3.3.2. Solution of the Resonance Equations

The wavelength in a circular waveguide has a relation with the working mode of microwave at applied frequencies and can be expressed as [14]

$$\lambda_g = 1\Big/\sqrt{\mu\varepsilon f^2 - \left[p_{nm}/(\pi d)\right]^2} \tag{3.9}$$

where the μ and ε are the permeability and the permittivity of the medium in the pipe; f is the operating frequency; d is the inner diameter of the pipe; p_{nm} is the mth root of the first kind Bessel function $J_n(x)$ for TM modes, i.e., $J_n(p_{nm}) = 0$ [14]. Air is used as the medium in our experiment, as a result $\mu = \mu_0 = 4\pi \times 10^{-7}$ H/m and $\varepsilon = \varepsilon_0 = 8.854 \times 10^{-12}$ F/m.

When the microwave signal is introduced directly into the pipe through a coaxial line sensor, the electromagnetic field at the terminal of the coaxial line sensor determines that the working modes existing in the circular waveguide are all TM modes, and among which the dominant mode is TM_{01}-mode. When sweeping the frequency between the cut-off frequency of the dominant mode and that of the first higher order TM mode, only the TM_{01}-mode exists. In the experiment, only the frequency ranges of the TM_{01}-mode were used, for which it is $p_{01} = 2.4048$.

3.3.2.1. Determining the Propagation Variable l_0

As mentioned in Sect. 3.3.1, $l_0 = G(\lambda_{gd_1})$ is the equivalent propagation route introduced by the distance between the T&R ports of the sensor and the terminal condition, in which $G(\lambda_{gd_1})$ is a function of the wavelength in the pipe without PWT. It should be calibrated before the quantitative evaluation. A method to determine l_0 is established and demonstrated in detail in this section.

To make the total length the same as the pipe connecting respectively with different PWT joints so as to make the values of q in Eq. (3.8) the same as that in Eq. (3.1) and (3.2), the calibration was carried out by connecting the pipe with the joint without PWT (joint No. 1) to determine the l_0 and q in Eq. (3.8).

In order to increase the calibration precision, the sweeping frequency range containing ten neighboring resonance frequencies (NRFs) was measured in the experiment. For the ten NRFs, q can be expressed as q_0 to q_0+9 in Eq. (3.8). When the resonance frequencies are extracted from the experimental results, the corresponding wavelengths in the pipe without PWT can be calculated using Eq. (3.9).

After the ten wavelengths corresponding to the NRFs have been determined, the q_0 and $l_0(f'_{q_0})$ are firstly solved from Eq. (3.8) simultaneously with considering l_0 to be

$$d_0 < l_0 < \lambda_{gd_1}(f'_{q_0}) \tag{3.10}$$

where the wavelength $\lambda_{gd_1}(f'_{q_0})$ is larger than $10d_0$ in the experiment. Thereafter, for the other nine wavelengths with q from q_0+1 to q_0+9, their corresponding $l_0(f'_q)$ can be solved from Eq. (3.8) one by one.

When plotting the ten $l_0(f'_q)$ versus their corresponding $\lambda_{gd_1}(f'_q)$ in the same figure, the relationship between $l_0(f'_q)$ and $\lambda_{gd_1}(f'_q)$ can be determined by curve-fitting using Least Square method (LSM).

3.3.2.2. Determining the Discontinuity Parameter l_d

For the pipe under PWT conditions, the fictitious length l_d introduced by the discontinuity is calibrated in this section before the quantitative evaluation.

Using the resonance equation Eq. (3.6), Eq. (3.2) can be expressed as

$$2l_2 + 2l_d(f_q) = [q - (m+x)]\lambda_{gd_2}(f_q) \tag{3.11}$$

where $(m+x)$ can be written as

$$m + x = [2l_1 - l_0(f_q)] / \lambda_{gd_1}(f_q) \tag{3.12}$$

After l_0 and q having been determined, $(m+x)$ can be solved from Eq. (3.12), and then the undetermined parameters in Eq. (3.11) are $l_d(f_q)$ and $\lambda_{gd_2}(f_q)$. Therefore, in order to solve $\lambda_{gd_2}(f_q)$ from Eq. (3.11), $l_d(f_q)$ should be calibrated. $l_d(f_q)$ is generated by the discontinuity at the PWT interface, therefore, it should be a function of the applied frequencies and the two inner diameters of the pipe at both sides of the interface. Since the wavelength is just right the combining function of the frequency and the diameter, l_d can be assumed as a function of the wavelengths

$$l_d = a_2(\lambda_{gd_1} - \lambda_{gd_2})/2 \tag{3.13}$$

where a_2 is an undetermined constant. Eq. (3.13) satisfies the limit condition that for the pipe without PWT, i.e. $\lambda_{gd_2} = \lambda_{gd_1}$, l_d equals zero.

Therefore, Eq. (3.11) can be written as

$$2l_2 + a_2(\lambda_{gd_1} - \lambda_{gd_2}) = [q - (m+x)]\lambda_{gd_2} \tag{3.14}$$

In Eq. (3.14), the unknown parameters are only a_2 and λ_{gd_2}. When using one joint whose PWT value is known (i.e., d_2 is known) for calibration, its corresponding λ_{gd_2} can be calculated from Eq. (3.9), and then the a_2 can be calibrated from Eq. (3.14). In this paper, joint No. 6 with PWT value of 0.585 mm is used for calibration.

3.3.2.3. Equation Solving

The final difference of the propagation route in the pipe without PWT has been expressed in Eq. (3.12) and $(m+x)$ can be solved from this equation. Then from Eq. (3.14), the wavelength in the wall thinning part of the pipe can be achieved as

$$\lambda_{gd_2} = (2l_2 + a_2\lambda_{gd_1}) / [q - (m+x) + a_2] \tag{3.15}$$

Finally, substituting Eq. (3.15) into Eq. (3.9), the diameter of wall thinning part is evaluated to be

$$d_2 = 2.4048 \Big/ \left[\pi \sqrt{\mu_0 \varepsilon_0 f_q^2 - \left(1/\lambda_{gd_2}\right)^2} \right] \tag{3.16}$$

3.4. Results Analysis and Discussion

During the calibration of l_0, the microwave signals at the frequency range from 14.00 to 14.20 GHz which contains ten NRFs was measured, and all these ten NRFs were used for curve-fitting. In the evaluation of PWT degrees, the same frequency range was measured and analyzed. It is found that for all the resonance frequencies, the proposed method gives almost the same evaluation result. For conciseness, only the experimental results at the frequency range from 14.12 to 14.16 GHz are presented here.

Fig. 3.3 shows the measured amplitudes of the microwave signal versus the sweeping frequencies, in the case that the pipe is connected with the joints from No. 1 to No. 6. It can be found that the resonance frequencies corresponding to the peaks of waveforms are changed due to the wall thinning. With the increase of the wall thinning degrees, the resonance frequencies decrease step by step. It is in accordance with the fact that the wavelength of guiding wave is correlative with the inner diameter of the waveguide. From the waveforms at frequencies 14.12 ~ 14.14 GHz and 14.14 ~ 14.16 GHz shown in Fig. 3.3, it is found that for the PWT joints No. 1 and No. 2, with the increase of 35

μm wall thinning, the resonance frequencies decrease from 14.1365 to 14.1357 GHz (0.8 MHz frequency change) and from 14.1590 to 14.1585 GHz (0.5 MHz frequency change) are found, respectively. Take advantage of the minimum frequency resolution 1 Hz of the microwave instrument, the proposed method has a quite high resolving power for detecting the PWT values.

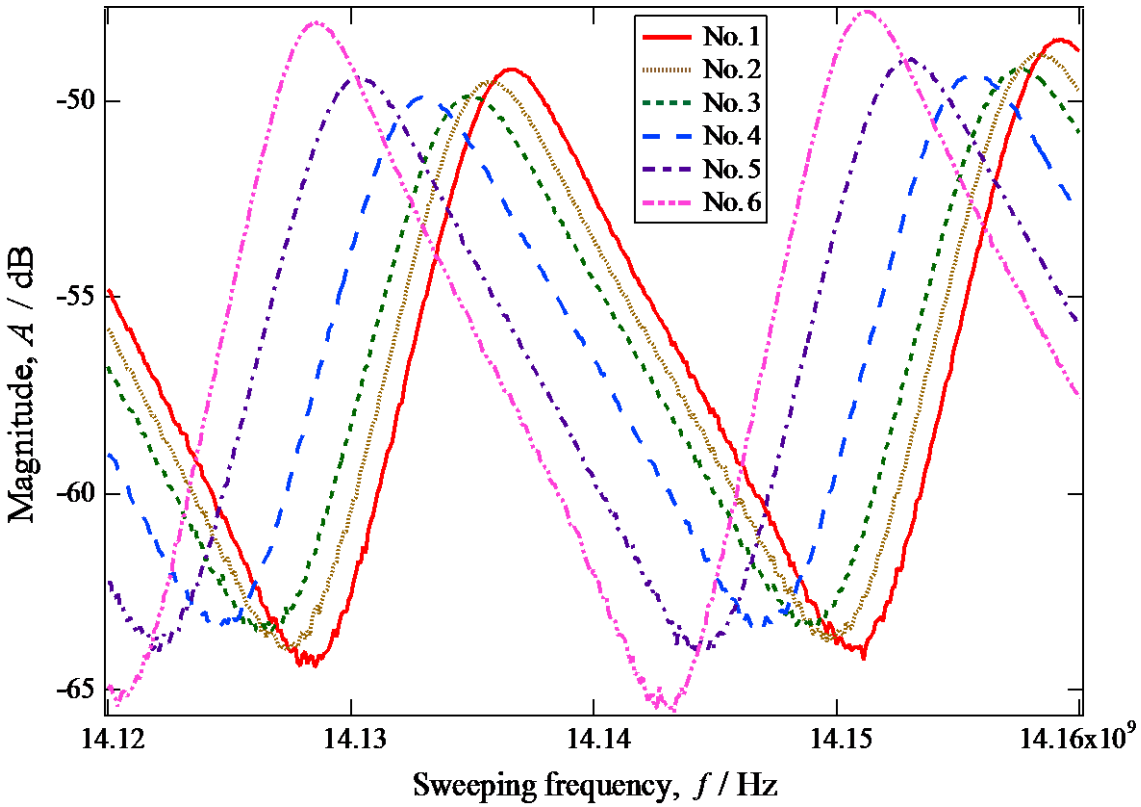

Fig. 3.3. Experimental results of the amplitudes vs. sweeping frequencies of microwaves when the pipe is connected with different PWT joints.

Using the method described in Sect. 3.3.2.1, $q_0 = 51$ and the ten different values of l_0 corresponding to the ten NRFs are solved. The ten calculated l_0 versus the corresponding wavelengths are shown together in Fig. 3.4 in form of triangle markers. In Fig. 3.4, using LSM, both the linear and quadratic polynomial curve-fitting results

are displayed. It is found that both kinds of curve-fitting methods match the triangle markers well and give almost the same fitting results. For convenience, the linear curve-fitting is adopted and l_0 can be expressed as follows

$$l_0 = G(\lambda_{gd_1}) = a_1\lambda_{gd_1} + b_1 \tag{17}$$

where a_1, b_1 are solved to be $a_1 = 0.76867494$ and $b_1 = -0.01873670$.

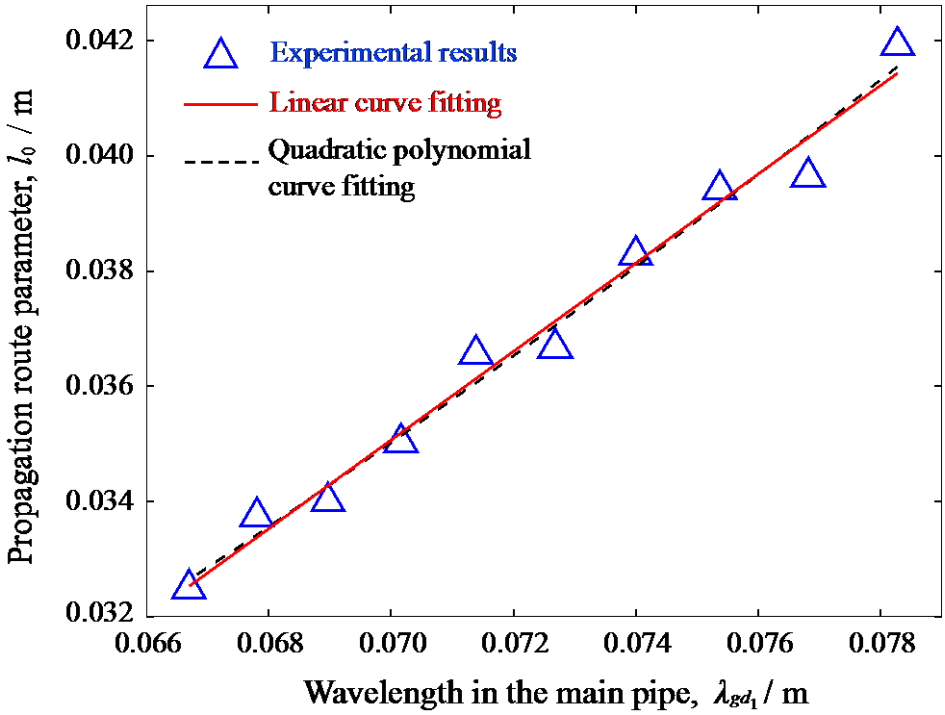

Fig. 3.4. Determining the path length l_0 using NRFs of experimental results.

If l_0 in Eq. (3.8) can be expressed exactly as a linear function of λ_{gd_1} as shown in Eq. (3.17), three NRFs are enough to solve the three unknown parameters a_1, b_1, and q. However, this linear relationship is rarely satisfied rigorously, mainly because the pipe and joint with an open end is not exactly under the open circuit condition. Therefore, it is suggested that more than 5 NRFs should be used to improve the calibration precision and the robustness of this method.

As described in Section 3.3.2.2, to solve the a_2 in Eq. (3.14), the joint No. 6 (with known PWT value of 0.585 mm) is used for calibration. It is solved that $a_2 = 0.218$.

For the resonance frequencies extracted from the peaks of the experimental results around higher frequency range14.14 ~ 14.16 GHz shown in Fig. 3.3, q equals $q_0 + 7$.

Using Eqs. (3.12), (3.15) and (3.16), for the higher frequency resonance results shown in Fig. 3.3, the evaluated PWT degrees (shown in inner diameters) in comparison with the nominal ones are shown together in Fig. 3.5.

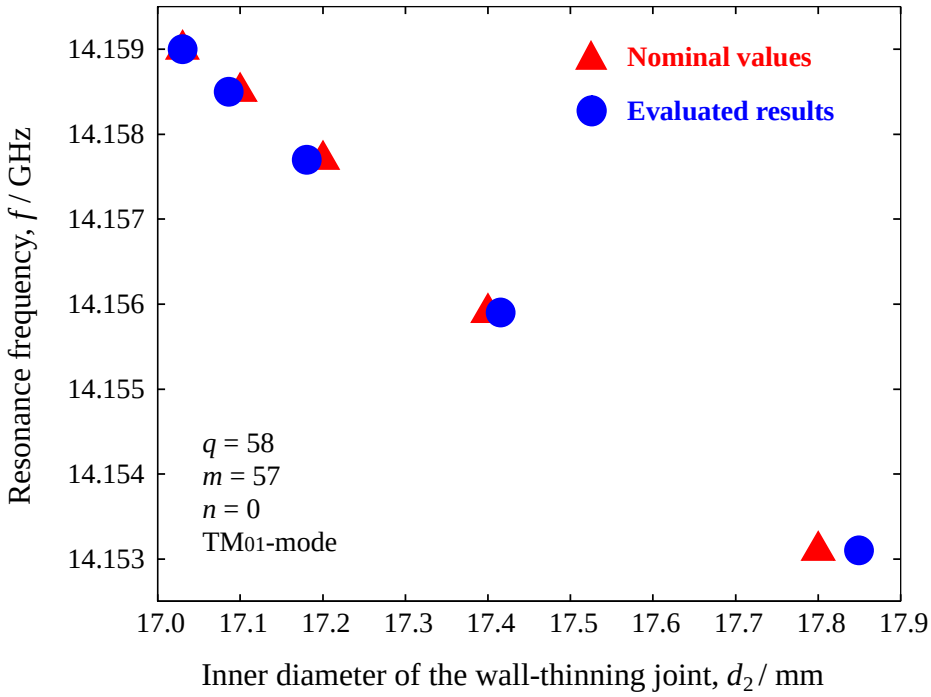

Fig. 3.5. Comparison of the evaluated inner diameters of joints and the nominal ones.

The triangle markers in Fig. 3.5 show the relationship of the joints' nominal inner diameters and the resonance frequencies extracted from the higher frequency results shown in Fig. 3.3. It can be found that with the increase of the inner diameter (i.e., with the aggravation of the PWT degree), the resonance frequencies decrease step by step.

The circle markers in Fig. 3.5 represent the inner diameters of the joints evaluated

from the measured resonance frequencies mentioned above.

By comparing the evaluated results with the nominal ones shown in Fig. 3.5, it is found that for the pipe having a 17.03 mm inner diameter, the maximum error of evaluated inner diameter is less than 0.294% (i.e., 0.05 mm). Since the dominant mode frequencies were used in the experiment, a high ratio of signal to noise was obtained and, thereby, a high precision measurement was realized.

It is noted that this paper only deals with an ideal experimental condition with an abrupt and full-circumference diameter change. Since the smallest PWT degree in the paper is as small as 70 μm changing in diameter, it also can be considered as a smooth PWT approximately. Therefore, this method could also be used for the pipe having a smooth PWT interface or having a PWT confined to only a part of the circumference. Because the proposed method is established by analyzing the change of the wavelength of microwave in the pipe, for the two conditions mentioned above, the wall thinning evaluation can be converted into the analysis of the changed wavelength. Thus, if the degree of the wall thinning is large enough, the high precision evaluation can still be realized independent of the shape of wall thinning. In addition, the paper deals with an ideal pipe. If the pipe has welds or fittings changing the inner diameter of the pipe, an additional reflection will occur which will affect the evaluation result of the proposed method.

3.5. Conclusions

In this paper, microwaves are creatively adopted to detect and evaluate the PWT degrees remotely and quantitatively with high efficiency.

From the measured amplitudes of the microwave signal versus the sweeping frequencies,

it can be found clearly that for the same length pipe with different wall thinning values, the resonance frequencies are different. The relationship is that with the increase of the PWT degrees, the resonance frequencies decrease step by step. It is in accordance with the fact that the wavelength of guiding wave is correlative with the inner diameter of the circular waveguide.

Then by tracing and reconstructing the propagation route, the equations describing the route of propagation and then the resonance equation are derived.

Finally, by analyzing, decomposing and solving the resonance equations, a group of resonance results of the pipe having a 17.03 mm inner diameter and connected respectively with six PWT joints having different PWT degrees is analyzed and whose resonance frequencies are used for evaluating the PWT degrees of these joints. From comparison of the evaluation results of the inner diameters of these joints and the nominal ones, it is found that the maximum evaluation error is less than 0.294%. It hints that a high efficiency nondestructive remote detection method with high evaluation precision has been achieved.

It should be noted that, although the PWT joints having the same length were measured at the terminal of the pipe in this paper, the proposed method is possible to be used independent of the pipe length and, the position and the length of the PWT. In addition, since the measurement was carried out under the open-end condition, the proposed method will have a great potential for the practical applications.

References

[1] R. B. Dooley and V. K. Chexal, Int. J. Pres. Ves. Pip., **77**, 85 (2000).

[2] A. Vageswar, K. Balasubramaniam, C. V. Krishnamurthy, T. Jayakumar, and B. Raj, NDT & E Int., **42**, 275 (2009).

[3] G. Kajiwara, J. Test. Eval., **33**, 295 (2005).

[4] T. Shimakawa, H. Takahashi, H. Doi, K. Watashi, and Y. Asada, Nuclear. Eng. Des., **139**, 283 (1993).

[5] K. R. Leonard and M. K. Hinders, Ultrasonics, **43**, 574 (2005).

[6] H. Nishino, M. Takemoto, and N. Chubachi, Appl. Phys. Lett., **85**, 1077 (2004).

[7] J. Ding, Y. Kang, and X. Wu, NDT & E Int., **39**, 53 (2006).

[8] J. B. Nestleroth and R. J. Davis, NDT & E Int., **40**, 77 (2007).

[9] Y. Li, L. Sun, Z. Song, and Y. Zhang, Ultrasonics, **44**(S1), e1111 (2006).

[10] C. Aristégui, M. J. S. Lowe, and P. Cawley, Ultrasonics, **39**, 367 (2001).

[11] Y. Ju, L. Liu, and M. Ishikawa, Mater. Sci. Forum, **614**, 111 (2009).

[12] K. Abbasia, S. Ito, and H. Hashizume, Int. J. Appl. Electromagn. Mech., **28**, 429 (2008).

[13] K. Abbasi, N. H. Motlagh, M. R. Neamatollahi, and H. Hashizume, Int. J. Pres. Ves. Pip., **86**, 764 (2009).

[14] D. M. Pozar, Microwave Engineering (2nd Ed), New York: John Wiley & Sons, (1998).

Chapter 4. Time Domain Measurement (TDM) for PWT Location Evaluation

Abstract

This research aims to find an efficient and nondestructive way of detecting the locations of the pipe wall thinning (PWT) in a long-distance metal pipe at open-end condition. Time domain measurement (TDM) of microwave signals is adopted in the method since microwaves can propagate a long distance with low attenuation in the pipe and reflection occurs at the PWT section. To carry out the measurement, a microwave vector network analyzer (VNA) and a self-designed coaxial-line sensor were used to generate microwave signals propagating in the pipe. By analyzing the time domain response of the signals and extracting the time of flight (TOF) that corresponds to the PWT location, the locations are quantitatively evaluated after the group velocity of the microwave signals propagating in the pipe was calibrated. In order to approach a pipe with different PWT degrees and locations, three brass pipes with an inner diameter of 17.0 mm and lengths of 453 mm, 455 mm, and 2000 mm, respectively, were used in the experiment. In addition, five joints, which have the length of 17.0 mm and inner diameters from 17.10 mm to 18.20 mm were also used. The arithmetical mean error of the evaluation for PWT locations is found to be less than 1.7 mm, i.e. less than 0.068% of the length of the corresponding pipe. It indicates that a quite efficient and precise method to remotely and quantitatively evaluate PWT locations in a long-distance pipe has been established.

Keywords: microwave, metal pipe, pipe wall thinning (PWT), remote detection, time of flight (TOF), nondestructive testing and evaluation (NDT&E)

4.1. Introduction

Metal pipes are used widely in many industries, including oil and gas transportation, chemical industry and various kinds of power plants. Pipe wall thinning (PWT) is one of the most serious defects in the pipelines during their service in those industries [1-4]. In recent years, accidents caused by PWT have been reported frequently around the world, which have caused severe economical loss and social damages. Therefore, efficient and nondestructive detection of PWT defects as well as their quantitative evaluation, especially for long-distance pipes are mandatory for the effective maintenance and the lifetime prediction of the pipelines in order to avoid severe economical and social damages.

The PWT problem is twofold. One is the PWT degree, which means the depth and length of PWT. This is important information concerning the safety and lifetime of pipes. The other is the PWT location, which is important for the detection and maintenance of in-service pipes, especially long-distance pipes. Recently, many researchers have focused on developing nondestructive testing (NDT) techniques for detecting PWT defects, including infrared thermography [3], X-ray [5], electrical potential drop [6], ultrasonic [7,8], magnetic flux leakage [9], eddy current method [10], elastic-plastic finite element analysis [11] and so on. However, they can only inspect a pipe locally except for the hollow cylindrical guided wave (HCGW) of ultrasonic method [8]. For the HCGW method, the ultrasonic energy will attenuate much faster when there are many girth welds on the surface of the pipe [12], and the HCGW can only propagate a long distance along an isolated pipe. Moreover, all of these methods are difficult to measure long pipes buried underground, or placed in the walls of some concrete buildings, or

under other similar conditions. This is the main shortage for the HCGW method, because the ultrasonic energy will attenuate much faster in the pipe surrounded by various kinds of media such as earth, concrete, etc. [13]. In reality, all those methods generally take lots of time and labor to inspect a long-distance pipe, and most of them can only measure the PWT degrees locally, i.e., they can only solve part of the first aspect of the PWT problem.

Since microwave can propagate a long distance with quite little attenuation in a low-loss dielectric medium such as air, gas, and gasoline, it can be used to overcome the shortcomings of the aforementioned methods. To microwave NDT, a metal pipe under test (PUT) can be promisingly taken as a circular waveguide [4,14], and all the energy of microwave signals is confined inside the pipe. Therefore the propagation and attenuation of microwave in the pipe are independent of the surrounding conditions of the pipe.

In our previous studies [4], the PWT degrees of a 2 m long pipe were remotely examined and quantitatively evaluated with a high precision using microwave signals generated by a vector network analyzer (VNA) working at frequency domain. Meanwhile, the time domain response of microwave signals, which can be effectively used for detecting fault location, identifying impedance variations in connectors, transmission lines or waveguides, can be derived from inverse fast Fourier Transform (IFFT) of signals obtained at frequency domain. Because a defect in the pipe affects the impedance of the pipe and causes a reflection peak in time domain signals, the time domain measurement of microwave signals was adopted and then the time of flight (TOF) extracted from the time domain signals was used to detect the locations of defects in a metal pipe.

Some studies have adopted time of flight of microwave signals to detect locations of

deep cracks (that having depths no less than 2 mm) in a metal pipe [15,16], and their research showed a potential use of microwave for detecting defects of pipelines. However, there are three main shortcomings in their proposed method. First, their measurement instrument is a little too complicated that a mode converter and a mounted tapered waveguide are compulsorily required for detection. Second, for signal processing, the measured reflection coefficient of signals in a crackless pipe with exactly the same inner diameter and length as the PUT is additionally required as the reference signals. Third, for any single crack, the evaluated location was not unique (multiple candidate locations were evaluated for a single crack), and the errors of evaluation are as large as 12.3 mm (for a crack located at 800 mm in a 1200 mm long pipe) even for the best groups of evaluated results [16]. Further, since the signal of experimental results has multi-peaks, a cut-off parameter β is needed when carrying out signal processing while a general criterion to determine β has not been established yet [15,16]. These shortcomings hinder the practical approach and hamper the broad application of microwave for locating defects in the pipes. Moreover, the evaluation of PWT, i.e. a shallow defect with the change of the inner diameter of a pipe, is still not carried out. In addition, there is no literature reporting the inspection of metal pipes by microwaves at the open-end condition which is the most common case in the practice, except the Ref. [4].

The method shown in is chapter significantly simplifies the sensor structure and demonstrates the position measurement of wall thinning in open-end pipes at the first time utilizing time domain microwave signals. The simplification of sensor structure is fortunately realized based on studies of Piotrowski [17], Gimenno and Guglielmi [18], and Adous *et al* [19]. Their studies have shown that when a coaxial line is connected directly to a circular waveguide under the rotational symmetry condition, only TM_{0m} modes are

excited in the circular waveguide. In this research, we designed a rotationally symmetric coaxial line sensor, and utilized the TOF of microwave to detect the location of PWT defect. The reason for using TOF to detect PWT location is that a PWT defect acts as discontinuity of the impedance of the waveguide, which causes large reflection at the time domain measurement result.

Using a simple measurement instrument that consists of a VNA and the self-designed coaxial-line sensor, reflected signals in the pipe at frequency domain were measured, and time domain signals were derived through their IFFT. Finally, by calibrating the group velocity and analyzing the time domain signals and extracting information of TOFs corresponding to the PWT locations, we have demonstrated a nondestructive method that can deliver an efficient inspection and quantitative evaluation of PWT locations for a long-distance metal pipe.

It should be noted that this paper mainly aims to establish an efficient and stable method to determine the PWT location in a long-distance pipe regardless of the start point and end point of a PWT defect since lengths of PWT defects are normally no longer than the inner diameter of the pipe. After the location is determined, more detailed information such as the start point and end point, as well as the shape of a PWT defect can be evaluated by a further development of the proposed method or by other local detection methods with further advance in accuracy.

4.2. Experimental Approach

The experimental instrument is composed of a VNA and a coaxial-line sensor developed by ourselves, as shown in Fig. 4.1(a). The coaxial-line sensor is made from a standard coaxial-line cable and a connector, and it serves as both the transmitting and receiving

port of microwave signals. The length of this coaxial-line sensor is $l_a = 52.0$ mm. In order to inspire strong signals in the pipe that is considered as a circular waveguide, the sensor is designed with inner cable to be $d_0 = 6.5$ mm protrudent as shown in Fig. 4.1(b).

The pipe specimens tested in the experiment, including three pipes with inner diameter of $d_1 = 17.0$ mm, five joints and two connectors, are made of brass. The lengths of the three pipes numbered as P1, P2, and P3 in the experiment are $l_{11} = 453$ mm, $l_{12} = 455$ mm, and $l_{13} =$ 2000 mm, respectively, and the wall thickness of the pipes is $t = 1.0$ mm. The five joints with the same length of $l_2 = 17.0$ mm and different nominal inner diameters are utilized together with the two connectors to construct different wall thinning sections in a combined pipe, and they are numbered as joint No. 1 to No. 5 successively and shown in TABLE 4.1. Different PWT degrees and locations can be constructed using these pipes, joints, and connectors.

In the experiment, three kinds of pipes with PWT defects of different locations and degrees were constructed by the aforementioned pipes, joints and connectors. The first kind of PUT consists of P1, P3, and a joint located between them, as shown in Fig. 4.2(a). The difference between the second and the first kind of PUT is the exchange of the locations of pipes P1 and P3, and the schematic diagram for the second kind of PUT is shown in Fig. 4.2(b). To test the first and second kind of PUT, the five joints listed in TABLE 4.1 were connected between P1 and P3 in turn, to construct PWT sections with different PWT degrees. The third kind of PUT is composed of P1, P2, P3, and two joints between them as the photograph shown in Fig. 4.1(a) and the schematic diagram in Fig. 4.2(c), which is utilized to approach a pipe with two separate PWT sections. To approach the third kind of PUT, the four joints numbered as No. 1 to 4 in TABLE 4.1 are used in the experiment, where one joint (No. 2 to 4, respectively) is used in turn to

construct the first PWT section, and the other three joints are used in turn to approach the second PWT section for each joints being used as the first PWT section.

In Fig. 4.2, l_0 is the total length of the PUT, d_1 is the inner diameter of pipe section without PWT, while t is the wall thickness of the pipe. t_1 and t_2 represent the PWT degrees. l_{21} and l_{22} are the corresponding lengths of the two defects, and they are both equal to l_2 in the experiment.

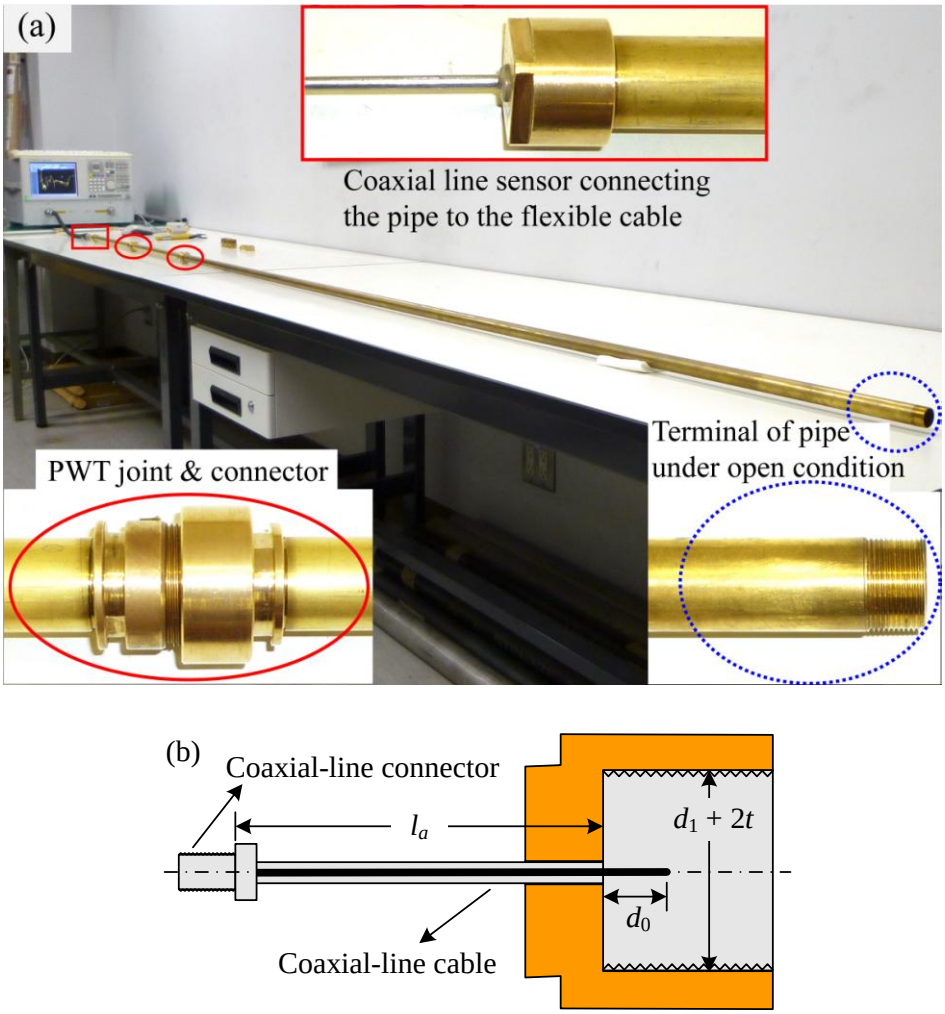

Fig. 4.1. (a) Overall photograph of experimental instrument (the three insets are the enlarged images of corresponding parts of the pipe, and the correspondence is carried out using markers of real line panes, ellipses, and dashed line ellipses); (b) detailed structure of the self-designed coaxial line sensor.

TABLE 4.1. Detailed geometric parameters of the joints.

Joint's number	1	2	3	4	5
Inner diameter, d_2 (mm)	17.10	17.20	17.40	17.80	18.20
PWT degree, %t	5%t	10%t	20%t	40%t	60%t

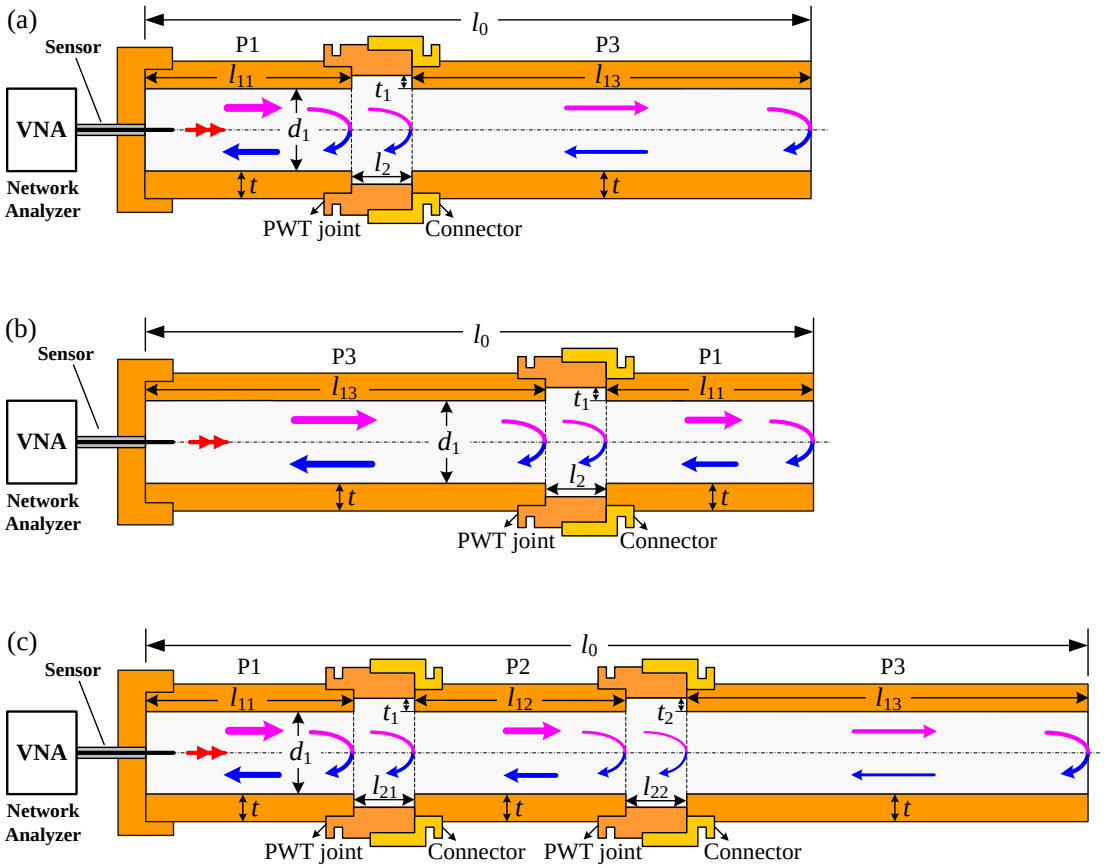

Fig. 4.2. Schematic diagrams of experimental setup for two groups of combined pipes having (a) single PWT defect near the sensor, (b) single PWT defect far from the sensor, and (c) two PWT defects.

During the experiment, microwave signals were generated by the VNA and coupled into the pipe through the coaxial-line sensor. The VNA was set to work at the S11 mode,

so that microwave signals reflected from both the PWT sections and the terminal of the PUT were detected by the same port of the sensor. When sweeping the frequency within a proper range, the corresponding amplitudes containing PWT information were measured, and the frequency domain signals were obtained directly, from which the time domain results can be calculated through IFFT. TOF, which is defined as the arrival time of any reflection peak of signals going and returning to the reference zero time interface in this paper, can then be extracted from the time domain analysis of microwave signals.

Moreover, to obtain high precision in the time domain measurement, sweeping points of 1601 are set in the experiment, and the time domain results are designed to be measured in two steps: the first step is to measure the pipe at a very wide range of time domain that is wide enough to contain time domain information from the calibrated zero time interface to the reflection from the terminal of the PUT to get general information of the PWT in the pipe, and the second step is to measure the pipe at a focused range (much narrower range) of time domain where big reflection occurs to obtain more detailed information about the PWT. The two steps are carried out with the same number of sweeping points. Thus, the time precision of the second step is much higher because of the smaller time range is measured. Although it is technically possible to use the maximum 6401 sweeping points, it is found that the result has no obvious difference in the results measured at a focused time range.

4.3. Theoretical analysis

4.3.1. Confirming the Range of Sweeping Frequency

As shown in Fig. 4.1, the coaxial line sensor is used as both the transmitting and receiving port of microwave signals, and its rotationally symmetric structure when connected to the circular waveguide results to that only TM_{0m} modes are generated [17-19], among which the dominant mode is TM_{01} [14]. It should be mentioned that, however, the coaxial line sensor used in the experiment is not exactly a coaxial line, but is designed with the inner cable to be $d_0 = 6.5$ mm protruding as shown in Fig. 4.1(b) so as to inspire strong signals in the pipe. This protrudent structure causes that a comparatively small amount of TM_{nm} modes ($n \neq 0$) other than TM_{0m} modes are also excited in the circular waveguide.

To insure single working mode of microwave signals in the PUT, the sweeping frequency is set to be lower than the cutoff frequency of the first high order mode, i.e. TM_{11} mode. Moreover, because time domain response of the signals is obtained through IFFT of the frequency domain result, the frequency range of signals cannot be too narrow in order to achieve a high resolution in time domain. Therefore, the frequency range between the cutoff frequencies of TM_{01} mode and TM_{11} mode is utilized in the experiment.

The cutoff frequency of TM_{01} and TM_{11} mode are expressed as follows [14],

$$f_{c\mathrm{TM}_{n_0 1}} = c p_{n_0 1} / (\pi d), \quad (n_0 = 0, 1) \tag{4.1}$$

where d is the inner diameter of the pipe, c is the speed of light in free space, and $n_0 = 0$ and 1 correspond to TM_{01} and TM_{11} mode, respectively. $p_{n_0 1}$ represent the first and the second roots of the first kind Bessel function $J_{n_0}(x)$, i.e. $J_{n_0}(p_{n_0 1}) = 0$, with $p_{01} = 2.4048$ and $p_{11} = 3.8317$.

4.3.2. Signal Analysis and TOF from Discontinuity of the Pipe

The VNA is utilized to generate microwave signals and then measure the frequency domain signals propagating along the pipe. Timed domain response can be mathematically calculated through IFFT of the results of frequency domain response to convert the frequency domain information into the time domain.

For the dominant TM mode, TM_{01} mode, of the circular waveguide, the cutoff wavenumber is $k_c = 2p_{01}/d$. Meanwhile, the wave impedance of a hollow pipe can be derived from Ref. [14], and the expression shows that the wave impedance is a function of the inner diameter of the pipe. Therefore, change in the diameter of the circular waveguide will cause discontinuity in the wave impedance, and thus the reflection from the location of this discontinuity will occur. This is shown in the schematic diagrams in Fig. 4.2. The TOFs of the signals reflected from different discontinuities can then be taken as the indications for evaluating the PWT locations.

4.3.3. Group Velocity Calibration and PWT Location Evaluation

The group velocity is a function of the working mode and operating frequencies of microwave in the circular waveguide filled with air and can be expressed as follows [14],

$$v_g = c \cdot \sqrt{1-(f_c/f)^2} \propto (1/\lambda_g) \tag{4.2}$$

where λ_g is the wavelength in the waveguide and the cutoff frequency is $f_{c\mathrm{TM}_{01}} = cp_{01}/(\pi d)$ for the dominant TM_{01}-mode, while f is the operating frequency.

The group velocity of microwave is prerequisite for evaluating PWT locations quantitatively. As mentioned above, to achieve a high resolution in time domain, the operating frequency range of the microwave signals can not be too narrow. Therefore, the group velocity of the wave package which consists of multiple frequencies is

difficult to be decided from Eq. (4.2) by a single frequency. In this paper, the group velocity is confirmed using a calibration method.

The calibration of group velocity v_g can be realized by measuring a reference pipe with a known length and exactly the same inner diameter d_1 as the defect-free section of the PUT. When carrying out this calibration, the source signals should be set exactly the same (at the same sweeping frequency range and after the same E-cal) as the ones utilized in the PWT evaluations. The terminal condition of the reference pipe is set to be short circuit by covering the open end of the pipe with a metal cap that can be taken as a perfect conductor. After measuring the TOF corresponding to twice the full length of the reference pipe, the group velocity can be calculated as

$$v_g = 2l_{\text{cal}} / T_{\text{end}} \tag{4.3}$$

where l_{cal} is the length of the reference pipe, and T_{end} is the difference of TOFs corresponding to the signals reflected from the beginning and the end of the pipe. For the pipe at the short circuit condition, a strong reflection will occur at the end of the pipe and cause a large reflection peak in the time domain result, which makes it easy to determine T_{end} with a considerably small error.

Taking the group velocity and the TOF corresponding to the PWT section of the PUT into account, the PWT location can be evaluated by

$$l_{\text{PWT}} = v_g \cdot T_{\text{PWT}} / 2 \tag{4.4}$$

where l_{PWT} and T_{PWT} represent the PWT location and TOF corresponding to the PWT, respectively. The presence of factor 1/2 in Eq. (4.4) is due to the fact that the signals should propagate twice the distance between the sensor and the PWT section after being transmitted and received by the sensor.

4.4. Result Analysis and Discussion

4.4.1. Analysis of Time Domain Signals and Group Velocity

For the PUT with inner diameter of 17.0 mm, the cutoff frequencies of TM_{01} and TM_{11} modes are calculated to be 13.499 GHz and 21.509 GHz from Eq. (4.1). To insure the single TM_{01} mode, the sweeping frequency is set to be from 13.0 GHz to 21.0 GHz.

When using pipe P1 to calibrate the group velocity, the experimental results of time domain signals are shown in Fig. 4.3. It is obtained through IFFT of the frequency domain result. In Fig. 4.3, quite clear information of the reflections is observed. As mentioned in the experimental approach section, focused measurement of small time range is implemented to improve the precision at time domain, and the obtained results are inserted in Fig. 4.3. Because the zero time reference plane is set at the end of the flexible cable of the VNA rather than at the beginning of the pipe, the reflection peaks corresponding to all of the connections as well as the reflection from the pipe end are presented together in Fig. 4.3.

The largest peak at the left side of Fig. 4.3 is caused by the mismatch between the coaxial-line sensor and the pipe, as the inserted enlarged image of the sensor shown in Fig. 4.1(a). From the focused result within time range of 0 ~ 1.0 ns shown in Fig. 4.3, the TOF corresponding to this mismatch is found to be 0.724 ns, which is the TOF at the beginning of the pipe. While the last large peak at the right side of Fig. 4.3 corresponds to the reflection from the end of the reference pipe P1, and the TOF is measured to be 5.320 ns from the focused result within the time range of 5.0 ~ 6.0 ns.

Therefore, the difference of TOFs corresponding to the signals reflected from the beginning and the end of the pipe is calculated to be $T_{\text{end}} = 4.596$ ns. Since the length of

pipe P1 is l_{cal} =453 mm, the group velocity is calculated to be v_g = 1.971×10^8 m/s from Eq. (4.3).

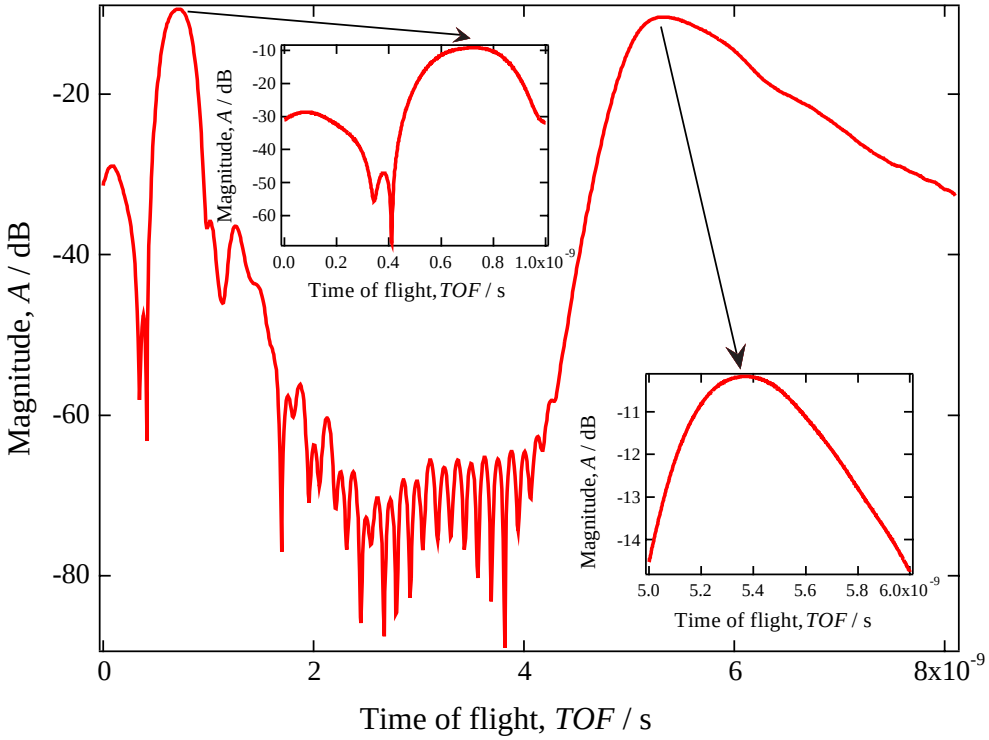

Fig. 4.3. Time domain experimental results of pipe P1 measured under short circuit condition. To show the results clearer, two figures are inserted: one is the focused figure at time range 0 ~ 1.0 ns for the reflections from the sensor, the other is focus on time range 5.0 ~ 6.0 ns for the reflections from the end of the pipe.

4.4.2. Evaluating the Location of a Single PWT Section

As mentioned above, three kinds of PUT are measured in the experiment. The measurement results of the first kind of PUT in the time domain are shown in Fig. 4.4. It is found that large reflection peak for each PUT with a different PWT degree occurs around 5.0 ns, which is the TOF from the PWT section. It is shown in both the wide time range result and the focused result within the time range of 5.0 ~ 6.0 ns in Fig. 4.4

that, although the magnitude of the peak corresponding to each PWT section increases with the PWT degree of this section ranging from 50 μm to 600 μm, the TOFs corresponding to these large peaks of reflection are almost the same for all the PWT sections with different PWT degrees. It confirms the ability to detect small PWT defect and the good stability of the proposed method. In addition, a large reflection peak also appears around 25.0 ns, which is caused by the reflection at the open end of the PUT.

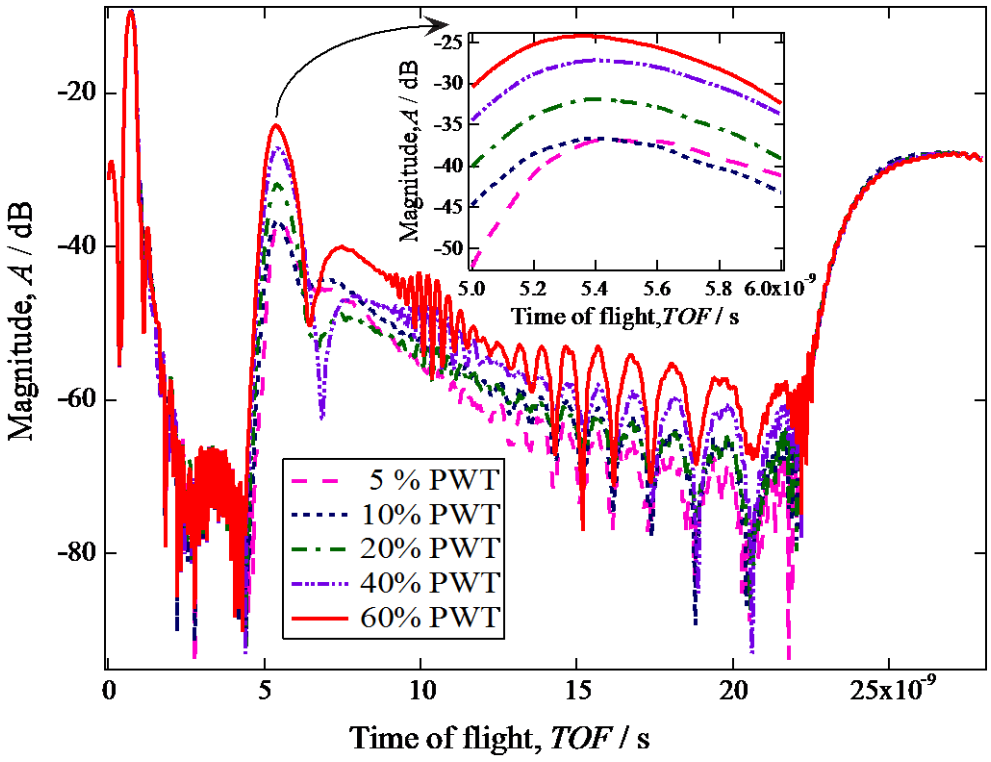

Fig. 4.4. Experimental results of the combined pipe shown in Fig. 4.2(a) when connecting with different degrees of PWT joints; the inset figure is the focused part at time range 5.0 ~ 6.0 ns around the TOF of reflection from PWT defects.

However, it should be noted that only one large reflection is observed although there are two discontinuities in the wave impedance, i.e. the discontinuities at the start and end points of a PWT section. This phenomenon is caused by the frequency range being

not wide enough, which makes the resolution of time domain measurement being low. When the two reflection peaks caused by the start and end points of the PWT section are not sharp enough, the signals will overlap and, as a result, only the peak of the overlapped signals is observed. Fortunately, the lengths of the industrial PWT defects are generally smaller than the inner diameter of the pipe and of course much smaller than the pipe length. Thus the most important task is the determination of the PWT location in the long-distance pipe rather than distinguishing the start point and end point of the PWT section. After the location is determined, more detailed information such as the start point and end point, and the shape of the PWT defect can be evaluated by an improvement of the proposed method or by other local detection but more accurate techniques. This paper mainly aims to establish an efficient and stable method to determine the PWT location in a long-distance pipe in spite of the detailed structure of the PWT section.

The measurement results of the second kind of PUT shown in Fig. 4.2(b) in the time domain are shown in Fig. 4.5. It is found that large reflection peak for each PUT occurs around 21.0 ns, which is the TOF from the PWT section. The inset in Fig. 4.5 shows the focused result within the time range of 20.0 ~ 22.0 ns.

It is similar as the first kind of PUT, the TOFs corresponding to the large reflection peaks are almost the same for the PWT sections with different PWT degrees, which confirms again the good stability of the proposed method.

Taking the calibrated group velocity in pipe P1, i.e. $v_g = 1.971 \times 10^8$ m/s, into account, the PWT locations of the first kind of PUT can be derived from the time domain signals shown in Fig. 4.4 by Eq. (4.4), and the evaluated results are shown in Fig. 4.6. In Fig. 4.6, the values at the abscissa of the two dashed lines correspond to the actual locations of the start point and end point of the PWT section, i.e. 453 mm and 470 mm, respectively.

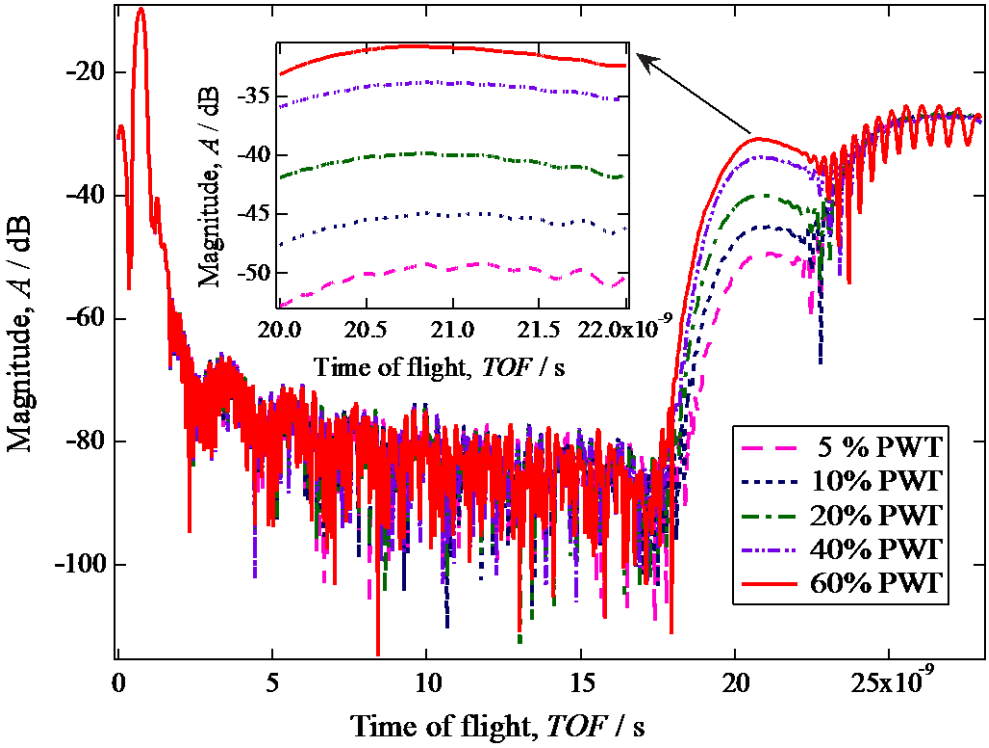

Fig. 4.5. Experimental results of the PUT shown in Fig. 4.2(b) when connecting with different degrees of PWT joints; the inset figure is the focused part at time range 20.0 ~ 22.0 ns around the TOF of reflection from PWT defects.

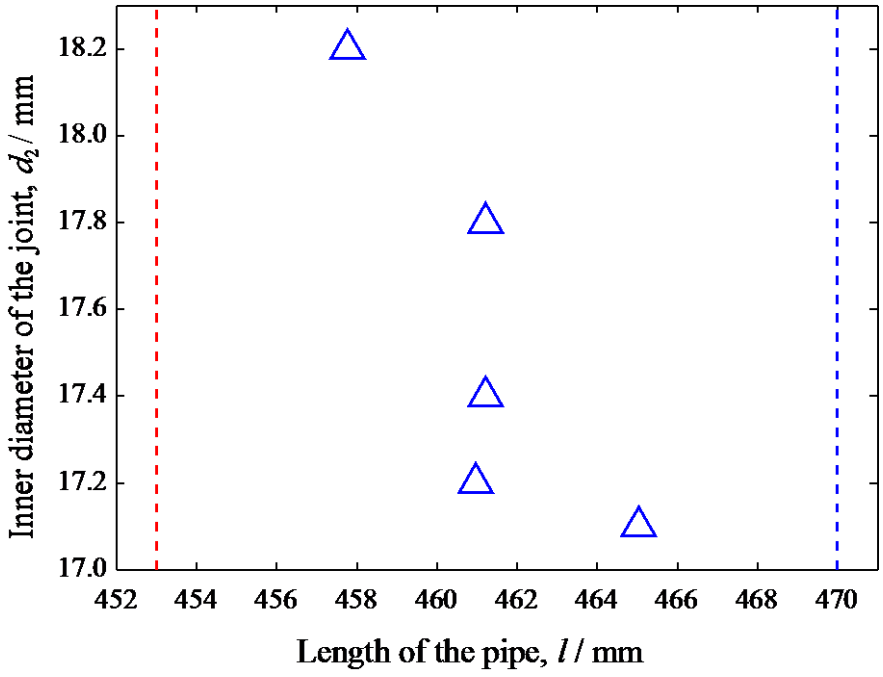

Fig. 4.6. Evaluated results for PWT defects located near the sensor (shown in Fig. 4.4).

From Fig. 4.6, it is found that all the PWT locations evaluated from the TOFs lie between the start and end points of the PWT section. Taking the middle location of the PWT section, i.e. 461.5 mm, as a datum plane, the arithmetical mean error of the evaluation is 1.7 mm, i.e. 0.068% of the length of the PUT, and even the maximum evaluation error is less than 3.8 mm, i.e. less than 0.16% of the length of the PUT. In addition, it is noted that when the PWT degree is very small such as 50 μm, i.e. 5% of the wall thickness of the pipe, the evaluated location is a little closer to the end point of the PWT section, which means the reflection from the end point is stronger and caused the peak of overlapped signals to lean to the end point; while as the PWT degree is comparatively large such as 0.6 mm, i.e. 60% of the wall thickness, the evaluated location is a little closer to the start point of the PWT section, which is caused by the reflection from the start point becoming stronger.

For the experimental results of the second group of PUT shown in Fig. 4.5, the group velocity calibration was carried out again using pipe P3 instead of P1 because the pipe P3 is connected to the sensor and located at the beginning of the composite PUT. The group velocity in P3 was obtained as $v_g' = 1.999 \times 10^8$ m/s, and then the PWT locations in the second kind of PUT were evaluated again and shown in Fig. 4.7.

As shown in Fig. 4.7, all the PWT locations evaluated are between the start point and end point of the PWT section. Taking the middle location of the PWT section, i.e. 2008.5 mm, as a datum plane, the arithmetical mean error of the evaluation is less than 1.4 mm, i.e. less than 0.055% of the length of the PUT, even for the PWT introduced by the 60% PWT joint, joint No. 5, which has the maximum evaluation error of 5.2 mm, i.e. less than 0.21% of the length of the PUT. It means that all the evaluated locations matches well with the actual values even for the worst one.

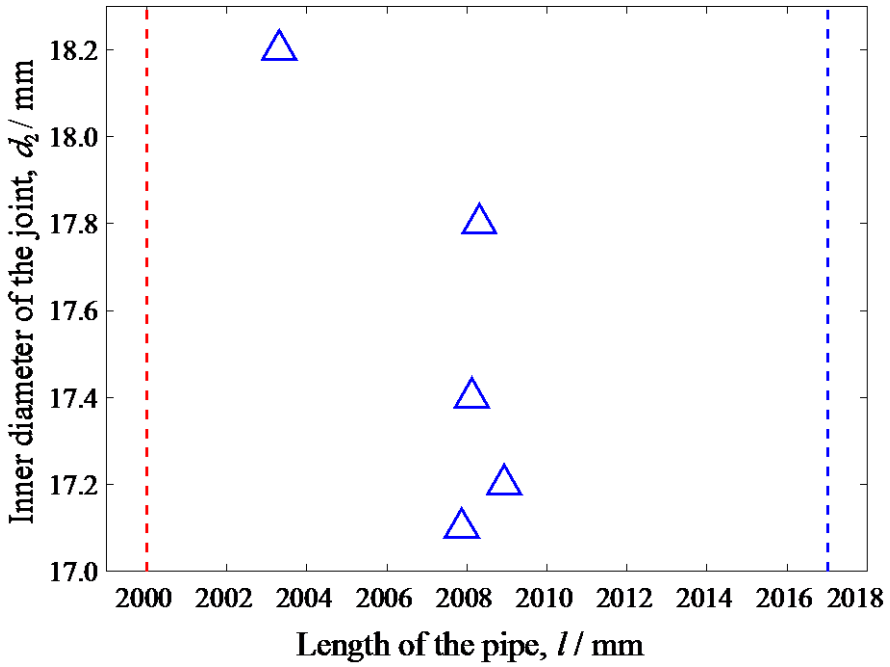

Fig. 4.7. Evaluated locations for results shown in Fig. 4.5 of PWT sections located far away from the sensor.

As a result of the calibration method, it should be noted that the evaluation results of the proposed method with high precision is sensitive to the calibrated group velocity. In other words, it is very important to calibrate the group velocity by a reference pipe with exactly the same inner diameter with the PUT connected to the sensor. In addition, Fig. 4.7 is a little different from Fig. 4.6 that the evaluated location is a little closer to the start point of the PWT section when the PWT degree is as large as 0.6 mm.

4.4.3. Evaluating the Locations of Two Separate PWT Sections

The third kind of PUT is composed of P1, P2, P3 and two joints between them as shown in Fig. 4.2(c), which is utilized to approach a pipe with two separate PWT sections.

As mentioned in the experimental approach section, the four joints numbered as No. 1 to 4 in TABLE 4.1 are used in the experiment, where one joint (No. 2 to 4, respectively) is used in turn to construct the first PWT section, and the other three joints are used in

turn to approach the second PWT section. The time domain results of the third kind of PUT with joint No. 4 as the first PWT section is shown in Fig. 4.8. In Fig. 4.8, two large peaks caused by reflections from the first and second PWT sections are clearly presented. Similar as the results of PUT with single PWT section, it can also be seen from these figures that the magnitude of the second peak increases with the PWT degree of the second PWT section. On the other hand, the locations of the first and second peaks are almost constant regardless of the different PWT degrees, and this confirms the stability of the proposed method for detecting two separate PWT sections.

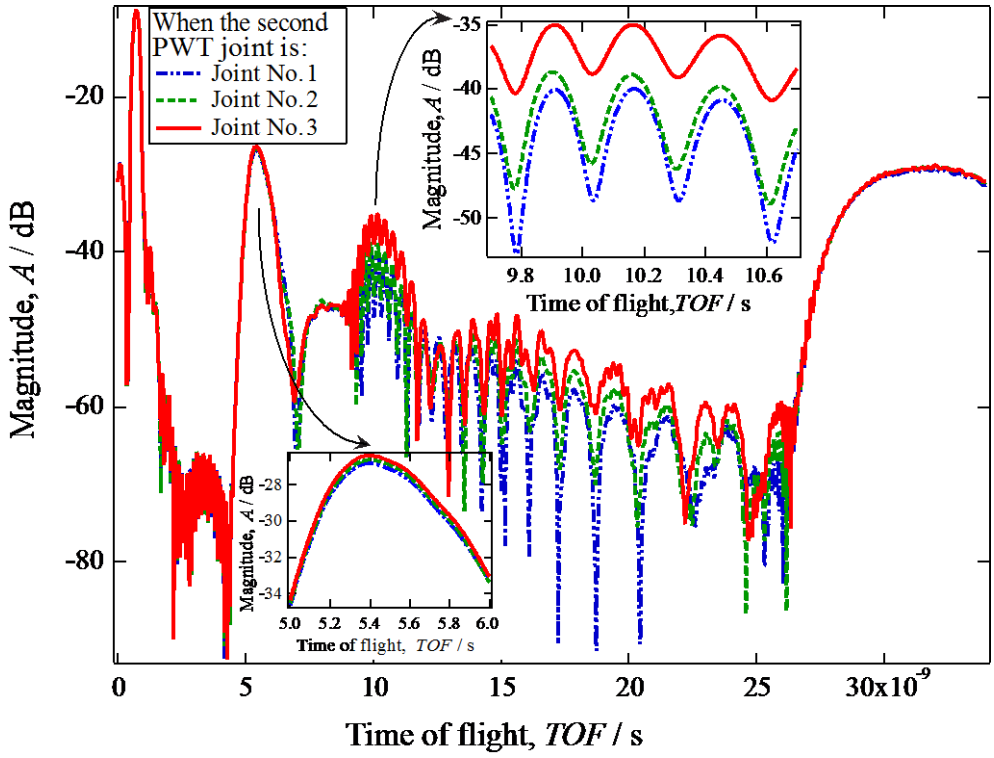

Fig. 4.8. Experimental results of the pipe composed of pipe P1 and the PWT joint No. 4 and pipe P2 and then PWT joints No. 1 ~ 3 and finally pipe P3 as shown in Fig. 4.3(c). The inset figures are the focused part at time range 5.0 ~ 6.0 ns around the TOF of reflection from the first PWT defect, and the focused part at time range 9.7 ~ 10.7 ns around the TOF of reflection from the second PWT defect.

For conditions that joints No. 2 and 3 were used as the first PWT section, the similar results were obtained, and the only difference is that the magnitudes of the first peaks for them are a little smaller than the results presented in Fig. 4.8 and, as a result, the reflection signals of the second PWT sections are stronger and the evaluation of them is more feasible. The reason for this phenomenon is that stronger reflection occurs at the first PWT section for the more severe PWT defect, such as joint No. 4, as the first PWT section and, as a result, the stronger reflection caused by the first PWT section more seriously masks the reflection results of the second PWT section.

Considering the group velocity calibrated in pipe P1, i.e. $v_g = 1.971 \times 10^8$ m/s, both the first and second PWT locations can be evaluated by Eq. (4.4) from the time domain results shown in Fig. 4.8. The evaluated PWT locations corresponding to the results shown in Fig. 4.8 are shown in Fig. 4.9, where the dashed lines indicate the start points and end points of the PWT sections.

Before measuring the pipe, electrical calibration (E-cal) of one flexible cable of the VNA was carried out to set the zero time reference plane at the end of the flexible cable. From Fig. 4.9, it is found that the evaluated locations are almost the same, respectively, for both the first and the second PWT sections, where the errors of the evaluation for both Fig. 4.9(a) and (b) are less than 1.5 mm, i.e. less than 0.06% of the length of the PUT. It means a quite high precision and high stability of the evaluation method has been realized. However, it should be noted that all the evaluated locations of the second PWT sections are not exact the center of the PWT sections but a little closer to the start of these PWT sections.

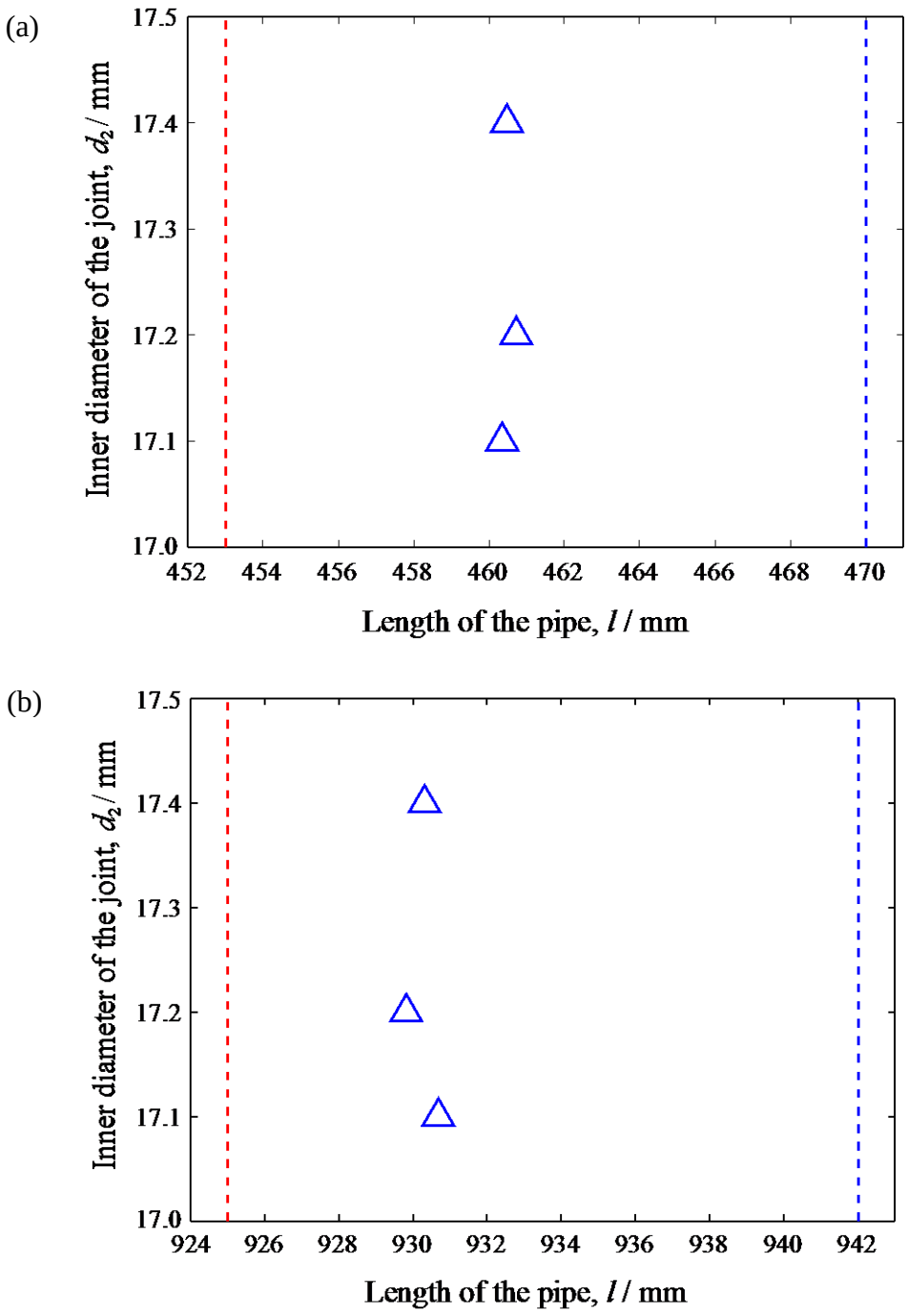

Fig. 4.9. Evaluated PWT locations for the condition that joint No. 4 working as the first PWT defect: (a) Evaluated location for the first PWT defects; (b) Evaluated location for the second PWT defects.

4.5. TDM for Evaluation of PWT Depth

From the TDM results shown above, it is found that the results have a relation with the PWT depths. The relation is that the more serious PWT has the larger reflection peaks. Therefore, it is possible to utilize this relation to evaluate the PWT depths. In this part, the results that shown in Fig. 4.4 that corresponding to the PUT shown in Fig. 4.2(a), and that shown in Fig. 4.5 that corresponding to the PUT shown in Fig. 4.2(b) are analyzed and utilized to evaluate the PWT depths.

4.5.1. Relation between Reflection Peaks and PWT Depths

From the TDM results, the values of reflection peaks can be obtained, and then we can find the relation between these values and the corresponding PWT depths.

For the results shown in Figs. 4.4 and 4.5, the relation between the reflection peaks and the PWT depths is shown in Fig. 4.10.

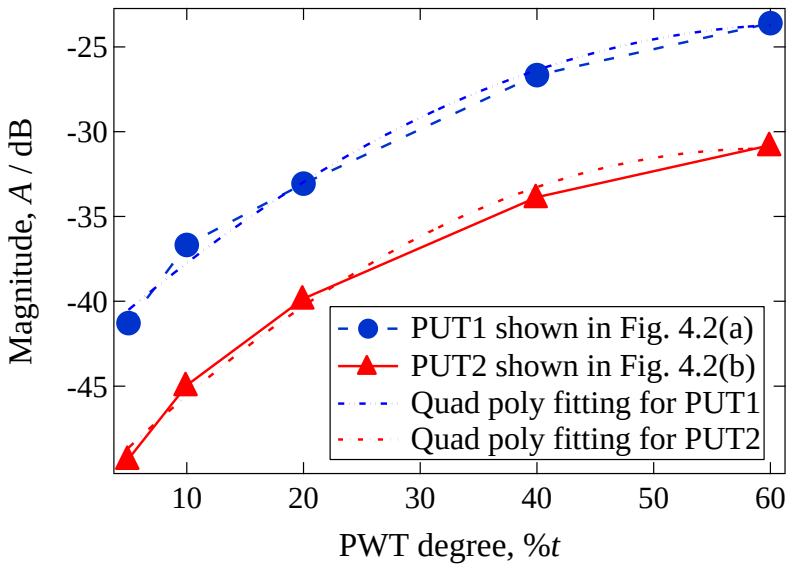

Fig. 4.10. Relationship between values of reflection peaks and PWT depths and their corresponding quadratic polynomial curve-fitting results

From Fig. 4.10, two typical relations have been found. The first one is that the value of the reflections peak is larger for the PWT defect that is located nearer to the sensor, such as the (magnitude) values of the reflection peaks of PUTs shown in Fig. 4.2(a) is about 6 ~ 8 dB larger than that of PUTs shown in Fig. 4.2(b) for the PWT defects having the same PWT depth. The second one is that an approximately quadratic polynomial relationship has been found between the values of reflection peaks and the PWT depths when the PWT defects are located at the same location.

These two relations make it theoretically possible to quantitatively evaluate the PWT depths utilizing the TDM results.

4.5.2. Evaluation of PWT Depths Using TDM

As shown in Fig. 4.10 and the two typical relations mentioned above, we can evaluate the PWT depths using the values of reflection peaks shown in the TDM results. However, as the approximately quadratic polynomial relationship is found between their values (i.e. three undetermined coefficients exist in the evaluation equation), there are at least three specimens should be used for calibration of the evaluation equation, and the evaluation equation is shown as follows,

$$D_{\mathrm{PWT}} = a_0 + a_1 A + a_2 A^2 \tag{4.5}$$

where D_{PWT} is the PWT depth having a value of the percentage of wall thickness t, a_i ($i = 1, 2, 3$) are the undetermined coefficients, and A is the (magnitude) value of the reflection peak expressed in dB.

For both the first kind of PUTs shown in Fig. 4.2(a) and the second kind of PUTs shown in Fig. 4.2(b), the TDM results of PUTs having PWT depths of 5%, 20%, and 40% of wall thickness shown in Figs. 4.4 and 4.5 are used for calibration. The evaluation

equations for the first and second kinds of PUTs are calibrated to be $D_{\text{PWT1}} = 201.8595 + 8.4441\,A + 0.0890\,A^2$, and $D_{\text{PWT2}} = 306.9335 + 11.7404\,A + 0.1139\,A^2$, respectively. The evaluated results are shown in Figs. 4.11 and 4.12, respectively.

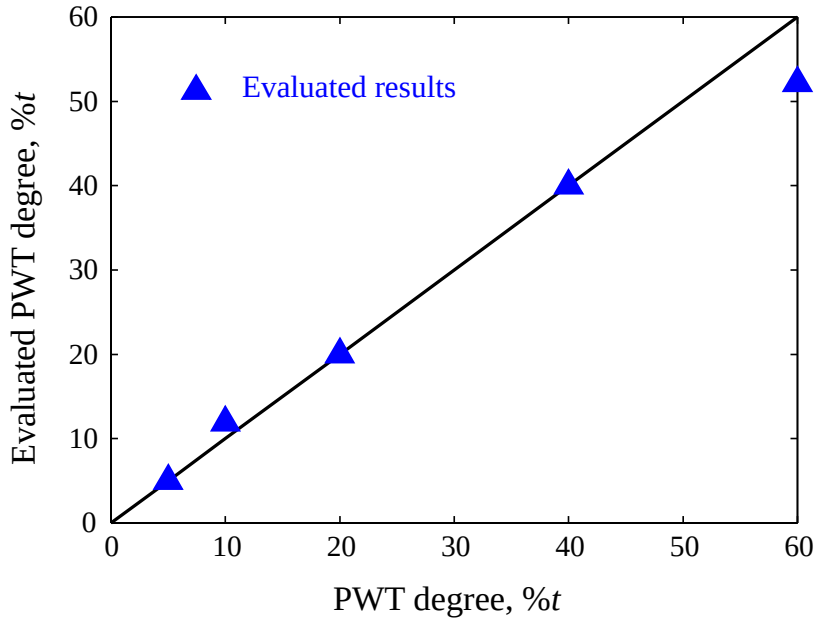

Fig. 4.11. Evaluated results of PWT depths using TDM results shown in Fig. 4.4.

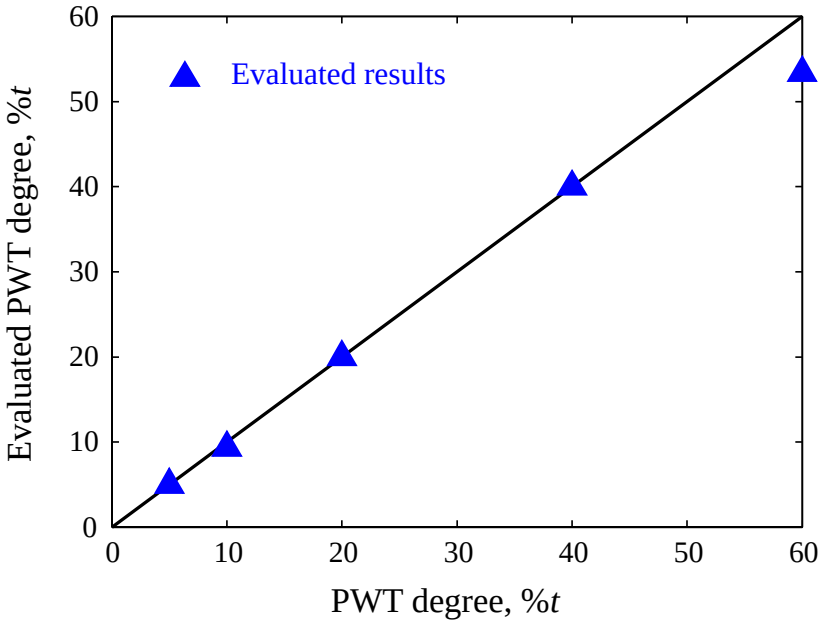

Fig. 4.12. Evaluated results of PWT depths using TDM results shown in Fig. 4.5.

Figs. 4.11 and 4.12 show the evaluated results of PUT having PWT depths of 10% and 60% of wall thickness for PUTs shown in Figs. 4.2(a) and 4.2(b). The evaluated results of the 10% PWT depths are 11.92% and 9.37%, respectively. Thus, the errors of evaluation are 1.92% and -0.63% of resolute values, and 19.2% and -6.3% of comparative values. In addition, the evaluated results of the 60% PWT depths are 52.15% and 53.38%, respectively. Thus, the errors of evaluation are -7.85% and -6.62% of resolute values, and -13.1% and -11.0% of comparative values. It is found that the error of evaluation is less than 10% of the resolute PWT values and less than 20% of the comparative PWT values.

4.5.3. Discussion of PWT Depth Evaluation Using TDM

In this section, the PWT depths evaluated using TDM results have been demonstrated. The error of evaluation is found to be less than 10% of the resolute PWT values and less than 20% of the comparative PWT values for both PUTs shown in Figs. 4.2(a) and 4.2(b).

The method of PWT depth evaluation using TDM results is much simpler in mathematical analysis than the evaluation method using FDM results as shown in Chapter 3. However, the three shortcomings for evaluation using TDM results are also obvious. Firstly, the error of evaluation is much larger than the method shown in Chapter 3. Secondly, as the approximately quadratic polynomial relation is obtained between the PWT depths and the values of reflection peaks in TDM results, three undetermined coefficients shown in Eq. (4.5) should be calibrated using three pipe specimens whose PWT depths are known. Thirdly, since the values of reflection peaks have a relation with the PWT locations, the pipe specimens (whose PWT depths are known to be used for calibration) should have the PWT defects located at the same location as the PUT.

The three shortcomings limit the evaluation of PWT depths using TDM results. As a result, this evaluation method is only significantly useful when a further simpler relation

between the PWT depths and the values of reflection peaks in TDM results can be discovered using signal processing or some other method.

4.6. Conclusion

In this research, we have demonstrated an efficient and nondestructive way of detecting the locations of the PWT defects in a long-distance metal pipe at the open-end condition, which is the most common case in the practice.

We achieved this by introducing a self-designed rotationally symmetric coaxial-line sensor used to excite microwave signals of TM_{01} mode in the PUT. Three kinds of pipes under different PWT conditions were used in the experiment and a VNA was used to work at the time domain. By analyzing the time domain response of signals and extracting the TOFs corresponding to the PWT locations, and calibrating the group velocity of microwaves at applied frequencies, the PWT locations were quantitatively evaluated.

The arithmetical mean errors of evaluation for all the three kinds of pipes used in the experiment are found to be less than 1.7 mm, i.e. less than 0.068% of the length of the corresponding pipe. It means that a quite precise and stable evaluation method has been established.

At the last part of this chapter, a method is established for PWT depths evaluation based on the relationship between the PWT depths and the values of reflection peaks in TDM results. However, there are three main shortcomings in this method, and they have limited the general use of this method.

Finally, it should be noted that this paper mainly aims to establish an efficient and stable method to determine the PWT location in a long-distance pipe regardless of the

start point and end point of a PWT area. This method can not separate the start point and end point of the PWT defect at present because of the resolution of signals, which cause the peaks of reflection to be not very sharp and that only overlapped signals can be detected when the peaks are close to each other. Therefore, after the location is determined, more detailed information such as the start and end points, as well as the shape of a PWT defect is necessary to be evaluated by a further development of the proposed method or by other local detection methods with further advance in accuracy.

References

[1] R. B. Dooley and V. K. Chexal, Int. J. Pres. Ves. Pip., **77**, 85 (2000).

[2] J. H. Lee and S. J. Lee, NDT & E Int., **42**, 222 (2009).

[3] A. Vageswar, K. Balasubramaniam, C. V. Krishnamurthy, T. Jayakumar, and B. Raj, NDT & E Int., **42**, 275 (2009).

[4] L. Liu and Y. Ju, NDT & E Int., **44**, 106 (2011).

[5] G. Kajiwara, J. Test. Eval., **33**, 295 (2005).

[6] T. Shimakawa, H. Takahashi, H. Doi, K. Watashi, and Y. Asada, Nuclear Eng. Des., **139**, 283 (1993).

[7] K. R. Leonard and M. K. Hinders, Ultrasonics, **43**, 574 (2005).

[8] H. Nishino, M. Takemoto, and N. Chubachi, Appl. Phys. Lett., **85**, 1077 (2004).

[9] J. Ding, Y. Kang, and X. Wu, NDT & E Int., **39**, 53 (2006).

[10] J. B. Nestleroth and R. J. Davis, NDT & E Int., **40**, 77 (2007).

[11] M. Kamaya, T. Suzuki, and T. Meshii, Int. J. Pres. Ves. Pip., **85**, 628 (2008).

[12] Y. Li, L. Sun, Z. Song, and Y. Zhang, Ultrasonics, **44**(S1), e1111 (2006).

[13] C. Aristégui, M. J. S. Lowe, and P. Cawley, Ultrasonics, **39**, 367 (2001).

[14] D. M. Pozar, Microwave Engineering (2nd Ed), New York: John Wiley&Sons, (1998).

[15] K. Abbasi, S. Ito, and H. Hashizume, Int. J. Appl. Electromagn. Mech., **28**, 429 (2008).

[16] K. Abbasi, N. H. Motlagh, M. R. Neamatollahi, and H. Hashizume, Int. J. Pres. Ves. Pip., **86**, 764 (2009).

[17] J. K. Piotrowski, Proc. 13 Int. Conf. Microw. Radar Wireless Commun. 2000 (MIKON-2000), **1**, 333 (2000).

[18] B. Gimeno and M. Guglielmi, Int. J. Microw. Millimet. Wave Comput. Aided Eng., **7**, 180 (1997).

[19] M. Adous, P. Queffelec, and L. Laguerre, Meas. Sci. Tech., **17**, 2241 (2006).

Chapter 5. Improved TDM for PWT Location and Length Evaluation

Abstract

We have proposed a nondestructive and high-efficiency way to detect the wall thinning locations in a long-distance metal pipe using microwaves. However, the superposed refection signals from both the start and end points of the pipe wall thinning (PWT) section in the pipe under test (PUT) made these two points difficult to be separated. This research aims to find a method with higher resolution to detect the locations of PWT and separate the start and end points of the PWT section. A vector network analyzer (VNA) and a self-designed coaxial-line sensor are utilized in this method to generate time domain response of microwave signals. The frequency range of the signals is optimized by analyzing the time domain response. Thereafter, by generating signals working at the optimum frequency range and extracting the time of flight (TOF) corresponding to PWT location, the PWT location is quantitatively evaluated. To approach a pipe with different PWT degrees and lengths, two brass pipes with inner diameters of 17.0 mm and lengths of 453 mm and 455 mm, respectively, and nine brass joints having different inner diameters and lengths used between the two pipes in turn to construct combined pipes were used in the experiment. For the optimum frequency range, the space resolution is evaluated to be 16.6 mm and less than the inner diameter of the PUT, and the maximum errors of evaluations are less than 3.5 mm and 9.6 mm (i.e. 0.38% and 1.04% of the full length of the PUTs) for the start and end points of the PWT sections, respectively. When the length of the PWT section increases, the evaluation precision also increases. It indicates that a quantitative method to evaluate the PWT locations in the pipe with high resolution and precision has been established.

Keywords: Microwave, metal pipe, PWT, remote detection, NDT&E, high resolution

5.1. Introduction

Metal pipes have been widely used in many industries since 1960s. During the service of the pipes, wall thinning is one of the most typical defects and especially, is an important future failure symptom to pressure vessels [1-3]. Pipe wall thinning (PWT) is a serious defect that can cause a normal pressure of the pipe wall to become overloading because of the thickness reduction, and the overloading pressure of the pipe wall can lead to burst of the pipe. Since twenty years ago, PWT has become a serious problem for many pipelines whose service time exceeding 20 years, and accidents due to PWT took place frequently around the world. These accidents have caused severe economical loss and social damages. Therefore, efficient and nondestructive detection of PWT defects as well as their quantitative evaluation, especially for long-distance pipes, are mandatory for the effective maintenance and the lifetime prediction of pipelines.

The PWT problem is twofold. One is the PWT degree, which means the depth and length of PWT. This is important information concerning the safety and lifetime of pipes. The other is the PWT location, which is important for the detection and maintenance of in-service pipes, especially long-distance pipes. Many researchers have focused on developing nondestructive testing (NDT) techniques for detecting PWT defects recently [3-11]. However, most of these methods can only inspect a pipe locally and all of them are difficult to measure long-distance pipes buried underground, placed in the walls of some concrete buildings, or under other similar conditions. In reality, all those methods generally take lots of time and labor to inspect a long-distance pipe, and they can only solve part of the first aspect of the PWT problem.

Microwave NDT has been used to overcome the shortcomings of the aforementioned

methods since microwave can propagate a long distance with quite little attenuation in a low-loss dielectric medium [12,13]. In microwave NDT, a metal pipe under test (PUT) can be promisingly taken as a circular waveguide [12-14], and all the energy of microwave signals is confined inside the pipe. Moreover, the propagation and attenuation of microwaves in the pipe are independent of the surrounding conditions of the pipe.

In our previous studies [12], the PWT degrees of a 2 m long pipe were remotely examined and quantitatively evaluated with a high precision using microwave signals at frequency domain. Meanwhile, time domain response (TDR) of microwave signals, which is derived from inverse fast Fourier Transform (IFFT) of the frequency domain signals has been used as an effectively tool to detect fault locations in a metal pipe in our previous studies [13]. However, our previous studies mainly aimed to establish an efficient and stable method to determine the PWT location in a long-distance pipe regardless of the start and end points of a PWT defect. Thus, only the pure low order TM_{01} mode was generated in the pipe by a self-designed rotationally symmetric coaxial-line sensor to act as the working mode. It is found that the response resolution for the time of flight (TOF) of the TM_{01} mode signals at time domain was not high enough and the reflection signals from the start and end points of the PWT section were overlapped and difficult to separate [13]. In this paper, we aim to improve the response resolution of the time domain signals, i.e. the ability to resolve two closely-spaced responses, or a measure of how close two responses can be to each other and still be distinguished from each other [15], by optimizing the sweeping frequency range, and thereby find out a method to detect the PWT locations with higher resolution, which can successfully evaluate the start and end points of a PWT defect with length no less than the inner diameter of the pipe. Moreover, a reference pipe under the open condition was utilized to calibrating the group

velocity at the optimum frequency range in this work to make the calibration easier to carry out than the previous method that calibrated at the short circuit condition [13].

It should be noted that the response resolution depends upon the time domain mode, the frequency range and the relative propagation velocity of the signal path.

5.2. Experimental Approach

The experimental instrument is composed of a microwave vector network analyzer (VNA), a self-designed coaxial-line sensor, and a PUT as shown in Fig. 5.1.The sensor is made from a standard coaxial line cable and connector [13], and it serves as both the transmitting and receiving port of microwave signals.

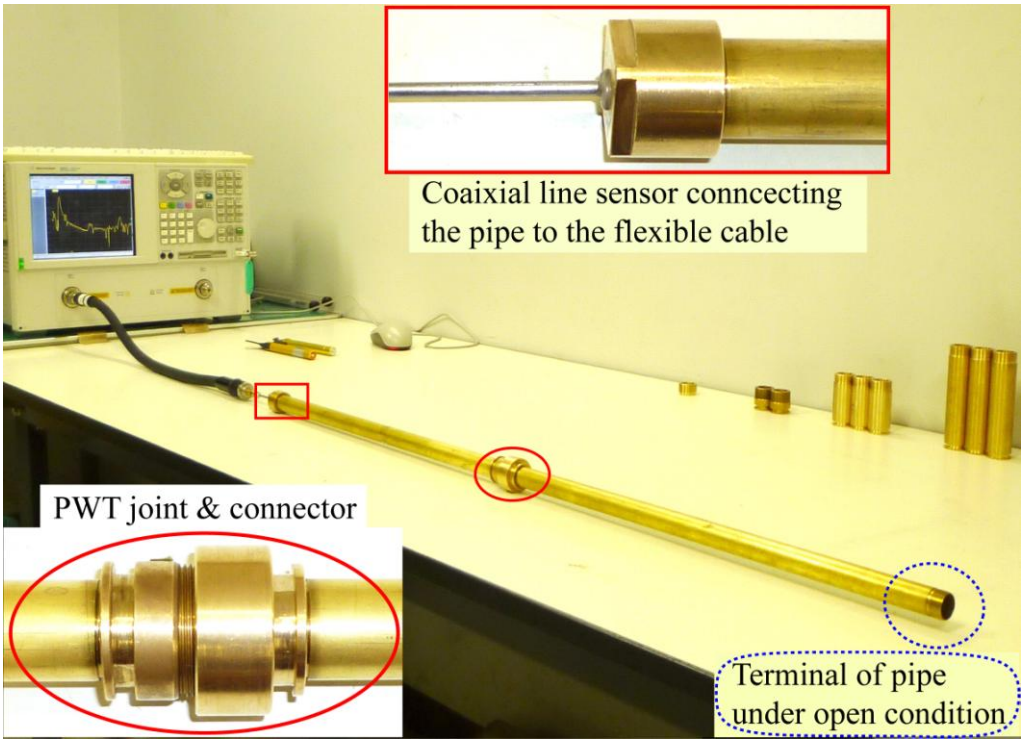

Fig. 5.1. Overall photograph of the experimental instrument (the three insets are the enlarged images of the corresponding parts of the pipe, and the correspondence is carried out using markers of solid line panes, ellipses, and dashed line ellipses).

The pipe specimens tested in this paper are composed of two pipes with inner diameter of $d_1 = 17.0$ mm, nine joints, and a connector used to connect each joint between the two pipes. All of them are made of brass. The lengths of the two pipes numbered as P1 and P2 in this paper are $l_{11} = 453$ mm, $l_{12} = 455$ mm, respectively, and the wall thickness of the pipes is $t = 1.0$ mm. The nine joints which are used to introduce PWT sections with different PWT degrees and lengths in the combined pipe are separated to three groups, i.e. A, B, and C, by their different length of $l_2 = 17.0$, 51.0, and 102.0 mm. In each group, there are three joints with different inner diameters, d_2, as specified in TABLE 5.1. These joints are used in turn to construct different PWT sections in the combined pipe. During the experiment, nine combined pipes with PWT defects of different degrees and lengths were constructed using the two pipes, the connector and joints mentioned above, as shown in Fig. 5.2. In this figure, l_0 denotes the total length of the PUT, d_1 is the inner diameter of the section free from PWT, while *t* is the wall thickness of the pipe. t_1 and l_2 represent the PWT depth and length of the PWT sections, respectively. $d_0 = 6.5$ mm denotes the inner cable of the sensor is 6.5 mm protruding.

TABLE 5.1. Detailed geometric parameters of the joints.

Joint's number	A1	A2	A3	B1	B2	B3	C1	C2	C3
Length, l_2 (mm)		17.0			51.0			102.0	
Inner diameter, d_2 (mm)	17.1	17.2	17.4	17.2	17.4	17.8	17.2	17.4	17.8
PWT degree, %*t*	5%*t*	10%*t*	20%*t*	10%*t*	20%*t*	40%*t*	5%*t*	10%*t*	20%*t*

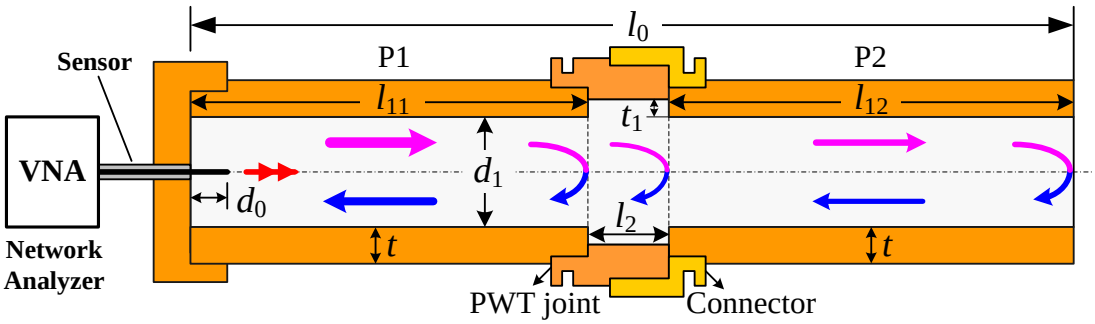

Fig. 5.2. Schematic diagram of the experimental setup and the signal propagation and reflection within the combined pipe.

Before measuring the pipe, electrical calibration (E-cal) of one flexible cable of the VNA was carried out to set the zero time reference plane at the end of the flexible cable. During the experiment, microwave signals were generated by the VNA and coupled into the pipe through the coaxial-line sensor. The VNA was set to work at the S11 mode, so that microwave signals reflected from both the PWT sections and the terminal of the PUT were detected by the same port of the sensor. When sweeping the frequency within a proper range, the corresponding amplitudes of response signals containing PWT information were measured, and the frequency domain signals were obtained directly, from which the time domain results was calculated through IFFT. TOF, which is defined as the arrival time of any reflection peak of the microwave signals going from and returning to the reference zero time interface in this paper, can then be extracted from the time domain analysis of the signals. The frequency range of microwave signals is one of the most important factors for the response resolution at time domain and thus the space resolution of the evaluated locations. The detailed method of how to select the frequency range will be discussed in the next section.

Moreover, to obtain high precision (range resolution) in the time domain, sweeping

points of 1601 are adopted in the experiment, and the time domain results are designed to be measured in two steps. The first step is to measure the pipe at time domain range that is wide enough to contain all the time domain responses, i.e. responses according to all the discontinuous points from the calibrated zero time interface to the terminal of the PUT. After getting the general information of the PWT location in the pipe, the second step is to measure the pipe at a focused range (much narrower range) of time domain where big reflection occurs. As a result, more detailed information of the PWT can be extracted from the reflection peaks expanded on the time axis. The two steps are carried out with the same number of sweeping points. Thus, the time precision of the second step is much higher as the smaller time range being measured.

5.3. Theoretical Analysis

As it is mentioned above, the frequency domain response (FDR) of the microwave signals is obtained directly when sweeping the frequency at a fixed range, and the TDR is calculated through IFFT of the FDR. By calibrating the group velocity in the pipe and analyzing the TOF corresponding to the PWT location at the time domain, the PWT locations can be quantitatively evaluated. The resolution of evaluated locations is determined by the response resolution of the reflected signals at the time domain. In this section, we focus on the theoretical analysis of relations between the frequency range selection and the time domain response, especially, the response resolution of the signals. Some of the waveguide theory and experimental results are utilized together here to optimizing the frequency range of the microwave signals in order to evaluate PWT locations with high-resolution. In addition, the analysis of the TOF data and the calibration of the group velocity of the microwave signals propagating in the pipe are

also introduced in this section.

5.3.1. Frequency Range Optimization and Time Domain Response

To obtain a good response resolution in time domain, the working frequency range should be optimized. Ideally, if the frequency domain stimulus is continuous over an infinite frequency range, the response resolution will be infinitely high. However, the VNA is only capable of measuring over a finite frequency range. Therefore, the time domain signals obtained from the IFFT of the frequency domain signals has a finite impulse width for a response, such as reflection from a discontinuity along the pipe. Thus, the finite impulse width limits the ability to resolve two closely spaced responses. Moreover, the impulse sidelobes limit the dynamic range of the time domain response by hiding low-level responses within the sidelobes of higher level responses.

The influence of the sidelobes can be reduced by windowing, i.e. by filtering the frequency domain data prior to conversion to the time domain, to produce an impulse stimulus with lower sidelobes. Thus, windowing can greatly enhance the effectiveness in viewing time domain responses in magnitude. However, the sidelobe reduction is achieved by windowing with the trade-off of increased impulse width [15]. Generally speaking, the maximum window can reduce the sidelobes better than the normal and minimum windows, but at the same time, it will increase the impulse width most seriously, and the condition is vice versa for the minimum window. For a compromise, the normal window is utilized in this paper as a golden mean of windowing, which can make the sidelobes comparatively low and obtain high time domain responses viewing in magnitude.

Because the PWT has approximately equal discontinuities at the start and end points of the PWT section, the response resolution for responses of equal amplitude can be

used approximately to estimate the response resolution of the reflections at the PWT section although the masking effect making the later reflection a little weaker than the reflection at the start of the PWT. In addition, as there is a particular frequency range for any mode of the microwaves, bandpass impulse of the signals is utilized to detect the PWT locations. In this case, the relationship between the response resolution, ΔT, and the frequency span, Δf, is expressed as follows [15],

$$\Delta T = 1.95/\Delta f \tag{5.1}$$

As the signals should propagate twice the distance and the 2-way travel time involved for the refection measurement, the space resolution, Δl, is expressed as,

$$\Delta l = v_g \cdot \Delta T / 2 \tag{5.2}$$

where v_g is the group velocity in the PUT.

It is found from Eq. (5.1) that the impulse width is inversely proportional to the frequency span of the measurement. If the impulse is too wide, two closely spaced impulses, such as reflections from the start and end points of a short PWT section, will overlap and become difficult to be separated from each other. The only way to reduce the impulse width is to increase the frequency span after the window type has been selected. However, we can not increase the frequency span arbitrarily due to the multi-mode transmission characteristics of the pipe (circular waveguide).

The problem of the multi-mode transmission is that each of the responses of different modes may present as an individual peak in time domain, due to the different group velocities for different transmission mode. In this case, it is almost impossible to evaluate the PWT location from the time domain responses, because we can not relate these responses to their corresponding transmission modes and group velocities. In this

sense, it should be conservatively said that the response resolution can be improved by increasing the frequency span only if the microwave signals at single mode are transmitting in the waveguide.

Under the premise of single-mode transmission in the PUT, to adopt a working frequency range as wide as possible, the sweeping frequency should be set between the cutoff frequencies of two neighboring working modes that can be excited in the PUT, such as that the lower frequency of the frequency range should be slightly higher than the cutoff frequency of the dominant mode and the upper frequency should be slightly lower than the cutoff frequency of the first high order mode for the single dominant mode. As shown in Fig. 5.1, the coaxial line sensor is used to generate microwave signals, and its rotationally symmetric structure when connected to the circular waveguide results to that only TM_{0m} modes are generated [13], and the dominant mode is TM_{01} [14]. However, the coaxial line sensor used in the experiment is not exactly a coaxial line, since the inner cable is designed to be $d_0 = 6.5$ mm protruding to excite strong signals in the pipe, as the schematic diagram shown in Fig. 5.2. This protrusion excites a small amount of TM_{nm} ($n \neq 0$) and TE_{0m} modes in addition to the TM_{0m} modes. Since the cutoff frequencies of TE_{0m} modes are the same as those of TM_{1m} modes, only the cutoff frequencies of TM_{nm} modes are considered in this paper and they are given as [14],

$$f_{c\mathrm{TM}_{nm}} = cp_{nm}/(\pi d) \tag{5.3}$$

where d is the inner diameter of the pipe, and c is the speed of light in free space. p_{nm} represents the mth root of the Bessel function $J_n(x)$, i.e. $J_n(p_{nm}) = 0$. The values of p_{nm} for the first few TM_{nm} modes are given in TABLE 5.2. It can be calculated from Eq. (5.3) and TABLE 5.2 that cutoff frequencies for the first few TM_{nm} modes are in sequence of TM_{01}, TM_{11} (and TE_{01}), TM_{21}, TM_{02}, TM_{31}, TM_{12} (and TE_{02}) modes.

TABLE 5.2. Values of p_{nm} for the first few TM_{nm} modes of a circular waveguide.

n \ m	1	2	3	4
0	2.4048	5.5201	8.6537	11.7915
1	3.8317	7.0156	10.1735	13.3237
2	5.1356	8.4172	11.6198	14.7960
3	6.3802	9.7610	13.0152	16.2235
4	7.5883	11.0647	14.3725	17.6160

Based on the previous analysis, a stable mode with high response resolution to evaluate the PWT locations can be found out, and the dominant TM_{01} mode and several high order modes are investigated as follows.

To obtain the single dominant mode, the frequency range between the cutoff frequencies of the dominant TM_{01} mode and the first high order mode, TM_{11} or TE_{01} mode (they have the same cutoff frequency), should be utilized. The cutoff frequencies of TM_{01} and TM_{11} modes can be calculated from Eq. (5.3) and TABLE 5.2. When increasing the frequency, it seems theoretically that lower order modes also exist at frequencies beyond the cutoff frequency of higher order mode. The experimental results also show that multi-reflection happens and two reflection peaks appear after the upper limit of the frequency range beyond the cutoff frequency of the higher order mode, i.e. TM_{11} mode. As a result, the resolution improvement by simply increasing the upper limit of frequency range to obtain a wider frequency span for the dominant TM_{01} mode is limited by the cutoff frequency of the first high order mode.

On the other hand, it is found from the experimental results that the reflection peak corresponding to the dominant TM_{01} disappears and only the reflection peak that

corresponding to the high mode exists after the lower limit of the frequency range increases to be higher than the cutoff frequency of the high order mode, i.e. TM_{11}/TE_{01} mode. Furthermore, the reflection peak keeps being single until the upper limit of frequency range reaches the cutoff frequency of TM_{31} mode (which is the next mode of TM_{02}), provided that the lower frequency limit is kept invariable and higher than the cutoff frequency of the TM_{11}/TE_{01} mode. During this process, the reflection peak becomes sharper and sharper with the increase of the upper frequency limit, which means the improvement of response resolution. This phenomenon is in accordance with Eq. (5.2). The working mode of this frequency range should be the hybrid mode of TM_{11} and TE_{01} modes, and also a small part of TM_{02} mode. Moreover, it is found from the experiment that the TM_{02} mode takes more shares after the upper frequency having reached the cutoff frequency of TM_{31} mode and, thereafter, the reflection peak corresponding to TM_{02} mode appears. As a result, the frequency range with the lower and upper limits being the cutoff frequencies of TM_{11}/TE_{01} mode and TM_{31} mode, respectively, is taken as the working frequency range in this paper, within which the single reflection of the first high-order mode and a relatively wide frequency span can be satisfied. The cutoff frequencies of TM_{11}/TE_{01} mode and TM_{31} mode can be obtained from Eq. (5.3) and TABLE 5.2.

As mentioned above, the sensor structure determines that microwaves of TM_{0m} modes are mainly generated in the pipe. As a result, the cutoff frequency of the high-order TM_{02} mode is quite important and the cutoff frequency of the next high-order mode after it is taken as the upper frequency of the frequency range having single reflection of the first high-order mode.

In addition, when keeping the lower limit of the frequency range as the cutoff

frequency of the TM_{02} mode and increasing the upper limit, the frequency range having single reflection corresponding to the TM_{02} mode can also be obtained. However, the upper limit is found from the experiment to be also TM_{31} mode. Therefore, the frequency span of this frequency range is narrower than that of the previous frequency range that having single reflection of the first high-order mode. Moreover, when taking the cutoff frequency of TM_{31} mode as the lower limit of the frequency range and increasing the upper limit, TM_{02} and TM_{31} modes coexist and multi-reflections happen. Furthermore, more severe multi-reflections happen at higher frequencies because of the coexistence of more higher-order modes and, as a result, the condition becomes more complicated and makes it much more difficult to extract some reflection information corresponding to a single mode. Therefore, too high frequency ranges are not suitable for quantitative inspection, and the previous frequency range that having a comparatively wide frequency span and a single reflection (response) for a single discontinuity is taken as the optimum frequency range for inspecting a long-distance pipe.

5.3.2. Signal Analysis and TOF from the Discontinuity of the PUT

Since air is used as the medium in the pipe, the wave impedance of a circular waveguide for microwaves of TM_{nm} mode and TE_{0m} mode is expressed as [14],

$$Z_{\mathrm{TM}_{nm}} = \eta_0 \sqrt{1-[\lambda p_{nm}/(\pi d)]^2} \text{ , and } Z_{\mathrm{TE}_{0m}} = \eta_0 \Big/ \sqrt{1-[\lambda p_{1m}/(\pi d)]^2} \qquad (5.4)$$

where $\eta_0 = \sqrt{\mu_0 / \varepsilon_0}$ is the intrinsic impedance (μ_0 and ε_0 are permeability and permittivity, respectively), $\lambda = c/f$ is the wavelength of microwaves in free space at frequency f.

From Eq. (5.4), it is found that the wave impedances for both TM and TE modes are function of the inner diameter of the pipe. Therefore, change in the diameter of the

circular waveguide will cause discontinuity in the wave impedance, and thus the reflection from the location of this discontinuity. This is shown in the schematic diagram in Fig. 5.2. The TOFs of the microwave signals reflected from different discontinuities are utilized for evaluating the PWT locations.

5.3.3. Group Velocity Calibration and PWT Location Evaluation

Group velocity is a function of the working mode and operating frequencies of microwave in the circular waveguide filled with air and can be expressed as follows [14],

$$v_g = c \cdot \sqrt{1-(f_c / f)^2} \tag{5.5}$$

where f_c is the cutoff frequency, such as $f_{c\mathrm{TM}_{01}} = cp_{01}/(\pi d)$ for the dominant TM_{01} mode.

The group velocity of microwave is prerequisite for evaluating PWT locations quantitatively. As mentioned above, the operating frequency range of the microwave signals can not be too narrow in order to obtain a high resolution in the time domain. Therefore, the group velocity of the wave package which consists of multiple frequencies is difficult to be decided from Eq. (5.5) by a single frequency. In this work, the group velocity is confirmed using a calibration method.

For microwaves propagating in the pipe at a given frequency range, the group velocity v_g can be calibrated by measuring a reference pipe whose length is known and whose inner diameter d_1 is exactly the same as the defect-free section of the PUT. When carrying out this calibration, the source signals should be set exactly the same (at the same frequency range and after the same E-cal) as the ones utilized in the PWT evaluations. To carry out the measurement easily, the terminal condition of the reference pipe is set to be open. After measuring the TOF corresponding to twice the full length of the reference pipe, the group velocity can be calculated as [13],

$$v_g = 2l_{\text{cal}} / T_{\text{end}} \tag{5.6}$$

where l_{cal} is the length of the reference pipe, and T_{end} is the difference of TOFs corresponding to the signals reflected from the start and the end of the pipe.

Using the group velocity and the TOF corresponding to the PWT section of the PUT, the PWT location can be evaluated by

$$l_{\text{PWT}} = v_g \cdot T_{\text{PWT}} / 2 \tag{5.7}$$

where l_{PWT} and T_{PWT} represent the PWT location and TOF corresponding to the PWT, respectively. The presence of factor 1/2 in Eq. (5.7) is due to the fact that the signals should propagate twice the distance between the sensor and the PWT section after being transmitted and received by the sensor.

5.4. Experimental Results and PWT Evaluation

Considering the theoretical analysis mentioned above, only the experimental results for the two typical modes, the dominant TM_{01} mode and the first high-order mode, are presented in this part. In addition, the experimental results are quantitative evaluated and the evaluated results based on the mentioned two modes are also shown and discussed here.

5.4.1. Measured Results under the Dominant Mode

To obtain the single dominant mode, the frequency range between the cutoff frequencies of TM_{01} and TM_{11}/TE_{01} modes was utilized in the experiment. For a PUT having a defect-free inner diameter of 17.0 mm, the cutoff frequencies of TM_{01} and TM_{11} modes were calculated from Eq. (5.3) and TABLE 5.2 to be 13.5 and 21.5 GHz, respectively. Moreover, to avoid the edge dispersion of the frequency range and insure the single

mode propagation, the frequency range between 13.0 and 21.0 GHz were utilized in the experiment, where the frequency span Δf_1 is 8.0 GHz. Since the normal window and the bandpass measurement were utilized in the experiment, the response resolution was calculated from Eq. (5.1) to be $\Delta T_1 = 243.8$ ps.

As mentioned in the theoretical analysis section, the group velocity is determined through a calibration method. When using pipe P1 at the open condition to calibrate the group velocity, the experimental results of time domain signals are shown in Fig. 3, where the reflection from the terminal of the pipe can be clearly observed. This figure is obtained through IFFT of the frequency domain result. As mentioned in the experimental approach, focused measurement of small time range is implemented to improve the precision at time domain, and the obtained results are inserted in Fig. 5.3. As the zero time reference plane is set at the end of the flexible cable of the VNA rather than at the beginning of the pipe, the reflection peaks corresponding to all of the connections are presented together with the reflection from the pipe terminal.

The largest peak at the left side of Fig. 5.3 is caused by the mismatch between the sensor and the pipe, as the inserted enlarged image of the sensor shown in Fig. 5.1. From the focused result within time range of 0 ~ 1.0 ns shown in Fig. 5.3, the TOF corresponding to this mismatch is found to be 0.743 ns, which is the TOF at the beginning of the pipe. While the last large peak at the right side of Fig. 5.3 corresponds to the reflection from the open end of the reference pipe P1, and the TOF is found to be 5.483 ns from the focused result in the time range of 5.0 ~ 6.0 ns. Therefore, the difference of TOFs corresponding to the signals reflected from the beginning and the end of the pipe is calculated to be $T_{\text{end1}} = 4.740$ ns. As the length of pipe P1 is $l_{\text{cal}} = 453$ mm, the group velocity is calculated to be $v_{g_1} = 1.911 \times 10^8$ m/s from Eq. (5.6).

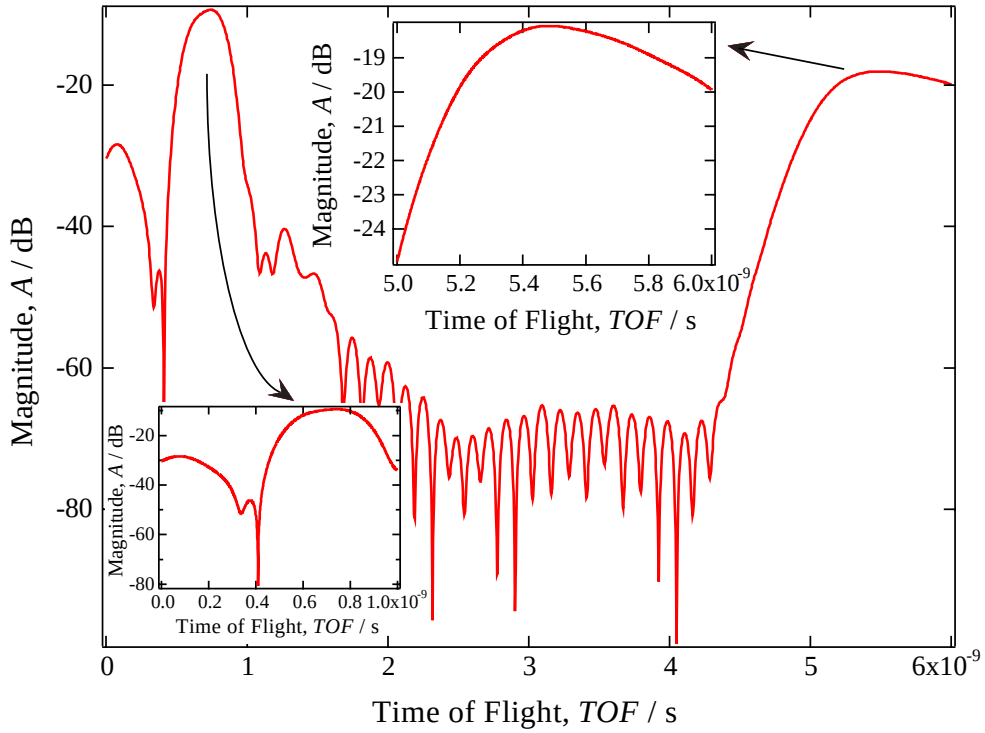

Fig. 5.3. Time domain experimental results of pipe P1 measured under the dominant mode. To show the results clearer, two figures are inserted: one is focused on time range 0 ~ 1.0 ns for the reflections from the sensor, the other is focus on time range 5.0 ~ 6.0 ns for the reflections from the end of the pipe.

When considering $\Delta T_1 = 243.8$ ps, the space resolution is estimated to be $\Delta l_1 = 23.3$ mm from Eq. (5.2), which is about 1.4 times of the inner diameter of the pipe (17.0 mm). As a result, the reflections from the start and end points of any PWT section having length less than this length will overlap and be difficult to separate, and it is theoretically impossible to separate the start and end points of the PWT joints that have such a length.

As mentioned above, nine PUTs composed of three groups of PWT joints shown in TABLE 5.1 are measured in the experiment. Time domain results of the PUTs composed of the group of shortest PWT joints having length of 17.0 mm (group A) are shown in Fig. 5.4. It is found that large reflection peak for each PUT with a different PWT degree

occurs around 5.5 ns, which is the TOF from the PWT section.

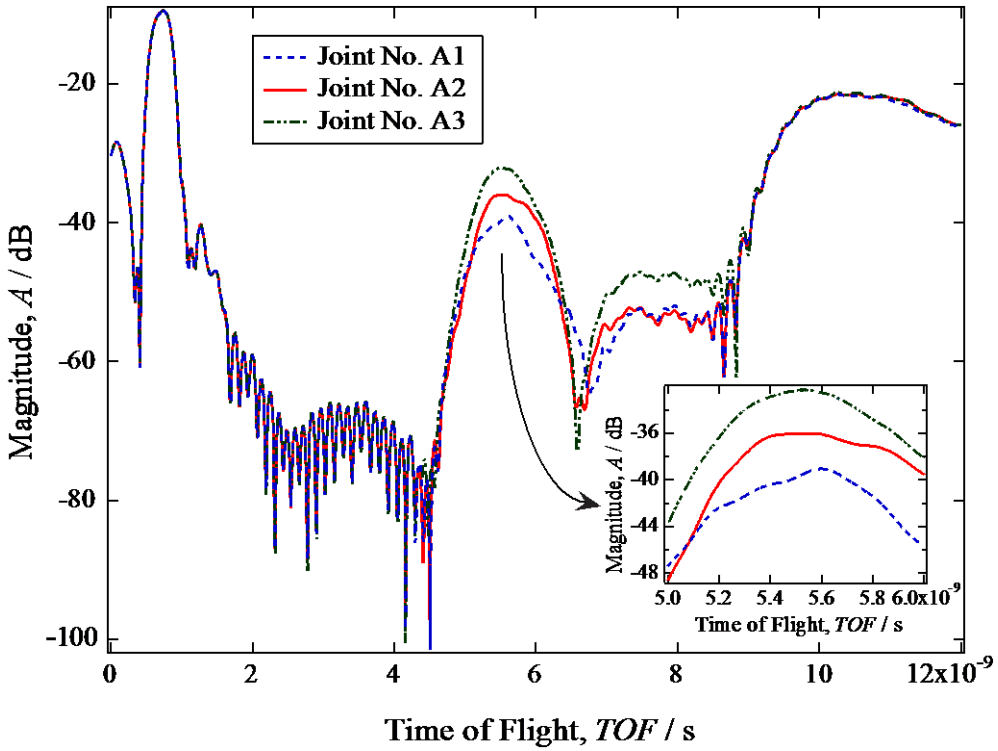

Fig. 5.4. Experimental results of the combined pipe shown in Fig. 5.2 when connecting with different degrees of PWT joints (group A) that have length of 17.0 mm; the inset figure is the focused part at time range 5.0 ~ 6.0 ns around the TOFs of the reflections from PWT defects.

In addition, focused results within the time range of 5.0 ~ 6.0 ns are also shown in Fig. 5.4. The TOFs corresponding to these large peaks of reflection are almost the same for all the PWT sections with different PWT degrees. It confirms the possibility and stability to detect small PWT defect. In addition, a large reflection peak also appears around 11.0 ns, which is caused by the reflection at the open end of the PUT.

As the response resolution is not high enough, the two reflection peaks caused by the start and end points of the PWT section (as shown in Fig. 5.2) are not sharp enough and,

as a result, only the peak of the overlapped signals is observed.

Time domain results of the PUTs composed of the group of middle length PWT joints with length of 51.0 mm (group B) are shown in Fig. 5.5. It is found that two reflection peaks for each PUT occur between 5.0 to 6.5 ns, which are the TOFs from the start and end points of the PWT section. Focused results within the time range of 5.0 ~ 6.5 ns are inserted in Fig. 5.5. Different from the first group of PUTs, the TOFs corresponding to the start and end points of the PWT sections are clearly separated. Moreover, Fig. 5.5 can also be used as an effective way to estimate the response resolution comparatively accurately.

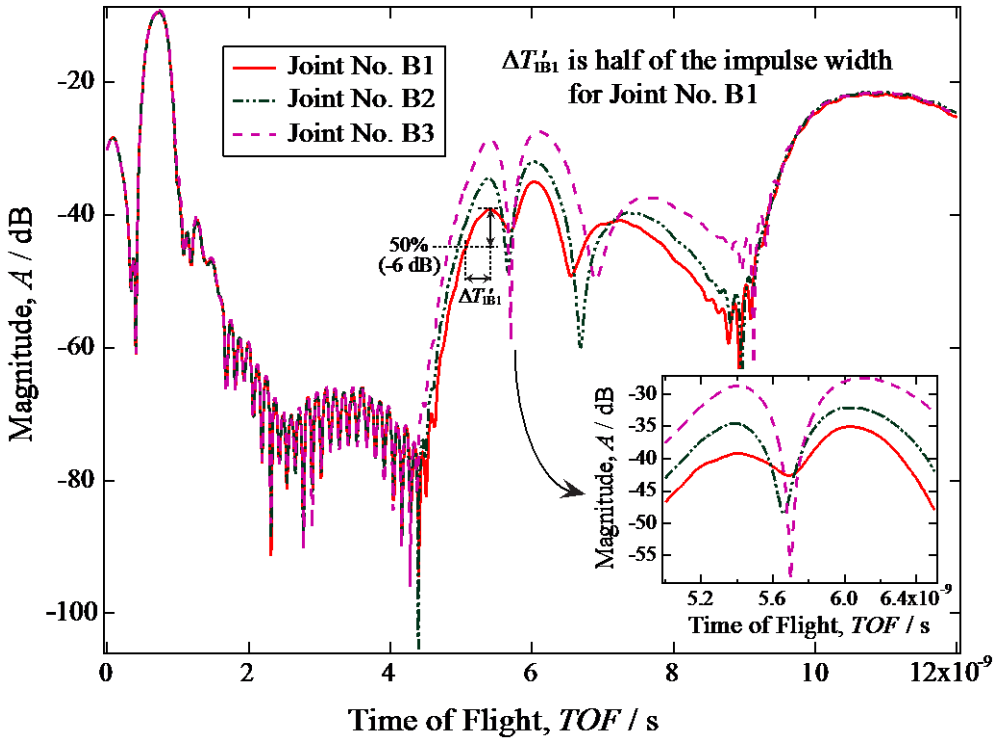

Fig. 5.5. Experimental results of the PUT composed of pipe P1 and different degrees of PWT joints (group B) having length of 51.0 mm and then pipe P2; the inset figure is the focused part at time range 5.0 ~ 6.5 ns around the TOFs of the reflections from PWT defects.

As the response resolution is equal to the 50% (-6.0206 dB) points of the impulse for responses of equal amplitude [15], the approximate but more accurate response resolutions, $\Delta T'_{1B1} = 360.0$, $\Delta T'_{1B2} = 300.5$, and $\Delta T'_{1B3} = 307.5$ ps, for responses of approximately equal amplitude are obtained from the experimental results shown in Fig. 5.5. When taking the average response resolution, $\Delta T'_1 = 322.7$ ps, into account, the space resolution is estimated to be $\Delta l'_1 = 30.8$ mm from Eq. (5.2), which is more than 1.8 times of the inner diameter of the pipe. It is almost the same but a little wider than the one ($\Delta l_1 = 23.3$ mm) estimated from Eqs. (5.1) and (5.2) when only using the frequency span. It means that, after utilizing the normal window, the widest frequency span for the dominant mode can only give birth to a response resolution generally no higher than the length of 1.8 times of the pipe's inner diameter.

Time domain results of the PUTs composed of the group of longest length PWT joints (group C) with length of 102.0 mm, i.e. six times of the length of the inner diameter, are shown in Fig. 5.6. It is found that reflection peaks caused by multi-reflection occur and make it difficult to distinguish which peak is the reflection peak corresponding to a specifically discontinuity. Moreover, as the large reflection peaks for each PUT occur between 5.0 to 7.0 ns, which are the TOFs of reflection signals from the start and end points of the PWT section and also the multi-times of reflections occur between the start and end points of the PWT section due to its long length, focused results within the time range of 5.0 ~ 7.0 ns are inserted in Fig. 5.6.

As mentioned above, because multi-times reflection unfortunately happens when the length of the PWT section is too long, such as longer than approximately six times of the length of the inner diameter of the PUT, it will be quite difficult to evaluate the PWT locations for pipes with such a long PWT defect using the frequency range of the single dominant mode.

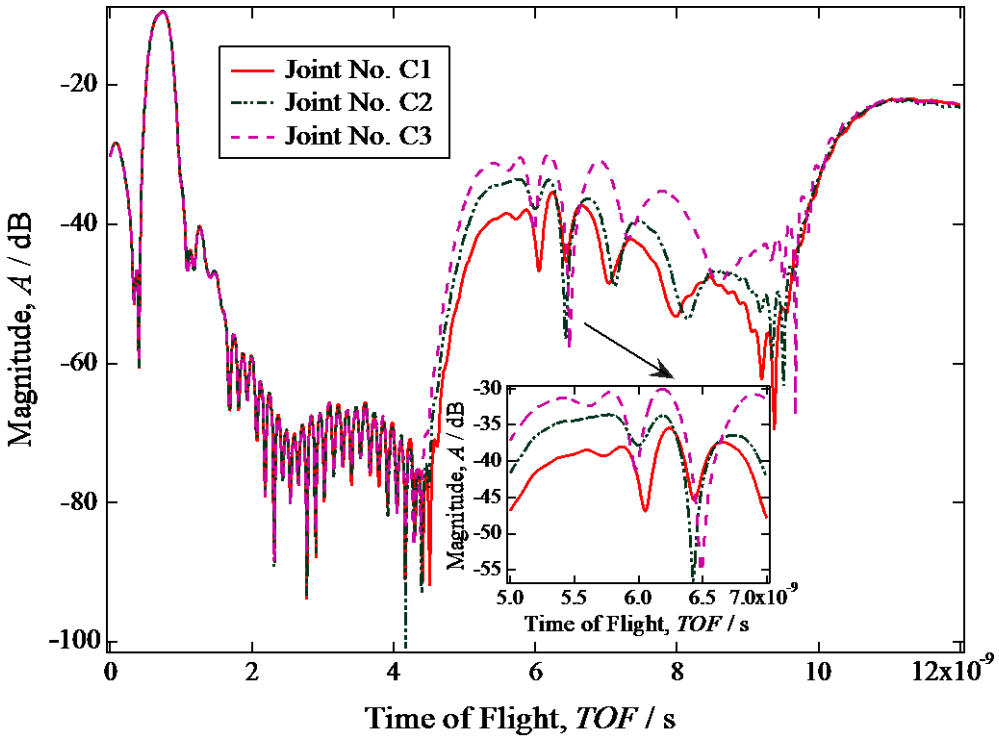

Fig. 5.6. Experimental results of the PUT composed of pipe P1 and different degrees of PWT joints (group C) having length of 102.0 mm and then pipe P2; the inset figure is the focused part at time range 5.0 ~ 7.0 ns around the TOFs of the reflections from PWT defects.

5.4.2. PWT Evaluation under the Dominant Mode

The experimental results measured under the dominant mode are evaluated in this part.

Considering the calibrated group velocity in pipe P1, i.e. $v_{g_1} = 1.911 \times 10^8$ m/s, and using the TOFs of the group A joints derived from the time domain responses shown in Fig. 5.4, the PWT locations of the PUTs are evaluated using Eq. (5.7), and the results are shown in Fig. 5.7. In this figure, the values at the abscissa of the two dashed lines correspond to the actual locations of the start and end points of the PWT section, i.e. 453 mm and 470 mm, respectively.

Since reflections corresponding to the start and end points of the PWT section overlaps and cannot be separated as shown in Fig. 5.4, the evaluated locations shown in Fig. 5.7 are between the start and end points of the PUT which are the total effect caused by the reflections from both the start and end points. From Fig. 5.7, it is found that the evaluated PWT location is a little closer to the start point of the PWT section for the PUT having a more severe PWT, i.e. it means that the reflection from the start point of the PWT section is stronger and causes the peak of overlapped signals to be a little closer to the start point. Taking the middle location of the PWT section, i.e. 461.5 mm, as a datum plane, the absolute errors of evaluation for the PUTs composed of joints No. A1, A2, and A3 are 2.9, 1.0, and 3.7 mm, respectively. These errors are less than 0.40% of the full length, $l_{01} = 925$ mm, of the PUTs. The maximum evaluation error happens at the PUT that having the most severe PWT, and this evaluated location is the closest one to the start point of the PWT section.

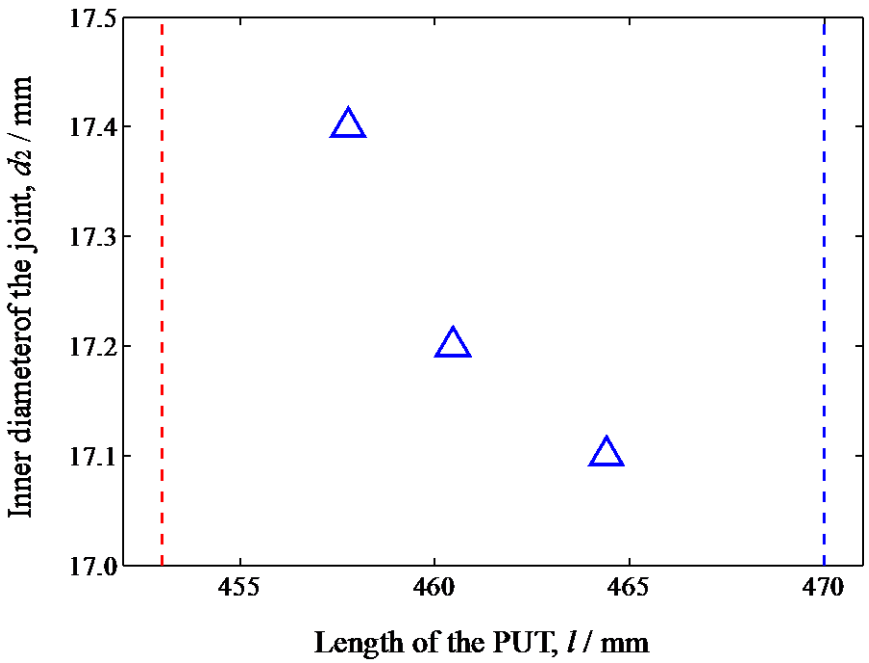

Fig. 5.7. Evaluated results for PUTs having a PWT length of 17.0 mm whose experimental results shown in Fig. 5.4.

For the experimental results of PUTs using the group B joints having length of 51.0 mm as shown in Fig. 5.5, after using the group velocity $v_{g_1} = 1.911 \times 10^8$ m/s for evaluation, the evaluated results for both the start and end points of the PWT locations are shown together in Fig. 5.8. It is the same as in Fig. 5.7, the values at the abscissa of the two dashed lines shown in Fig. 5.8 correspond to the actual locations of the start and end points of the PWT section, i.e. 453 mm and 504 mm, respectively.

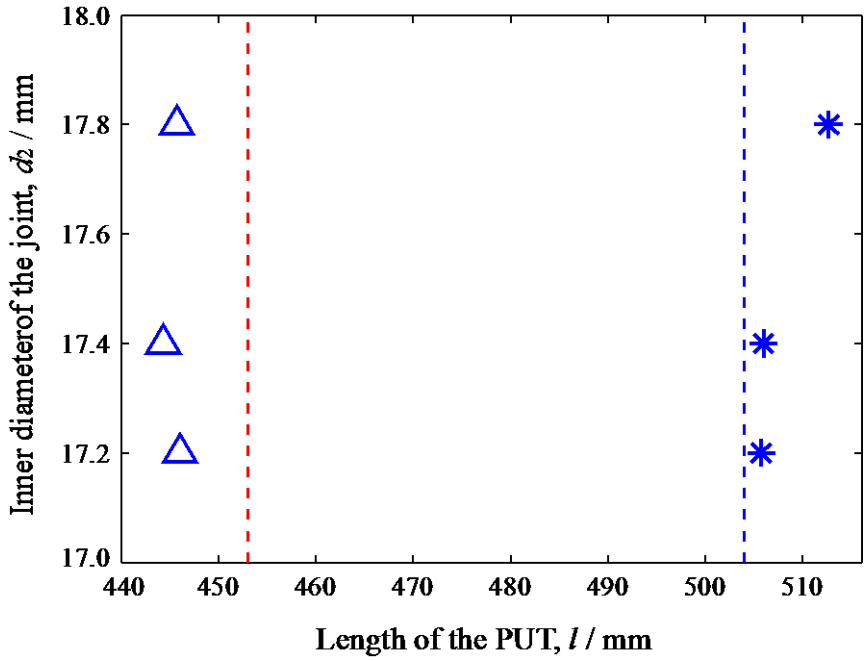

Fig. 5.8. Evaluated results for PUTs having a PWT length of 51.0 mm whose experimental results shown in Fig. 5.5.

As shown in Fig. 5.8, all the PWT locations evaluated for the start points of the PWT sections are ahead of the practical location for the start points, and that for the end points of the PWT sections are behind the practical location for the end points. The arithmetical mean error of the evaluation for the start points is less than 7.4 mm, i.e. less than 0.80% of the full length, $l_{02} = 959$ mm, of the PUTs, and that for the end points is less than 4.1

mm, i.e. less than 0.43% of the full length of the PUTs. Moreover, the maximum error of evaluation for both the start and end points of the PWT sections is 8.7 mm, i.e. less than 0.91% of the full length of the PUTs. Thus, it can be conservatively said that the precision of evaluation for this frequency range is less than 10.0 mm.

For the experimental results of PUTs using the group C joints having length of 102.0 mm as shown in Fig. 5.6, using the group velocity $v_{g_1} = 1.911 \times 10^8$ m/s for evaluation, the evaluated results for the three major reflection peaks corresponding to both the start and end points of the PWT locations and the multi-reflection are shown together in Fig. 5.9. The values at the abscissa of the two dashed lines shown in Fig. 5.9 is the same as in Fig. 5.8, which correspond to the actual locations of the start and end points of the PWT section, i.e. 453 mm and 555 mm, respectively.

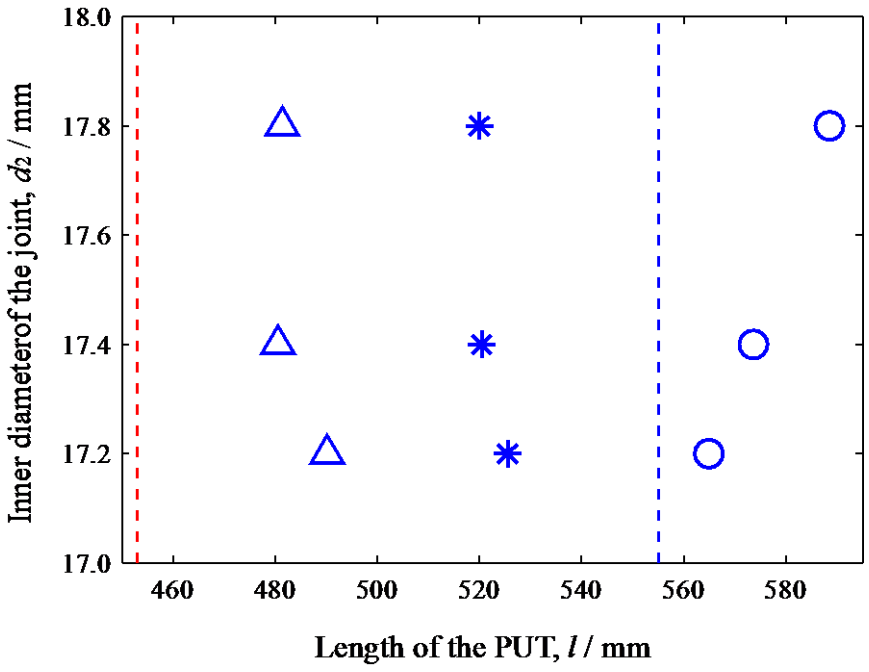

Fig. 5.9. Evaluated results for PUTs having a PWT length of 102.0 mm whose experimental results are shown in Fig. 5.6.

As found in Fig. 5.9, multi-times of reflection happen when the length of the PWT section is too long, such as longer than six times of the length of the inner diameter of the PUT. As a result, it will be difficult to evaluate the PWT locations for pipes with such a long PWT defect using the frequency range of the single dominant mode.

5.4.3. Measured Results under the First High Order Mode

To obtain the first high order mode, the frequency range between the cutoff frequencies of TM_{11}/TE_{01} and TM_{31} modes was utilized in the experiment. For a PUT with inner diameter of 17.0 mm, the cutoff frequencies of TM_{11} and TM_{31} modes were calculated from Eq. (5.3) and TABLE 5.2 to be 21.5 and 35.8 GHz, respectively. To avoid the edge dispersion of the frequency range and insure the single mode propagation, the frequency range between 22.0 and 35.0 GHz were utilized in the experiment, where the frequency span Δf_2 is 13.0 GHz. As the normal window and the bandpass measurement were utilized in the experiment, the resolution was calculated from Eq. (5.1) to be 150.0 ps.

When using pipe P1 at the open condition to calibrate the group velocity, the experimental results of time domain signals are shown in Fig. 5.10, where the reflection from the end of the pipe is clearly observed. This figure is obtained through IFFT of the frequency domain result. Focused measurement of small time range is utilized to improve the precision at time domain, and the obtained results are inserted in Fig. 5.10. The reflection peaks corresponding to all of the connections are presented together with the reflection from the pipe terminal.

It is the same as shown in Fig. 5.6 that the largest peak at the left side of Fig. 5.10 is caused by the mismatch between the sensor and the pipe, and the TOF corresponding to this mismatch is found to be 0.7206 ns, which is the TOF at the beginning of the pipe. In addition, the TOF of the reflection from the end of the pipe P1 is found to be 4.1176 ns

from the focused result in the time range of 4.0 ~ 4.2 ns. The difference of TOFs corresponding to the signals reflected from the beginning and the end of the pipe is calculated to be $T_{\text{end2}} = 3.397$ ns. As the length of pipe P1 is $l_{\text{cal}} = 453$ mm, the group velocity is calculated to be $v_{g_2} = 2.667 \times 10^8$ m/s from Eq. (5.6). When taking $\Delta T_2 = 150.0$ ps into account, the space resolution is estimated to be $\Delta l_2 = 20.0$ mm from Eq. (5.2).

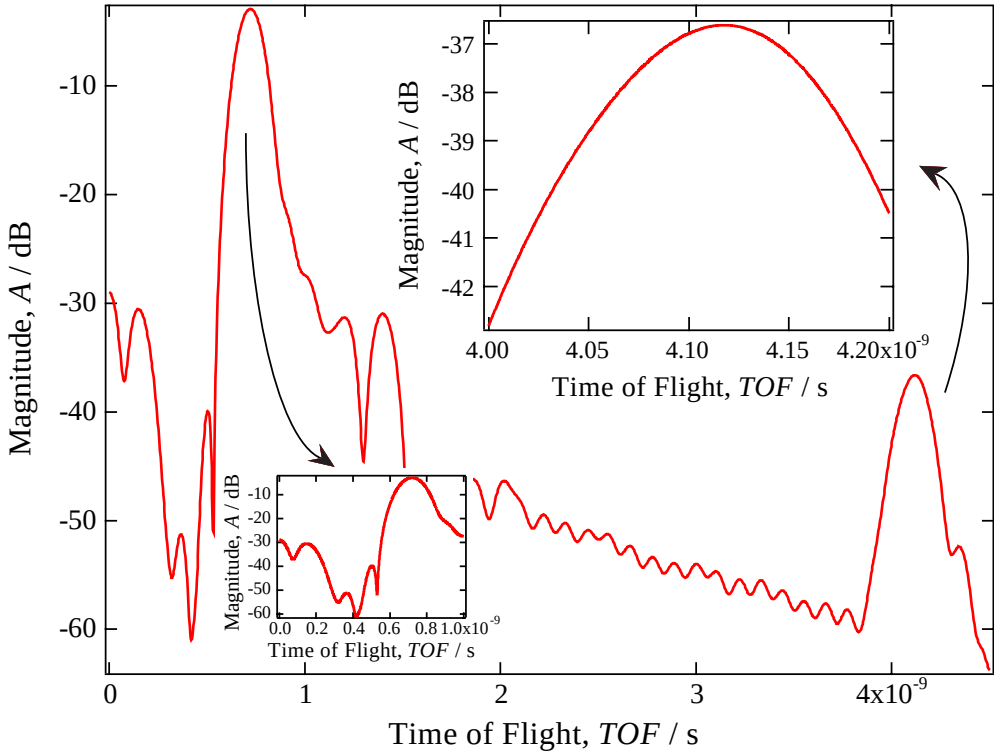

Fig. 5.10. Time domain experimental results of pipe P1 measured under the first high order mode.

Time domain results of the PUTs composed of the group of shortest PWT joints having length of 17.0 mm (group A) are shown in Fig. 5.11. It is found that two reflection peaks for each PUT occur between 4.0 to 4.5 ns, which are the TOFs from the start and end points of the PWT section. To view these two reflection peaks clear, focused results within

the time range of 4.0 ~ 4.4 ns are also shown in Fig. 5.11. Different from the experimental results of PUTs measured under the dominant mode, the TOFs corresponding to the start and end points of the PWT sections are clearly separated. The TOFs corresponding to these large peaks of reflections for both the start and end points of the PWT sections are almost the same for all the PWT sections with different PWT degrees. It shows the possibility and stability of this method. In addition, a group of large reflection peaks also appears around 7.6 ns, which is caused by the reflection at the open end of the PUTs.

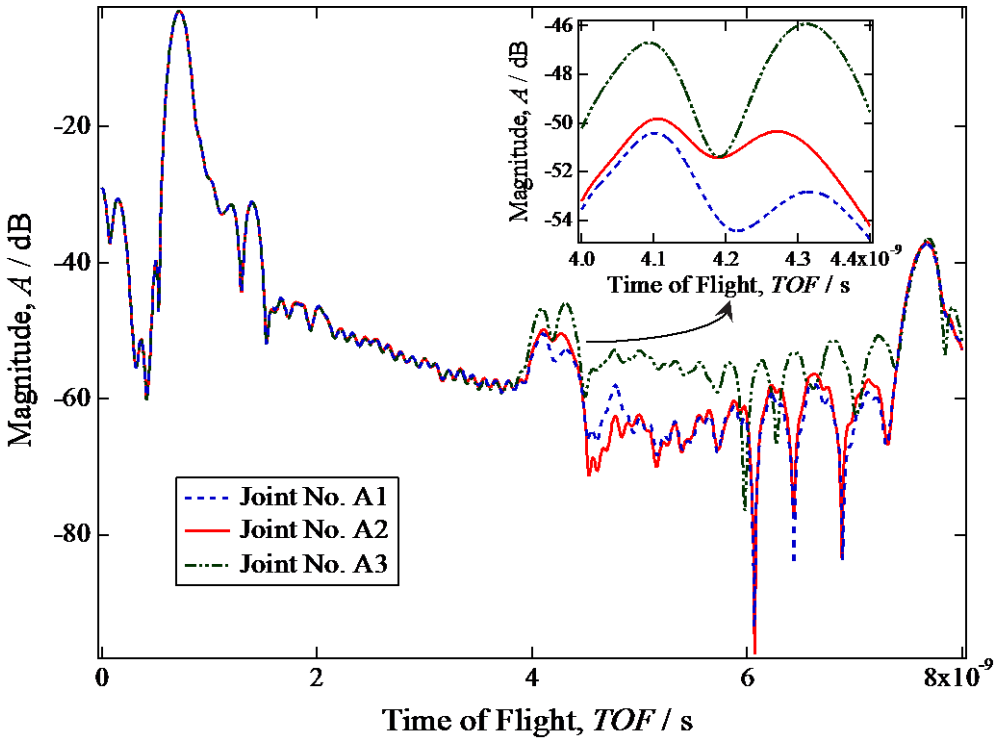

Fig. 5.11. Experimental results of the PUT composed of pipe P1 and different degrees of PWT joints (group A) having length of 17.0 mm and then pipe P2; the inset figure is the focused part at time range 4.0 ~ 4.4 ns around the TOFs of the reflections from PWT defects.

Time domain results of the PUTs composed of the group of middle length PWT joints with length of 51.0 mm (group B) are shown in Fig. 5.12. It is found that two reflection

peaks for each PUT occur between 4.0 to 5.0 ns, which are the TOFs from the start and end points of the PWT section. To view these two reflection peaks clear, focused results within the time range of 4.0 ~ 4.7 ns are inserted in this figure. Comparing to the experimental results for the PUTs having the group A joints, the TOFs corresponding to the start and end points of the PWT sections are more clearly separated. Moreover, Fig. 5.12 can also be used as an effective way to estimate the response resolution comparatively accurately.

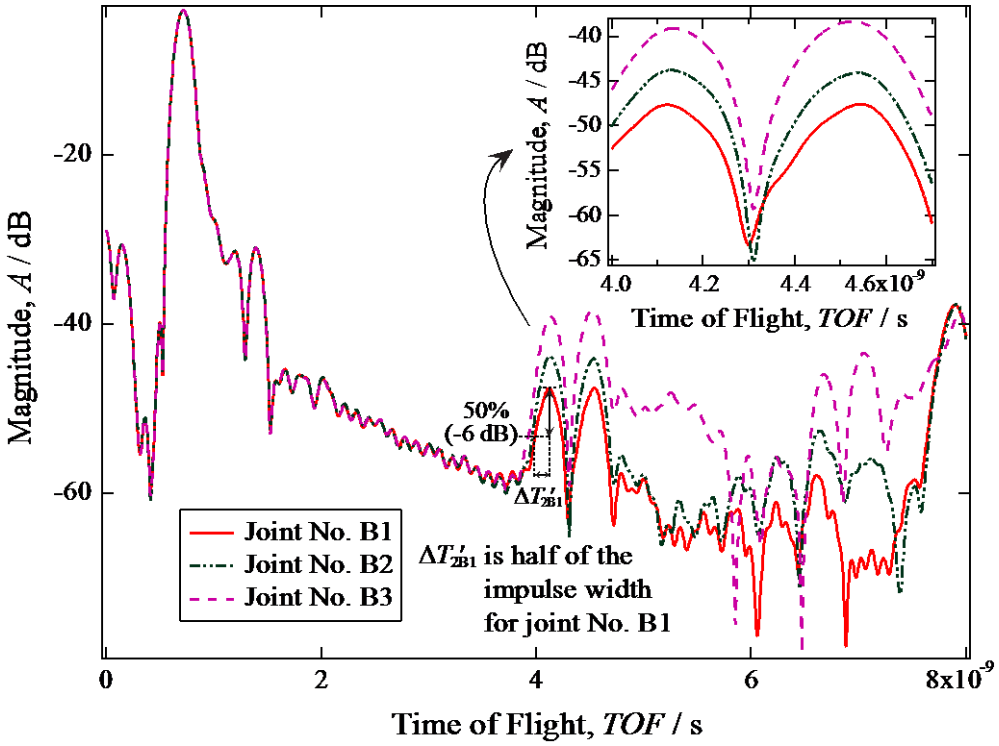

Fig. 5.12. Experimental results of the PUT composed of pipe P1 and different degrees of PWT joints (group B) having length of 51.0 mm and then pipe P2; the inset figure is the focused part at time range 4.0 ~ 4.7 ns around the TOFs of the reflections from PWT defects.

As the response resolution is equal to the 50% (-6.0206 dB) points of the impulse for

responses of equal amplitude [15], the approximate but more accurate response resolutions, $\Delta T'_{2B1} = 125.6$, $\Delta T'_{2B2} = 125.5$, and $\Delta T'_{2B3} = 122.7$ ps, can be obtained from the experimental results shown in Fig. 5.12. When using the average response resolution, $\Delta T'_2 = 124.6$ ps, the space resolution is estimated to be $\Delta l_2 = 16.6$ mm from Eq. (5.2), which is almost the same but a little sharper than the one estimated from Eq. (5.1) when only using the frequency span. The value of the space resolution is less than the inner diameter of the pipe, and it means that the microwaves working at this frequency range are capable to remotely separate the start and end points of a PWT defect having the PWT length no less than the inner diameter of a PUT.

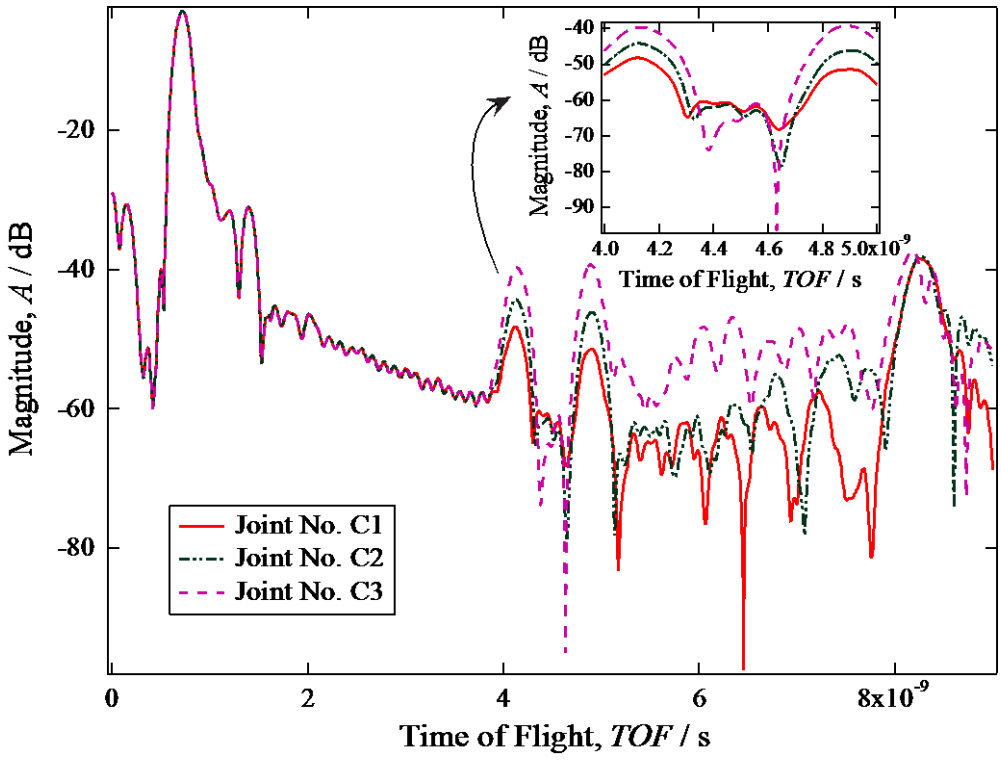

Fig. 5.13. Experimental results of the PUT composed of pipe P1 and different degrees of PWT joints (group C) having length of 102.0 mm and then pipe P2; the inset figure is the focused part at time range 4.0 ~ 5.0 ns around the TOFs of the reflections from PWT defects.

Time domain results of the PUTs composed of the group C joints are shown in Fig. 5.13. It is found that large reflection peaks for each PUT occur between 4.0 to 5.0 ns, which are the TOFs of reflection signals from the start and end points of the PWT section. To show these two peaks clear, focused results within the time range of 4.0 ~ 5.0 ns are inserted in this figure. It is quite different from the results for PUTs measured under the dominant mode, multi-times reflection have no severe effect on the experimental results and will not affect the evaluation.

5.4.4. PWT Evaluation under the First High Order Mode

The experimental results measured under the first high-order mode are to be evaluated in this part.

After using the calibrated group velocity in pipe P1, i.e. $v_{g_2} = 2.667 \times 10^8$ m/s, the TOFs of the PUTs with the group A joints derived from the time domain responses shown in Fig. 5.11, and Eq. (5.7) for evaluation, the evaluated results of the PWT locations are shown in Fig. 5.14. In Fig. 5.14, the values at the abscissa of the two dashed lines correspond to the actual locations of the start and end points of the PWT section, i.e. 453 mm and 470 mm, respectively.

As shown in Fig. 5.14, all the PWT locations evaluated for the start points of the PWT sections are ahead of the corresponding practical location, and that for the end points of the PWT sections are behind the corresponding practical location. In addition, the arithmetical mean error of the evaluation for the start points is less than 2.3 mm, i.e. less than 0.25% of the full length, $l_{01} = 925$ mm, of the PUTs, and that for the end points is less than 7.3 mm, i.e. less than 0.80% of the full length of the PUTs. Moreover, the maximum errors of evaluation are less than 3.5 mm and 9.6 mm (i.e. 0.38% and 1.04% of the full length of the PUTs) for the start and end points of the PWT sections,

respectively. Therefore, it can also be conservatively said that the precision of evaluation for PWT defects having such a length is less than 10.0 mm under this frequency range.

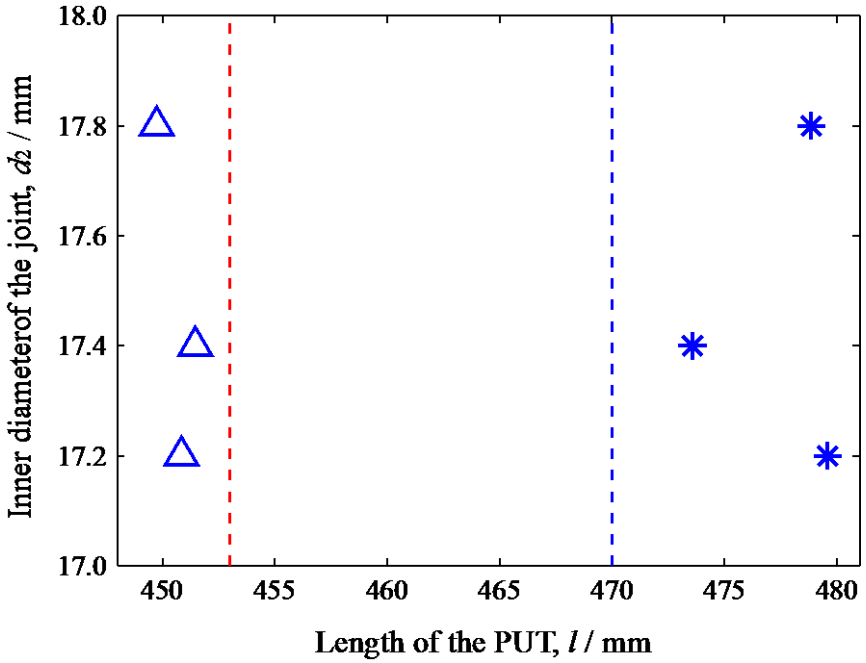

Fig. 5.14. Evaluated results for PUTs having a PWT length of 17.0 mm whose experimental results shown in Fig. 5.11.

For the experimental results of PUTs using the group B joints shown in Fig. 5.12, after using the group velocity $v_{g_2} = 2.667 \times 10^8$ m/s into Eq. (5.7) for evaluation, the evaluated results for both the start and end points of the PWT locations are shown together in Fig. 5.15. The values at the abscissa of the two dashed lines shown here correspond to the actual locations of the start and end points of the PWT section, i.e. 453 mm and 504 mm, respectively.

As shown in Fig. 5.15, all the PWT locations evaluated for the start points of the PWT sections are quite close to the practical location for the start points, and that for the end points of the PWT sections are a little behind the corresponding practical location.

The arithmetical mean error of the evaluation for the start points is less than 1.5 mm, i.e. less than 0.16% of the full length, $l_{02}=959$ mm, of the PUTs, and that for the end points is less than 4.8 mm, i.e. less than 0.50% of the full length of the PUTs. Moreover, the maximum errors of evaluation are less than 2.3 mm and 5.9 mm (i.e. 0.24% and 0.62% of the full length of the PUTs) for the start and end points of the PWT sections, respectively.

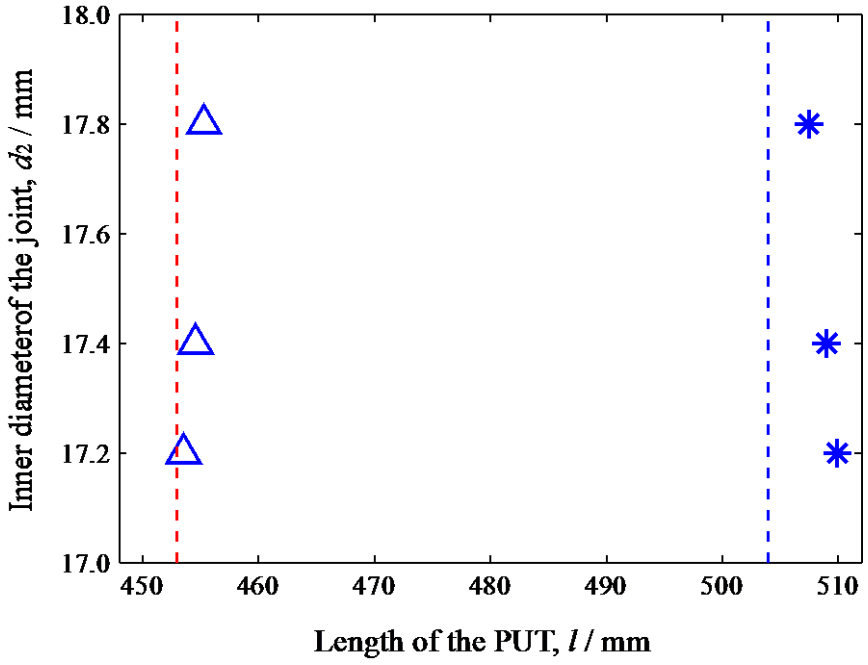

Fig. 5.15. Evaluated results for PUTs having a PWT length of 51.0 mm whose experimental results shown in Fig. 5.12.

For the experimental results of PUTs using the group C joints shown in Fig. 5.13, after using the group velocity $v_{g_2}=2.667\times10^8$ m/s into Eq. (5.7) for evaluation, the evaluated results for both the start and end points of the PWT locations are shown together in Fig. 5.16. The values at the abscissa of the two dashed lines shown here correspond to the actual locations of the start and end points of the PWT section, i.e. 453 mm and 555 mm, respectively.

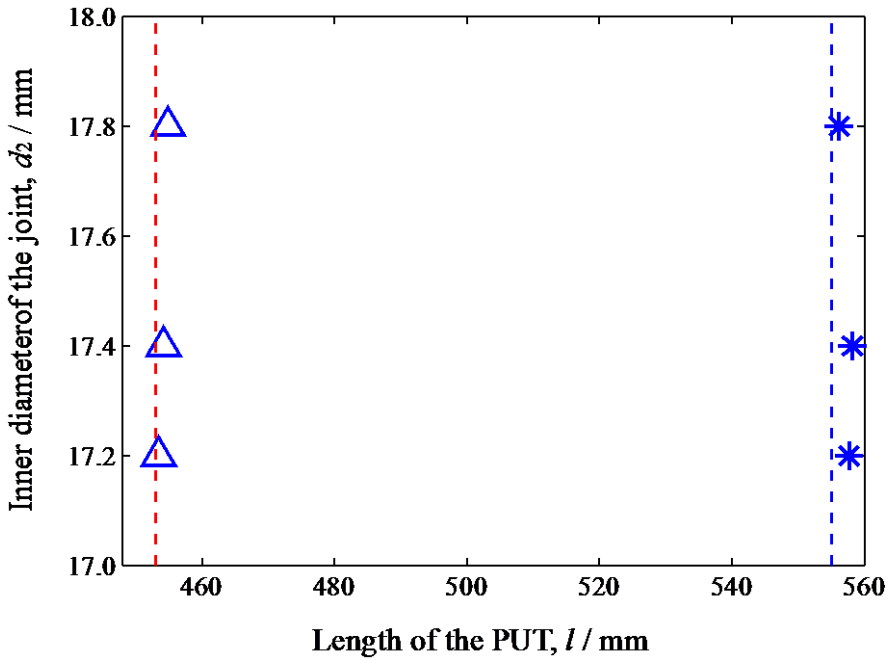

Fig. 5.16. Evaluated results for PUTs having a PWT length of 102.0 mm whose experimental results shown in Fig. 5.13.

The evaluated results shown in Fig. 5.16 is similar as that shown in Fig. 5.15, where all the PWT locations evaluated for the start points of the PWT sections are quite close to the practical location for the start points, and that for the end points of the PWT sections are a little behind the corresponding practical location. The arithmetical mean error of the evaluation for the start points is less than 1.2 mm, i.e. less than 0.12% of the full length, $l_{03} = 1{,}010$ mm, of the PUTs, and that for the end points is less than 2.3 mm, i.e. less than 0.23% of the full length of the PUTs. Moreover, Moreover, the maximum errors of evaluation are less than 1.9 mm and 3.2 mm (i.e. 0.19% and 0.32% of the full length of the PUTs) for the start and end points of the PWT sections, respectively.

5.4.5. Comparison of Experimental and Evaluated Results

The experimental and evaluated results have already been presented together for both the dominant mode and the first high-order mode. A brief comparison will be made in

this section.

The results for microwaves working at the widest frequency range of the single dominant mode showed that the space resolution of the single dominant mode is about 1.4 to 1.8 times of the inner diameter of the PUT. In the case that the PWT length less than this resolution, the reflections from the start and end points of the PWT section will overlap and can not be separated. The maximum errors of evaluation for all the PWT defects having a length of three times of the inner diameter of the PUT are found to be 8.7 mm, i.e. less than 0.91% of the full length of the PUTs, for both the start and end points of the PWT sections. However, it should be mentioned out that when the length of the PWT section becomes too long, such as longer than five or six times of the inner diameter, multi-times of reflections between the start and end points of the PWT section happen and their superposition making the overlapped reflection peaks not corresponding the start and end points of the PWT section and making them being impossible to separate.

While the results for microwaves working at the widest frequency range of the single first high-order mode showed that the resolution is a little less than the inner diameter of the PUT, which is much better than the former method. In this case, the precision of evaluation for all the PWT defects having the same length as the inner diameter of the PUT are found to be less than 3.5 mm and 9.6 mm (i.e. less than 0.38% and 1.04% of the full length of the PUTs) for the start and end points of the PWT sections, respectively. When the length of the PWT section increasing, the evaluation precision will also increase. For all the PUTs having a length of the PWT sections to be three times of their inner diameter, the precisions of evaluation are found to be less than 2.3 mm and 5.9 mm (i.e. 0.24% and 0.62% of the full length of the PUTs) for the start

and end points of the PWT sections, respectively. Moreover, for all the PUTs having a length of the PWT sections to be six times of the inner diameter, the precisions of evaluation are found to be less than 1.9 mm and 3.2 mm (i.e. 0.19% and 0.32% of the full length of the PUTs) for the start and end points of the PWT sections, respectively. Therefore, it is predicted that the longer the PWT section having the higher the evaluation precision for microwaves working at the first high order mode.

5.5. Conclusion

In this research, we have demonstrated an efficient, nondestructive, high precision and high resolution way to detect the locations of PWT defects in a long-distance metal pipe.

PUTs composed of three groups PWT joints that having different PWT degrees and lengths were used together in the experiment and a microwave VNA was used to generate time domain responses of signals at different frequency ranges. Moreover, we introduced a significant self-designed rotationally symmetric coaxial-line sensor in this research to excite microwave signals in the PUT. Through analyzing the time domain response of signals, optimizing the frequency range, extracting the TOF information corresponding to PWT locations, and calibrating the group velocity of microwaves propagating at the applied frequencies, the PWT locations were quantitatively evaluated.

As the time domain response of microwave signals can be obtained through the IFFT of the frequency domain signals, the frequency range selection determines the response resolution at the time domain. As a result, the high resolution of location evaluation was achieved through optimizing the frequency range of the microwave signals when keeping the signals working under a single mode. Results of microwaves working at both the single dominant TM_{01} mode and the single first high order mode are presented

in this paper.

The results showed that the resolution of the single dominant mode is about 1.4 to 1.8 times of the inner diameter of the PUT, while that of the single first high-order mode is a little less than the inner diameter of the PUT, which is much better than the former method and its frequency range is used as the optimum frequency range.

For the optimum frequency range, the errors of evaluation for all the PWT defects having the same length as the inner diameter of the PUTs, are found to be less than 3.5 mm (i.e. less than 0.38% of the full length of the PUTs) and 9.6 mm (i.e. less than 1.04% of the full length of the PUTs) for the start and end points of the PWT sections, respectively. When the length of the PWT section increases, the evaluation precision will also increase. It means that a precise and stable method with high resolution on the evaluation has been established.

References

[1] R. B. Dooley and V. K. Chexal, Int. J. Pres. Ves. Pip., **77**, 85 (2000).

[2] J. H. Lee and S. J. Lee, NDT & E Int., **42**, 222 (2009).

[3] A. Vageswar, K. Balasubramaniam, C. V. Krishnamurthy, T. Jayakumar, and B. Raj, NDT & E Int., **42**, 275 (2009).

[4] G. Kajiwara, J. Test. Eval., **33**, 295 (2005).

[5] T. Shimakawa, H. Takahashi, H. Doi, K. Watashi, and Y. Asada, Nuclear Eng. Des., **139**, 283 (1993).

[6] K. R. Leonard and M. K. Hinders, Ultrasonics, **43**, 574 (2005).

[7] H. Nishino, M. Takemoto, and N. Chubachi, Appl. Phys. Lett., **85**, 1077 (2004).

[8] J. Ding, Y. Kang, and X. Wu, NDT & E Int., **39**, 53 (2006).

[9] J. B. Nestleroth and R. J. Davis, NDT & E Int., **40**, 77 (2007).

[10] M. Kamaya, T. Suzuki, and T. Meshii, Int. J. Pres. Ves. Pip., **85**, 628 (2008).

[11] C. Aristégui, M. J. S. Lowe, and P. Cawley, Ultrasonics, **39**, 367 (2001).

[12] L. Liu and Y. Ju, NDT & E Int., **44**, 106 (2011).

[13] L. Liu, Y. Ju, M. Chen, and D. Fang, Mater. Trans., **52**, 2091 (2011).

[14] D. M. Pozar, Microwave Engineering (2nd Ed), New York: John Wiley&Sons, (1998).

[15] Agilent Technologies. Time Domain Analysis Using Network Analyzer. Application Note 1287-12, March 2007.

Chapter 6. Conclusion and Prospect

This research is intendedly carried out for solving the present problems in pipeline systems caused by pipe wall thinning (PWT), because metal pipes are used widely in industry and accidents caused by PWT have been reported frequently all over the world in recent twenty years. Efficiently detecting and quantitatively evaluating the PWT locations and degrees (depths and lengths) in these pipes, especially for the long-distance pipes that have been used for many years, are mandatory for effective maintenance and lifetime prediction of the pipelines in order to avoid severe economical and social damages.

This research has established a remote, efficient, effective, and quantitative method of detecting the locations and degrees of PWT in a long-distance metal pipe based on the fact that a metal pipe can be taken as a circular waveguide of microwaves that can propagate a long distance with low attenuation in the pipe. Meanwhile, a wavelength, group velocity, and wave impedance change will occur at the PWT section.

When building up a resonance structure concerning the wavelength changes at the PWT section in the PUT, frequency domain measurement (FDM) of microwave signals is adopted to evaluate the PWT degrees (depths). When considering the time of flight (TOF) of microwave signals propagating in the PUT and that reflected from the PWT section, time domain measurement (TDM) of signals is adopted to evaluate the PWT locations and lengths (a length is obtained from the difference of the evaluated locations of the start and end points of a PWT section).

To carry out the FDM and TDM, a microwave vector network analyzer (VNA) was employed and a pair of coaxial-line sensors was designed to generate microwave signals propagating in the pipe. The two coaxial-line sensors were utilized separately for FDM

and TDM with the VNA working at S12 (or S21) mode and S11 mode, respectively. To approach a long-distance pipe with PWT defects, pipe specimens and PWT joints are used to combine many sets of PUTs with most of the lengths being longer than 2 m.

The evaluation of PWT depths is realized by firstly designing a two-port T&R coaxial-line sensor and working the VNA at S12 (or S21) mode while building up a resonance condition in the PUT, and then tactfully solving the resonance equations. By comparing the evaluated PWT depths obtained using this method with the nominal PWT depths deliberately introduced in the pipes, the maximum error of evaluation is found to be less than 0.05 mm, which is less than 0.294% of the inner diameter of the pipe. It indicates that a high precision evaluation method to remotely evaluate the PWT depth in a long-distance pipe is established.

The evaluation of PWT locations is realized by designing a single port T&R coaxial-line sensor and working the VNA at S11 mode while measuring the microwaves signals propagating and reflecting in the PUT. By analyzing time domain response of the signals and extracting the TOF corresponding to the PWT location, PWT locations are quantitatively evaluated after the group velocity of the signals in the pipe was calibrated. The arithmetical mean error of the evaluation for PWT locations is less than 1.7 mm, i.e. less than 0.068% of the length of the corresponding pipe. It indicates that an efficient and precise method to quantitatively evaluate PWT locations in a long-distance pipe has been established.

In addition, based on the fact that the TDM results are obtained from IFFT of the FDM results, through analyzing the frequency range and working mode of microwaves, and optimizing the sweeping frequency range, an improved TDM method for PWT location evaluation with space resolution no longer than the value of the pipe’s inner

diameter has been realized.

Because the microwave NDT&E method proposed in this research has significant advantages of nondestructive, remote, efficient, effective, and quantitative properties on detecting the locations and degrees of PWT defects in a long-distance metal pipe that can be measured under open-end condition, it has a great potential for the practical applications for the widely used metal pipes throughout the world.

The method to operate the VNA and to carry out the data processing shown in this thesis is also possible to be compiled into a commercial software that having a friendly human-compute interface, which can enable an unskilled operator/inspector to inspect or monitor the PWT conditions of a piping system that having a long-distance pipeline.

Acknowledgement

This thesis has been prepared at Department of Mechanical Science and Engineering at Nagoya University during the years 2008–2012. I have been fortunate throughout my life as a PhD student in this venerable graduate school, in which I have been able to concentrate mostly on my research, and also have a quick glance of the beautiful landscape, clean environment, and friendly, peaceful, and fast-paced life in Japan in my spare time.

First, I would like to thank my supervisor, Professor Yang Ju. I owe you so much. You've been my mentor, colleague, shepherd, and a never-ending fount of moral support. You have given so much of your time and energy to help me succeed in my research and my pursuit of a PhD degree at this famous university abroad. If I do take the academic path, you are my role model. You have enhanced me not only on research spirit, but also taught me the invaluable character of humility, modesty, prudence, diligence, and perseverance by personal example as well as verbal instruction. Whatever path I will take in my future life, I will be well prepared because of you.

I want to also give my heartily thanks to Prof. Guanbin Song (previous JSPS Research Fellow at Ju Laboratory) at Chongqing University of China, and the previous lecturer Dr. Hidehiko Kimura of Ju Lab. Thanks them very much for their help to handle many of procedures before and after my coming to Japan, and their giving many precious advice and suggestions on my research and daily life.

Then, I give my sincere thanks to Associate Professor Yasuyuki Morita. He not only has a graceful and elegant stance but also is quite kind and helpful in many things. There is one example strongly engraved in my mind that I cannot help mentioning. It was unlucky for me to have found the black ink of our printer had been used out just 30 minutes

before my pre-defense presentation, when I wanted to print the PPT document to distribute to all the committee professors. Prof. Morita not only helped me try two other printers and prepared the meeting room for me and even helped to take my PC to the meeting room personally by running and set all the things ready for my report. My heart has been touched by his kind and merciful behavior.

During my pre-defense presentation presided by Prof. Eiichi Tanaka of Biomechanics Laboratory, the members of the Examination Committee, Professor Noritugu Umehara of Umehara Laboratory and Researcher Kogen Sato of Toyota Central R&D Labs., Inc, have given me many precious and helpful advice, directions, and comments. In addition, they also spend lots of their precious time on reviewing my PhD dissertation although they are very busy every day. Sincere gratitude should be given to all of them for their precious advice, help, and time.

I also want to express my sincere gratitude to Assistant Professor Atsushi Hosoi for his warm help and great patience in my life during the four years of my PhD study and research. For many times of my conference presentation, he has been supporting me with his accompanying and encourage. He is not only a teacher and adviser in my research, but also a research partner and a helpful friend in my daily life. He is my best foreign friend since our first acquaintance, and we have spent together many wonderful times and he had even tried to invite me to visit and sleep at his home when we attended a conference in Yokohama. I am sure many of the good memories of our international and unsophisticated friendship will accompany me for ever.

Technical assistant Dr. Teruaki Mikuriya is always optimistic, energetic and helpful in his work and life. Because my research needs lots of pipe and joint specimens, he has been a great help to machining almost all of the specimens and also do the work efficiently,

and a lot of gratitude should be given to him.

I give my deeply grateful thanks to two of my best partners and friends, Dr. Mingji Chen, and Mr. Lan Zhang (who will also achieve the PhD degree in soon future). When I met with difficulties on my research or in my life, they have been always living together with me with their accompanying. We have built a precious friendship. Many thanks also should be given to Dr. Xu, and the following PhD students Mr. Song, Mr. Tang, Mr. Wang, Mr. Hu, Ms. Yue, and master students Ms. Wang, Ms. He, and Ms. Zhang.

Ms. Misaho Kawahara is careful and responsible, and also helpful on handling some procedures of business trip. Previous master students such as Mr. Suzuki, Mr. Kubota, Mr. Ishikawa, Mr. Nagahama, Mr. Sasaki, Mr. Fujioka, Mr. Kondo, Mr. Yoshimoto and Mr. Fujimoto, etc., who had graduated from Ju Laboratory have helped me a lot during my research work and daily life. The present master students such as Mr. Koto, Mr. Yano, Mr. Nakayama, Mr. Yamauchi, Ms. Watanabe, Mr. Amano and Ms. Iwasaki have also give me lots of help, and I thanks them for their kind helps in Ju Laboratory.

During the last year, I was a little too busy and also had some private things, and as a result, I am not very familiar with all the M1 and B4 students. Mr. Yoshida, Mr. Ishiguro, Mr. Teshima and some other students that I even can’t call their names accurately also have made lots of help in my life. Here, I also give some thanks to them. In addition, I am thankful to all the other members in Ju Laboratory with whom I have interacted in one way or another.

I am also greatly indebted to Nagoya University for the research grant of funding my PhD research and to JSPS “Global COE for Education and Research of Micro-Nano Mechatronics” for the financial support for my research and life, and also to the Chinese government for granting me the *Chinese Government Award for Outstanding Self-financed*

Students Abroad of 2010.

Finally, I give my deepest emotional thanks to my parents, who have always been my unconditional support during my study from a six-year-old boy to a thirty-year-old man. They opened my eyes when I am a naive child, and broadened my mind throughout the 25 years of my study, research, and life with plenty of love and patience. Many brothers and sisters in the church of Nagoya who believe in that all human beings are children of God have also given me a great deal of help when I was in the depressed time of some difficult matters. Here, I also give my heartily gratitude to all of them.

I feel so happy and lucky to have had the precious and honorable experience to do the PhD research here and cooperate with many of the brilliant students in Ju Laboratory, and I am glad to have learned and achieved much from the lives together with them and published five scientific journal papers and more than a dozen of conference papers.

I have experienced many things in Japan, although I was already 26 years old when I came here at the first time, during these recent four years, I have grown up and improved a lot (out of my imagination) at our laboratory and at our university. Thus, there is no doubt that the study, research, and life experience in Japan will be an invaluable fortune for the future of all my life.

Linsheng Liu

Nagoya University

November 2011, Japan